

Prediction of the airborne sound transmission through a car front end model including poroelastic acoustic treatments

Dissertation

zur Erlangung des akademischen Grades

**Doktoringenieurin
(Dr.-Ing.)**

von Dipl.-Ing. Maria Gavila Lloret

geb. am 30.12.1991 in Benetusser (Valencia, Spanien)

genehmigt durch die Fakultät für Maschinenbau
der Otto-von-Guericke-Universität Magdeburg

Gutachter: Prof. Dr.-Ing. Hermann Rottengruber

Prof. Dr.-Ing. habil. Dr. h. c. Ulrich Gabbert

Promotionskolloquium am 12.12.2018

Acknowledgements

The work presented in this thesis was developed during my three-year occupation as PhD candidate in the group of Airborne Sound Acoustics at the BMW Group and in collaboration with the faculty of Mechanical Engineering at the Otto-von-Guericke Universität Magdeburg.

In the first place I would like to thank Prof. Dr.-Ing. habil. Dr. h. c. Ulrich Gabbert for the continuous support during my PhD study, for his patience, motivation and immense knowledge. I am very grateful that he accepted the supervision of this thesis and I appreciated the stimulating discussions we had along the last years.

I extend my gratitude to Prof. Dr.-Ing. Hermann Rottengruber, who also supervised and reviewed this work. His suggestions and comments from a more industrial perspective were always useful and enhanced the quality of the thesis.

For the smooth collaboration I am very grateful to the colleagues at the Otto-von-Guericke Universität Magdeburg, I always felt very welcome in Magdeburg. Every meeting at the university and in the different conferences led to fruitful discussions and new ideas. A very special thank you to Fabian for the continuous help, his enthusiasm and his constructive recommendations. Thanks too to Peter and Lars, who also contributed to bring this work forward.

I would like to express my gratitude to my supervisor at BMW, Dr. Gregor Müller, for the valuable comments, remarks and his engagement through the learning process of this PhD thesis. Furthermore, I would like to thank Dr. Peter Kalinke for making sure that I always had the appropriate conditions for the development of this research. The work of Mr. Thomas Hagl during his Master's thesis was a helpful contribution to the final result. My sincere thanks also goes to all former and current colleagues at BMW for the friendly work atmosphere in FIZ and in Aschheim.

I thank Rebecca for always having an open ear for me. A huge GRACIAS to my family, especially my mother and father, who first gave me the opportunity to study abroad and then had to deal with the distance between Valencia and Munich. Many thanks to Marco who was an incredible support during the last hard months of this thesis. This accomplishment would not have been possible without them. Thank you all!

Munich, December 2018

Maria Gavila Lloret

Contents

Kurzzusammenfassung	VII
Abstract	VIII
1 Introduction	1
1.1 Motivation	1
1.2 Objective	3
1.3 Outline of the thesis	4
2 Hybrid approach for the prediction of airborne sound transmission	6
2.1 Noise sources and transmission paths in a vehicle	6
2.2 Airborne sound transmission through the car front end	8
2.3 Hybrid approach	9
3 Numerical methods for vibroacoustic problems	12
3.1 Vibroacoustic simulation	12
3.2 Finite Element Method for vibroacoustic applications	14
4 Modeling of poroelastic components	27
4.1 Description of poroelastic media	28
4.2 Numerical methods for poroelastic media	42
5 Evaluation of vibroacoustic models for poroelastic media	53
5.1 Working principle of spring-mass systems	53
5.2 Description of the numerical configuration	55
5.3 Measured data for verification	58
5.4 Comparison of numerical and experimental results	63
5.5 Concluding remarks	74
6 Combination of experimental and numerical results in a hybrid approach	77
6.1 Panel contribution analysis	77
6.2 Mathematical description of the hybrid method	80
6.3 Numerical verification	82
6.4 Reciprocal measurement of the transfer functions	84
7 Simplified model of the vehicle front end	87
7.1 Description of the simplified model	87
7.2 Comparison of numerical and experimental results	91
7.3 Integration of the numerical front end model with measured transfer functions	97
7.4 Summary	103
8 Concluding remarks and outlook	105

References

109

Kurzzusammenfassung

Akustik und Schwingungen Vorgaben spielen eine wichtige Rolle in der Entwicklung von Personenkraftwagen. Die Auslegung und die Bewertung von passiven akustischen Maßnahmen erfordert, dass zuverlässige Vorhersage-Tools zur Verfügung stehen. Diese Modelle müssen die Anwendungsbedingungen realitätsnah berücksichtigen und sollen eine detaillierte Darstellung der Anwendungsumgebung beinhalten. Der aktuelle Auslegungsprozess basiert meist auf experimentellen Analysen, die während der ersten virtuellen Entwicklungsphasen dennoch nicht anwendbar sind. Zur Überwindung dieser Begrenzung stellt diese Dissertation ein hybrides Verfahren vor, das numerisch und experimentell ermittelte Daten integriert, um die Schallübertragung durch komplexe Systeme zu beschreiben.

Im ersten Schritt wird die Übertragungskette in ihre wesentlichen drei Komponenten bestehend aus der Anregung, dem strukturellen System und dem Empfangsgebiet geteilt. Anschließend wird jedes System getrennt untersucht. Der größte Vorteil dabei ist, dass der geeignete Ansatz abhängig von der vorhandenen Information entweder numerisch oder experimentell ausgewählt werden kann. Zum einen steigert die Beschreibung des strukturellen Bauteils mittels einer Simulation die Flexibilität, unterschiedliche Konfigurationen mit reduziertem Aufwand zu analysieren. Zum anderen umfasst die Verwendung von experimentellen Daten automatisch eine realistische Repräsentation der Anregungs- und Empfangsdomänen. Schließlich werden die Ergebnisse der partiellen Modelle zusammengefügt.

Ein zentraler Aspekt die erforderliche Robustheit der Simulationsergebnisse zu sichern ist die genaue Beschreibung von den akustischen Maßnahmen. Diese bestehen in weitem Umfang aus poroelastischen Medien. Die Mechanismen der Energiedissipation dieser Materialien sind aufgrund der zweiphasigen Natur schwierig zu modellieren. In dieser Dissertation werden drei unterschiedlichen Materialformulierungen zur Definition des poroelastischen Verhaltens mit Hilfe der Finite Elemente Methode verglichen. Ihre Funktionsfähigkeit wird für verschiedene Konzepte in zwei Konfigurationen überprüft, wobei Messungen in einem Fensterprüfstand die Referenzdaten liefern. Daraus zeichnet sich die Materialcharakterisierung als ein entscheidender Faktor für die Auswahl und die Anwendung einer Materialformulierung aus.

Nach der Verifikation der numerischen Modelle wird das hybride Verfahren am Beispiel eines vereinfachten Vorderwagens umgesetzt. Die gemessene einfallende Druckverteilung sowie die reziprok ermittelten Empfangstransferfunktionen werden mit der numerischen Information kombiniert. Dadurch kann die gesamte Übertragungskette beschrieben werden. Abschließend wird das Potenzial des vorgestellten Ansatzes einschließlich der Optionen zur Effizienzsteigerung diskutiert.

Abstract

Noise, vibration and harshness specifications play an important part in the development of passenger vehicles. The design and evaluation of the passive noise control treatments requires that reliable prediction tools are at one's disposal. These models have to realistically take into account the application environment and should include a detailed representation of the sound packages. The current acoustic design process is mostly based on experimental analyses, which are however not suitable during the early virtual stages of development. To overcome this limitation the present thesis proposes a hybrid technique that integrates numerically and experimentally determined data to describe the sound propagation through complex systems.

The first step consists in the division of the transmission chain into its essential components, namely, the excitation, the structural system and the reception domain. Next, each system is separately investigated. The main advantage of this method is that the most appropriate approach, either numerical or experimental, can be chosen depending on the available information. On the one hand, the description of the structural component with a simulation increases the flexibility to study different configurations with reduced effort. On the other hand, the use of experimental data automatically comprises a lifelike representation of the excitation and reception domains. As a last step, the results of the partial models are merged.

One key aspect to ensure the robustness of the simulation results of the structural subsystem is the accurate representation of the noise control treatments. To a large extent, the noise packages are composed of poroelastic media. The energy dissipation mechanisms inside such materials are difficult to model due to their biphasic nature. Throughout this thesis three material formulations to define the poroelastic behavior are investigated with the help of the Finite Element Method. Their performance is inspected for different noise control treatment concepts in two configurations for which measurements in a window test bench provide the reference data. Thereby the material characterization stands out as a decisive factor in the choice and the application of a material formulation.

After the verification of the numerical models, the hybrid approach is put into practice in the example of a simplified vehicle front end. The measured incident pressure distribution as well as the reciprocally determined reception transfer functions are combined with the numerical information to describe the complete transmission chain. Finally, the potential of the presented methodology, including options for the efficiency enhancement, are discussed.

Chapter 1

Introduction

1.1 Motivation

The acoustic performance plays a decisive role in the development of passenger vehicles. Together with the visual and haptic impressions, comfort defines the quality perception of the product, which is a major distinguishing characteristic among cars. The acoustic features also have a safety function as they give the driver essential feedback on the proper working order of the vehicle [1]. Furthermore, sound is an element of the brand identity. However, annoying and undesirable noises have to be suppressed or minimized. The noise, vibration, and harshness (NVH) concepts must therefore deliver a consistent and balanced product. The main challenge during the development process arises from the conflict of interest between the acoustic requirements and other project limitations such as weight, construction space and costs.

The growing customer expectations, especially in the premium car segment, and the stricter regulations on noise emissions intensify the demands on the comfort features. Additionally, the ongoing trends towards a more efficient and environmentally friendlier transportation have a large impact on the acoustic properties. For example, the application of lightweight design concepts reduces the basic insulation of the car body. Engine downsizing decreases the fuel consumption by using smaller engines, but it also generates a louder excitation level. Moreover, the expansion of electric and hybrid drive technologies radically modifies the traditional sound characteristics of internal combustion engines as well as they unmask some noise sources that were before imperceptible for the car occupants [2, 3]. Besides, the numerous sensors and control devices necessary for the new driving assistance systems occupy extensive construction space and require supplementary holes for the power and data lines [4], thus limiting the available volume for acoustic treatments.

The NVH engineers can improve the vibroacoustic behavior of the vehicle with the help of different modifications on the noise sources and along the acoustic transmission paths. An option to control the noise emissions is the minimization of the excitation levels. For instance, an offset of the piston pin can decrease the noise induced by the piston slap [5]. The tuning of the engine mountings [6] and the application of acoustic barriers [7] are examples of measures that contribute to the reduction of the total transmitted acoustic energy. Through active sound design is possible to purposely intensify or lessen noises as engine related sounds to achieve the targeted acoustic attributes [8]. In general, the noise control strategies can be classified into active and passive measures. With an active noise control system the undesired noise or vibrations are attenuated by destructive interference of the original signal with another signal generated by a secondary source [9]. Such an approach is adequate to suppress harmonic or constant perturbations like engine orders. However, supplementary components such as sensors and actuators are necessary for the

operation of active systems. Furthermore, their working range is limited by the distance between the secondary source and the reference microphone. Consequently, inside a passenger car, they are usually only applicable at low frequencies [10]. Alternatively, passive treatments can be employed. They diminish the transmission of the acoustic energy by means of absorption, insulation and/or damping along the propagation paths. Damping materials find application for low frequencies, whereas absorber and insulating treatments are especially effective for the noise reduction in the middle and high frequency ranges. Since they do not require any additional systems or energy sources, the passive sound packages are easier to integrate in the vehicle and their use is very widespread. In the following, we focus on the application of insulators and absorbers as passive treatments. In order to evaluate the functionality of the designed acoustic measures, experimental tests are the common practice. Nevertheless, the early stages of the product design are mostly virtual. Due to shortened development cycles and the reduction of the available prototype hardware, reliable prediction models become increasingly important [11]. Such design tools have to realistically reproduce the acoustic transmission chain, need to enable a comparison among different design concepts and, lastly, be able to relate the obtained results to the customer perception. The constant improvements in the computational capabilities during the last decades have allowed an extension of the integration of computer-aided methods in the early design and development stages. In the vibroacoustic applications the accuracy of the models strongly depends on the proper representation of the noise control treatments, whose main function is the reduction and insulation of the transmitted sound energy.

In literature we find numerous application examples of the description of the sound propagation including passive acoustic treatments in an automotive context. The work by Dejaeger *et al.* [12, 13] investigated the noise propagation through a vehicle dashboard including the instrument panel. The acoustic trims were explicitly modeled as structural and poroelastic components. To facilitate the comparison of the calculated results to the reference measurements in a window test bench, the system was clamped in a concrete frame, which strongly influences the global stiffness behavior of the structure. Other components that are also commonly object of the numerical analyses at component level are the floor module and the headliner. The approach employed by Korte [14] took into account the damping treatments and insulators on the vehicle floor. The statistical method used in that example is suitable for the middle and high frequency ranges. However, it does not allow for the analysis of local responses. A detailed examination of the dynamic behavior can only be obtained if a discretization approach is applied. In [15] the vibroacoustic performance of the Finite Element model of a headliner module was investigated up to a frequency of 1 kHz. Similarly, a trimmed floor module was studied in [16] up to 600 Hz. The article focused primarily on the performance of several models for the acoustic package, but no experimental reference data was provided.

The aforementioned examples were limited to analyses at component level, that is, the systems were evaluated as cut out modules separately from their real boundary and coupling conditions. Such approaches lead to smaller models that are faster to calculate, but present the disadvantage of not being able to refer the obtained results to the vehicle global performance or to the occupants perception. The influence of the real environment in the evaluation of the vibroacoustic behavior was remarked in [17]. In their work, Stelzer *et al.* compared the acoustic response of a floor module firstly placed between two semi-infinite fluids and secondly when it radiated into a closed passenger compartment. The interaction with the fluid cavity was proved to have significant impact on the

response. There are other study cases that additionally represented the structural parts of the car body that limited with the passenger cabin, including an explicit description of the sound packages too [18–20]. The major drawback arises from the fact that the computational effort increases severely with the size of the system, restricting the application to frequencies up to approximately 400 Hz.

Another option in order to obtain a realistic description of the properties of the inner cavity is to make use of measured data. In-situ measurements of the impedance at the surfaces of the cavity walls like in [21, 22] can be employed to update the information at the boundary conditions of the fluid. This procedure, nonetheless, requires the availability of hardware, which is not always at disposal during the early development stages, and an explicit modeling of the cavity fluid.

An alternative approach to overcome the latter issue was proposed by Tinti *et al.* [23]. In their work, the transfer functions between the radiating surfaces of the car body and the targeted point, e.g. the driver’s ear, were experimentally determined. That way the propagation behavior inside the cabin was implicitly captured and the representation of fluid volume could be omitted. The structural response was numerically determined for the excitation generated by three point forces. The acoustic treatments were also included in the simulation model as flat components of constant thickness. By the combination of the measured transfer functions with the calculated velocities on the structural panels, the pressure level at the observation point could be reconstructed. Because of the limitations on the computational power in the 1990s, though, the model could only be evaluated up to 220 Hz.

In summary, there are in the literature many application cases that examine the behavior of the acoustic packages at component level. Their main drawback is that they neglect the influence of the real environment on the vibroacoustic response. In most instances, the modeling of the acoustic treatments plays a secondary role and just few information on the description of the sound package is given. Furthermore, a great part of the examples lack of reference data sets for the validation of the numerical models.

1.2 Objective

During the vehicle development process the NVH engineers have to be able to evaluate the performance of different vibroacoustic concepts. In order to meet the product specifications and to deliver a high quality product, all project requirements should be considered from the beginning, so that optimized solutions can be found. Especially at the early stages in which hardware availability is restricted, the current, mostly experimental design processes need to be complemented with virtual prediction tools. The robustness of these models depends on two main factors. On the one hand, a realistic description of the system and its environment is decisive. This means that the excitation sources as well as the transmission paths need to be precisely represented. On the other hand, the modeling of the acoustic treatments is a key point for the accuracy, since they modify the way the sound energy propagates.

In this research, an approach to predict the airborne sound transmission is developed. Because of the high complexity of the considered propagation phenomena, we propose the use of a hybrid methodology that combines experiments and computer-aided simulations. This synergy allows to exploit the benefits of both procedures. In other words, the lifelikeness of experimental data complements the flexibility of the simulations to analyze

many different design configurations, so that the applicability of the overall method is enhanced.

The objective of this work is to develop a reliable procedure to evaluate the vibroacoustic behavior of complex systems including the passive noise control treatments. The main focus rests on the representation of the acoustic treatments based on poroelastic media, whose industrial utilization is widespread. The complete prediction model is exemplarily applied to a simplified model of a vehicle front end.

One of the principal difficulties of the approach lies in the numerical representation of poroelastic materials. Several virtual models are available for the description of their vibroacoustic behavior. Nevertheless, the application ranges of each one are not precisely known yet. Besides, the suitability of the characterization procedures, which provide the input information for the modeling, needs also to be reviewed. Another major challenge results from the hybridization process itself. The practical integration of the numerical and experimental results is not a straightforward process and requires that the models in the simulations and measurements be carefully prepared. These two aspects are analyzed with special attention in the following chapters.

1.3 Outline of the thesis

The present thesis is structured as follows. Chapter 1 introduces the importance of the acoustic properties in the development of passenger vehicles and presents some of the conventional noise control treatments. After a review of the state of the art of strategies for the prediction of the sound propagation, the objective of this work is derived. A hybrid tool to evaluate the vibroacoustic performance of complex systems including poroelastic sound packages is pursued. In Chapter 2 the basic concepts of the noise sources and the transmission paths in a vehicle are given. A special interest is taken in the specifics of the airborne sound transmission through the car front end, which is the example of application. These characteristics indicate the implementation framework for the striven hybrid approach, a combination of numerical and experimental methods. Chapters 3 and 4 draw attention to the numerical side of the procedure. In Chapter 3 the emphasis is on the resolution of fluid and structure coupled problems. Among the available techniques the Finite Element Method is chosen as most suitable. The following Chapter 4 examines two key points of the modeling of poroelastic media. First, the poroelasticity theory is outlined and the meaning and characterization procedures for the numerous material coefficients are discussed. Second, the numerical calculation centers again on the Finite Element implementation. The performance of three different material formulations is inspected with the help of several insulating spring-mass systems attached to a flat steel plate in Chapter 5. There, the comparison to measured data obtained in a window test bench assists to determine the application ranges as well as the limitations of each model. Chapter 6 provides further insight into the practical details of the hybrid approach. This includes the main mathematical principles, a numerical verification of the method, and the procedure for the experimental determination of the reciprocal transfer functions. The first part of Chapter 7 extends the conclusions of Chapter 5 to a simplified model of the vehicle front section. Additionally, sound absorbing noise control treatments are investigated in this setup. The second half of the chapter analyzes the integration of the numerical and experimental results according to the proposed hybrid approach. Measurements of the complete system in a window test bench also serve as reference here.

Lastly, Chapter 8 summarizes the major findings of the research and maps out the next steps and the potential future developments.

Chapter 2

Hybrid approach for the prediction of airborne sound transmission

Robust statements on the performance of noise control treatments are a central element in the noise, vibration and harshness (NVH) development process. In the current chapter a tool to predict the airborne sound transmission is presented. It is based on the merging of measurements and numerical results in a so-called hybrid model. This combination allows to include a detailed representation of the acoustic treatments in a realistic application environment, as the following sections and chapters emphasize. First, the basic concepts of the vehicle acoustics are introduced in Section 2.1, with special regard to the classification of the noise sources and transmission paths. Section 2.2 gives information about the specifics of the airborne sound transmission through the front end of the vehicle. Finally, the main characteristics of the proposed hybrid approach are explained in Section 2.3.

2.1 Noise sources and transmission paths in a vehicle

Noise and vibration are significant contributions to the passenger comfort, which also includes other aspects like temperature, ergonomics, and vehicle dynamics. Traditionally, vibrations have been associated to reliability and durability attributes. Furthermore, in the last decades, noise and vibration have become progressively a basic feature of the quality properties of passenger vehicles. The increase of the comfort standards as well as stricter noise regulations intensify the key part of the NVH specifications during the development cycle of a car.

The mechanical wave propagation that takes place in fluid and solid media is responsible for the phenomena related to noise and vibration. The wave transmission is usually classified according to the origin of the excitation, the transmission path, and the frequency range of perception. Vibrations, for instance, are sensed through the touch sense at frequencies between 1 Hz and 250 Hz, whereas vehicle noises can be heard by the passengers and pedestrians in a range from 30 Hz up to over 10 kHz [9]. Moreover, noise can be divided into airborne and structure-borne depending on whether the wave propagation mainly occurs in a fluid or in a solid medium. In a typical car, the structure-borne transmission paths are dominant for frequencies under 200 Hz, whereas the airborne transmission paths predominate above 500 Hz. In the middle frequencies both kinds of paths show a comparable contribution to the total perceived sound level [7]. There are some phenomena that fall outside of this classification, as is the case of the low-frequent booming noise caused by the intake system [1].

Figure 2.1 schematically illustrates how the noise is transmitted from the different sources to a receiver. We can differentiate between airborne and mechanical excitations. The di-

rect airborne noise is originated by the interactions with the moving air. Examples of such sources are the pressure fluctuations and the induced turbulence due to the airflow motion around a body [24, 25]. These phenomena are the object of study of the aeroacoustics.

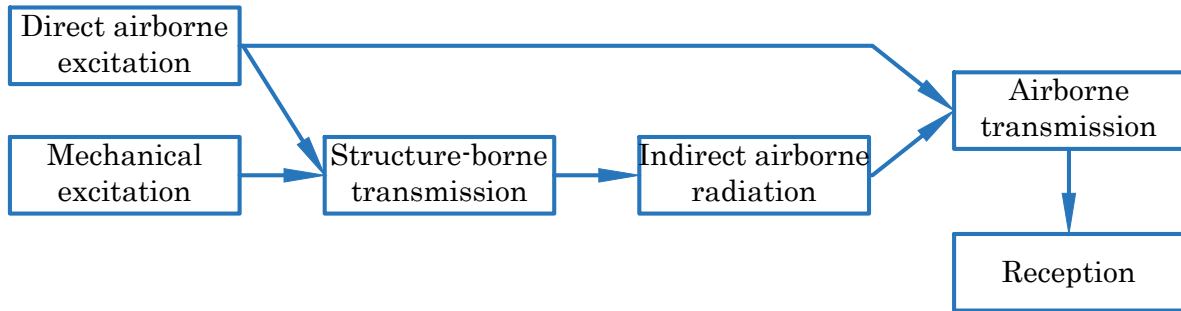


Figure 2.1: Schematic description of the noise transmission (adapted from [26]).

During the operation of the vehicle many other noise sources can be identified. One of the principal sources are the engine itself together with all the associated aggregates like the gearbox, the drive shaft, or the intake and exhaust systems. The working of the powertrain unit causes vibrations on the components that are transmitted through the solid bodies up to their outer surfaces. These vibrations can be radiated into the surrounding air in form of pressure oscillations, giving rise to the indirect airborne radiation. Another relevant noise source comes from the tires. As a result of irregularities on the road and uneven tire profiles, the contact between the wheels and the pavement can induce vibrations. These are also transmitted to the surrounding air. Auxiliary units such as the air conditioning system or the windscreen wiper are additional acoustic sources.

The direct transmission of the aeroacoustic and radiated sound energy in the air through massive walls or leakages up to the receiving points are classed in the so-called primary airborne noise. Besides that, the radiated pressure waves in the air can induce vibrations in other structural components like the firewall and the underbody, which later transmit the acoustic energy again into the air. The contribution of the noise propagated this way is known as indirect or secondary airborne noise [27]. Lastly, the vibroacoustic energy may be transmitted from one mechanical component to another. A typical situation is the propagation of the vibration energy of the engine to the chassis through the supporting bearings. This is an example of structure-borne noise. If the oscillations caused by the structure-borne transferred energy are radiated by the structural surfaces and become audible, they add up to the secondary airborne noise.

In Figure 2.2 the major acoustic sources in an operating vehicle are represented in a simplified form. Some noises, like the one produced by the turn indicators, have a functional purpose and should be perceived. Conversely, other are undesirable or annoying and, hence, should be minimized [26]. There are numerous options to reduce the total noise level in a vehicle. Those measures can be directly applied on the sources, on the transmission paths, or on the reception side. Because of the diversity of the noise generation and transmission mechanisms, of the excitation levels and frequency spectra it is not always possible to define standard acoustic treatments, but different solutions can work for the same problem. Some examples of common noise control measures have been indicated in the previous Section 1.1. The key challenge during the design stages lies in finding the acoustic treatment that fulfills the NVH requirements within the framework set by the other project limitations like weight, cost and construction space. To this end, the

combined support of expert knowledge, experimental techniques and numerical tools is necessary.

2.2 Airborne sound transmission through the car front end

The main acoustic sources vary depending on the operational state of the vehicle. At low and middle velocities with low engine loads the tire noise is the most significant source, while the engine radiation gains importance as the acceleration is increased or when running at idle. At higher velocities the wind excitation through the windshield and the A-pillars is dominant. In the present section the focus is set on particularities of the airborne sound transmission through the front end of a vehicle, the section in which the investigations in the last chapters are implemented.

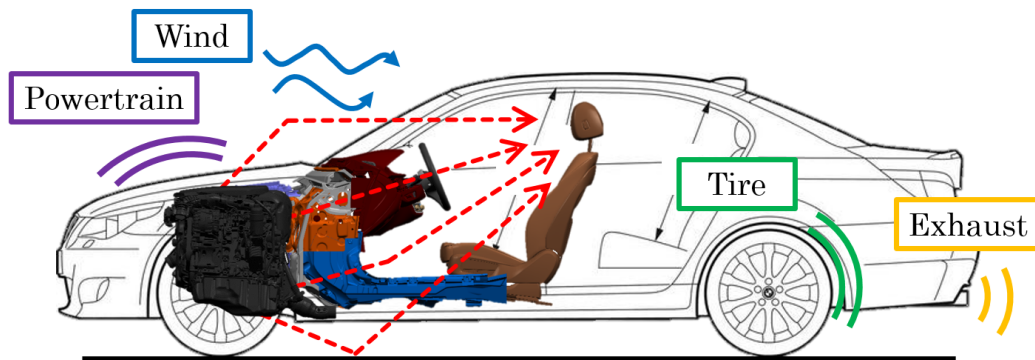


Figure 2.2: Main airborne noise sources in a vehicle during operation. The red dashed arrows symbolize the major transfer paths between the radiating engine and the receiver.

The noise propagation through the front area is of high complexity because of the numerous components and the several parallel paths. Next, the airborne transmission into the cabin using the engine excitation as acoustic source is exemplarily analyzed. The operation of the powertrain and its aggregates generates vibrations on their surfaces that are radiated into the surrounding air in form of pressure fluctuations. These acoustic waves can then propagate inside the engine compartment. A part of them is transmitted through the engine cover and the hood into the outer air, which in turn excites the windshield. Another portion of the energy is radiated downwards, reflects on the floor and induces vibrations in the car underbody structure. The excitation of the wheelhouse transmits an amount of the acoustic power into the side walls and door compartments. Besides, a great part of the energy impinges on the front structural panels of the firewall and the carrying beams. The waves on the upper half travel first through the instrument panel cavity before radiating through the dashboard. These major transmission paths are illustrated in Figure 2.2 with red dashed lines. The vibrations induced on the interior panels can radiate into the interior compartment fluid and contribute all together to the total noise level inside the cabin. Additionally, the primary airborne noise is transmitted through the leakages and the small openings that are required for the cable channels and other systems like the pedals.

The reduction of the airborne noise pays particular attention to the acoustic transmission paths and to the absorption properties of the passenger compartment [7]. On the one hand,

the design of the acoustic paths should, to the extent possible, avoid any leakages and apertures that directly link the source to the receiver. On the other hand, a solid concept of sound packages combining insulation, damping and absorption should be developed.

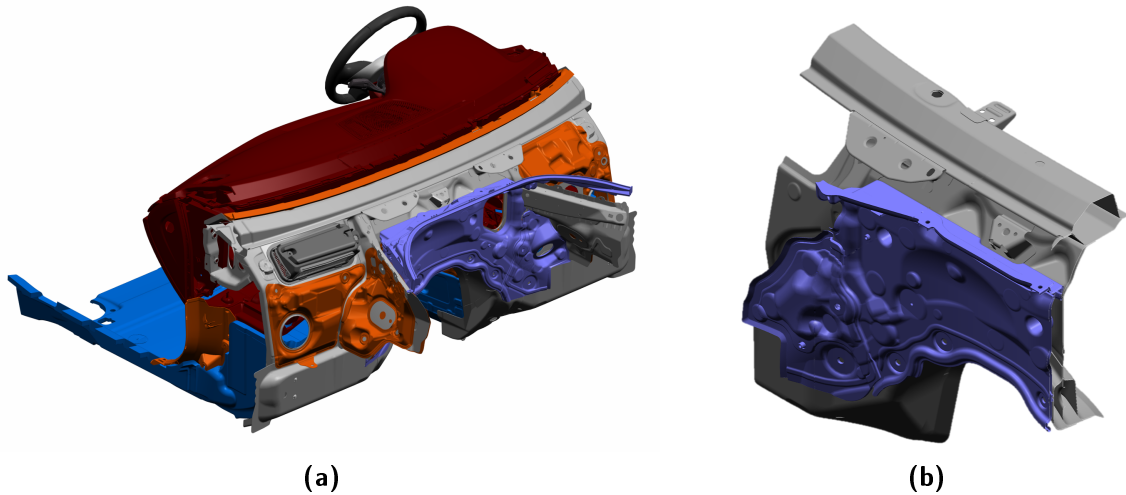


Figure 2.3: Vehicle front end with acoustic treatments: (a) noise control treatments (orange) applied on the firewall (grey), (b) detail view of the second firewall (violet).

The sound transmission through the firewall can be modified with the application of several kinds of acoustic treatments. Sometimes an additional panel, also known as second firewall, is placed in front of the firewall as represented in Figure 2.3b. The insulation is thereby augmented according to the double wall principle [26]. Other effective measure to reduce the noise transmission can be achieved by increasing the absorption in the air cavities with the utilization of absorber layers, for instance, in the engine compartment (Figure 2.3a), behind the dashboard or inside of the passenger cabin. Lastly, a widespread option is the combination of the latter two, that is, a double wall filled with absorber material. Such aggregate is known as a spring-mass system and its working principle is explained in detail in Section 5.1.

A standard method to analyze the acoustic performance of a vehicle in operational conditions are the measurements on a dynamic roller test bench. In this procedure the vehicle is placed on large rollers that allow the wheels to roll at the desired velocity [28]. Furthermore, the test bench includes a suction system to enable the motor to run during the measurement too. The major advantage over tests on the road is that the experiment conditions are controlled and highly reproducible. The aeroacoustic effects are thus excluded. Investigations with different passenger vehicles have shown that either at full or partial throttle, the airborne sound transmission through the instrument panel area is dominant for frequencies between 100 Hz and 2 kHz. The targeted model for the sound transmission in the front section should therefore be able to reproduce the vibroacoustic behavior of the metal panels, the fluid cavities, the absorbing layers and the double wall systems in that frequency range.

2.3 Hybrid approach

At the early stages of the vehicle development cycle reliable statements on the effectiveness of the noise control treatments are required. On the one hand, robust acoustic

concepts should ensure that no issues arise in the later development phases. On the other hand, specifications on the required construction space, the corresponding weight and the estimated costs need to be timely reported to the project management.

To a large extent, the verification of the airborne acoustic properties is experimentally based, which means that prototypes are needed to obtain information about the performing state. However, at the very beginning of the design process only virtual models are available. As a result, the development of the acoustic concepts currently relies on expert assessment and on measurements conducted on the predecessor model. An alternative practice could be the utilization of computer-aided engineering techniques. They are nowadays widely spread to assess the vibroacoustic behavior at component level [29] or in the low frequency range [30]. Nevertheless, if the real conditions of the application environment like the excitation characteristics and the properties of the receiving domain are to be considered, the size of the models becomes too large. For this reason their use is no practicable for frequencies above a couple of hundred Hertz.

To overcome these difficulties, this thesis proposes the combination of experimental and numerical techniques in a hybrid model. The basic hypothesis is that the merging of measured information with numerical data allows to obtain accurate predictions. That way, the advantages of both worlds are exploited. Experimental results intrinsically take into account the complexity of the real excitation and reception environments, whereas the numerical methods allow for a comprehensive representation of structural systems already during the virtual project phases.

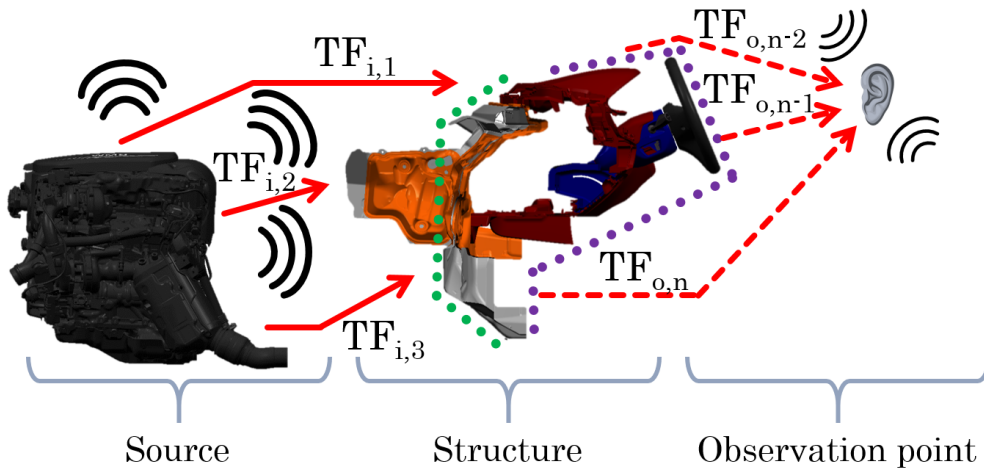


Figure 2.4: Schematic representation of the proposed hybrid approach applied to the vehicle front end.

In the presented hybrid approach the sound propagation chain is split into three subsystems according to the source-path-receiver transmission model. As Figure 2.4 shows in the example of the front section, we can identify one or more acoustic sources, a structural component throughout which the transmission mainly occurs, and an observation point at which the response is analyzed. The propagation of the vibroacoustic energy from one subsystem to the next one is included in the linking input and output transfer functions (TF_i , TF_o). The hybrid method has been developed on the basis of the panel contribution analysis (PCA), which is a standard experimental diagnosis tool in the airborne acoustics. More details on the foundations of the PCA and the underlying mathematical principles are given further on in Sections 6.1 and 6.2, respectively.

The major benefit of this hybridization technique is that all three components can be described independently of the others. That implies that the most appropriate approach for each subsystem, either experimental or numerical, can be chosen depending on the current development stage and the available resources. For instance, the radiation characteristics of the source may be simulated at the early project phases [31]. Later, the information may be replaced by measured data in an engine test bench as soon as the hardware is at disposal. Furthermore, the use of measurements in the predecessor model for the sound propagation inside the cabin permits to include the absorption and reflection properties of the receiving domain without any additional modeling effort. Another significant advantage is that the numerical representation of the structural component enables a great detail level in the modeling of different noise control treatments. This makes it possible to compare different acoustic concepts in the real application environment and, eventually, to run optimization loops. The numerical representation of the structural subsystem including the noise control treatments is the main topic of the research.

The principal steps of the hybrid methodology are examined throughout this thesis. As mentioned in the previous section, the frequency range of interest in all following investigations covers up to 2 kHz. In order to include all the frequency information in the standard 2 kHz third band, the frequency values up to 2240Hz are included.

Chapter 3

Numerical methods for vibroacoustic problems

The present chapter is dedicated to the numerical prediction of the dynamic behavior of vibroacoustic systems. In the first section, a short literature survey on the state of the art of the modeling techniques is conducted. Among the available numerical methods the Finite Element Method stands as most suitable for the aimed application. In Section 3.2 the dynamic vibroacoustic equations for fluid and structural components are recalled. After that, the Finite Element derivation is given, with special focus on the fluid-structure interaction and the corresponding coupling conditions. The chapter concludes with the convergence analysis of a coupled application.

3.1 Vibroacoustic simulation

Vibroacoustics deals with the interaction of vibrating structural systems coupled to acoustic fluids [32]. Depending on whether the fluid domain has a limited size or is unbounded we speak of an internal or an external vibroacoustic problem, respectively. If both bounded and unbounded fluid domains are present, we call it a mixed problem. The vibroacoustic behavior of a system can be mathematically described in terms of partial differential equations. The analytical solution of these governing equations is only possible for very simple domains, like the one-dimensional wave propagation [33]. For most practical cases, however, it is necessary to make use of a numerical method in order to obtain an approximated solution of the equations.

The numerical approaches can be divided into deterministic and probabilistic techniques. The deterministic methods are based on the discretization, that is, the division of the continuous fluid and structural domains into small elements. The Finite Element Method (FEM) is the most popular among the deterministic numerical approaches. It was first derived for solving static deformation and stress problems, but its use has been meanwhile extended to nearly any engineering application [34]. First, the integral form of the governing dynamic equations is derived. Under the assumption of linear dynamic behavior, the discretization of the domains into a finite number of elements results in a system of linear equations. The unknowns of the vibroacoustic system are the dynamic quantities acoustic pressure and solid displacements at certain points of the elements known as nodes. After assembling the domains using the appropriate coupling conditions, the system of equations can be condensed into symmetrical, frequency-independent matrices with real coefficients. The main disadvantage of the FEM is that, as the frequency increases and the wavelength becomes smaller, the size of the elements has to be reduced to properly capture the dynamic changes. This leads to very large models and

thereby limits the application of the FE approach at high frequencies. Another original difficulty of the Finite Element Method was the treatment of unbounded domains, but nowadays the combination with special procedures as the Perfectly Match Layer [35] or Infinite Elements [36] helps to overcome this issue. Because of the versatility of the method, solver algorithms based on the FEM are implemented in numerous commercial computer-aided engineering programs.

The Boundary Element Method (BEM) is also a deterministic approach. Instead of dividing the complete volume domain into elements like in the FEM, the BEM only discretizes the surface of the acoustic domain [37]. This method is especially well suited for radiation problems in unbounded domains or for bounded domains in which the interaction with the structural domains is weak. Since the solution of the integral equation is reduced to the boundary, the resulting system of equations is notably smaller [38]. Nevertheless, the matrices of the system are fully populated and have complex, frequency-dependent coefficients, which in many applications leads to computational efforts comparable to those of the FEM.

Among the probabilistic approaches, also called energetic methods, the most widely used is the Statistical Energy Analysis (SEA). The fundamental idea of the SEA is that vibroacoustic energy behaves like thermal energy, in other words, it transmits from a system with higher energy to a lower energetic system at a rate proportional to the energy difference between them. In the probabilistic methods the domains are no longer divided into small elements, but into subsystems that can support given types of propagating waves [39]. Each subset is defined by its stored energy, which is directly linked to its average vibrational velocity. The fundamental equation of this technique is the power balance for each subsystem. The dynamic behavior of the systems is represented by loss factors. The damping loss factors govern the rate of energy dissipation inside a subsystem, while the coupling loss factors control the energy exchanges between the subsets. The main assumption is that the frequencies of resonance for each subsystem are uniformly distributed in the frequency bands analyzed [40]. This fact restricts the application of the SEA to the high frequency range in which the modal density stays almost constant. Because of a reduced number of unknown variables, this method is suitable for the analysis of large systems and at high frequencies. Nonetheless, the results predicted by the SEA describe the response of the system only averaged inside the subsets and in the selected frequency bands. Furthermore, the subdivision of the domains is not a straightforward process, and the determination of the coupling and loss coefficients remains an open question in most practical applications.

During the last two decades a handful of alternative numerical approaches have been proposed in order to overcome some of the difficulties mentioned above. For example, the energy FEM is based on the energetic principles of the SEA, but it solves the equations on a Finite Element discretization [41]. In this way it is possible to obtain a more detailed spatial distribution of the system behavior than with the SEA. Another option is the utilization of the Wave Based Method (WBM) [42]. In this approach the dynamic response of the domain variables is represented using wave functions, which are an exact solution of the governing partial differential equations. This means that the approximation errors are only related to the representation of the boundaries and the interfaces between domains [43]. The unknowns to be solved are the contributions of each wave function to the total response. The use of the WBM is limited to convex domains of relatively moderate geometrical complexity. Even if promising in terms of computational efficiency, the

application of these methods is still in development and exclusively only non-commercial implementations are available.

From the aforementioned characteristics we can conclude that the Finite Element Method is the most suitable numerical technique for the aimed application. First, it is an appropriate method in the frequency range of interest up to 2 kHz. Second, unlike the Boundary Element Method, the FEM allows a strong direct coupling between the structural and acoustic domains. This coupled calculation is necessary to capture the interaction between enclosed fluids and the surrounding structures. Third, the merging with experimental information within the framework of the hybrid approach requires a detailed spatial representation of the results, which cannot be retrieved when employing energetic approaches like the SEA.

3.2 Finite Element Method for vibroacoustic applications

This section first provides an overview of the partial differential equations governing the vibroacoustic behavior of fluid and structural domains. Next, the Finite Element formulation is derived from the dynamic equations for each kind of medium. Then, the coupling conditions between fluid and structure domains are outlined. The section concludes with a convergence analysis on a vibroacoustic system. The focus lies here on the harmonic response of the systems since the investigated phenomena are quasi-stationary. Under these conditions, the analysis in the frequency domain greatly reduces the computational effort with respect to the time domain methods [7]. Another general hypothesis along this section and the following chapters entails that the components behave linearly. Only small deformations around the equilibrium state occur and, therefore, the relationships between stress and strain remain in the linear regime. For simplification, the examined media are assumed to be isotropic, that is, the values of the material properties are identical in all directions. This is a valid supposition for the acoustic fluids and common structural media present in automotive constructions with exception of the fiber-reinforced components, which are outside of the scope of this thesis.

Description of fluid media

The variables that describe the fluid state at each position and time (\mathbf{x}, t) of a compressible fluid domain Ω_f are the fluid pressure p_f , the density ρ_f and the particle velocity \mathbf{v}_f . The wave equation in an ideal fluid can be directly derived from the combination of the equation for the conservation of mass, Newton's second law and the adiabatic equation of state [44]. Under the assumption of small perturbations from an equilibrium state (p_0, ρ_0) for the fluid pressure $p_f = p_0 + p'_f$ and density $\rho_f = \rho_0 + \rho'_f$, and neglecting all terms of order higher than one, the linear wave equation due to an acoustic excitation $Q(\mathbf{x}, t)$ reads:

$$\nabla^2 p'_f(\mathbf{x}, t) - \frac{1}{c_0^2} \frac{\partial^2 p'_f(\mathbf{x}, t)}{\partial t^2} = Q(\mathbf{x}, t) \quad (3.1)$$

The operator ∇ represents the divergence of the given field. The pressure perturbation p'_f is also referred to as the acoustic pressure. For convenience, we have employed the defi-

inition of the speed of sound:

$$c_0^2 = \left[\frac{\partial p_f(\mathbf{x}, t)}{\partial \rho_f(\mathbf{x}, t)} \right]_s \quad (3.2)$$

where the subscript s indicates that the process takes place at constant entropy. The velocity change associated to a pressure fluctuation is given by Eq. (3.3).

$$\frac{\partial \mathbf{v}'_f(\mathbf{x}, t)}{\partial t} = -\frac{1}{\rho_0} \nabla p'_f(\mathbf{x}, t) \quad (3.3)$$

Many vibroacoustic applications are centered on the response of the system to a harmonic excitation of the form $\exp(j\omega t)$, where j denotes the imaginary unit $\sqrt{-1}$, the angular frequency ω is defined as $\omega = 2\pi f$, with f the linear frequency. For example, the pressure field can be expressed as:

$$p'_f(\mathbf{x}, t) = \hat{p}'_f(\mathbf{x}) \exp(j\omega t) \quad (3.4)$$

The pressure field $\hat{p}'_f(\mathbf{x})$ is also a complex magnitude. In the following, we omit the primes for the perturbations and the time dependence term $\exp(j\omega t)$ for clarity. The resulting equations for a harmonic excitation are:

$$\nabla^2 \hat{p}_f(\mathbf{x}) + k^2 \hat{p}_f(\mathbf{x}) = \hat{Q}(\mathbf{x}) \quad (3.5)$$

$$j\omega \hat{\mathbf{v}}_f(\mathbf{x}) = -\frac{1}{\rho_0} \nabla \hat{p}_f(\mathbf{x}) \quad (3.6)$$

where the wave number k is defined as $k = \omega/c_0$. Eq. (3.5) is commonly known as the Helmholtz equation.

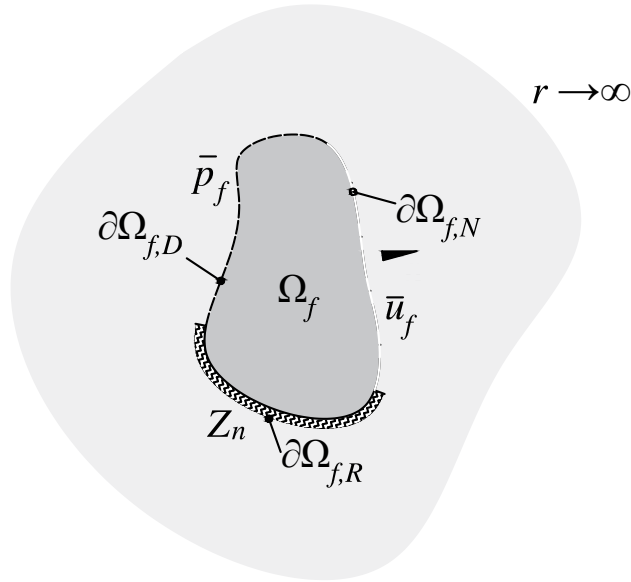


Figure 3.1: Schematic representation of the fluid domain (adapted from [45]).

Figure 3.1 displays a schematic fluid domain Ω_f together with the typical boundary conditions for acoustic problems, which are:

- The Dirichlet boundary condition: The acoustic pressure \bar{p}_f is set on the boundary.

$$\hat{p}_f = \bar{p}_f \quad \text{on} \quad \partial\Omega_{f,D} \quad (3.7)$$

- The Neumann boundary condition: The displacement field $\bar{\mathbf{u}}_f$ is specified on the boundary.

$$\frac{\partial \hat{p}_f}{\partial n} = \rho_0 \omega^2 \bar{\mathbf{u}}_f \cdot \mathbf{n} \quad \text{on} \quad \partial\Omega_{f,N} \quad (3.8)$$

where \mathbf{n} is the unit vector normal to the boundary surface.

- The Robin or impedance boundary condition: The relation between the acoustic pressure and normal velocity is given as $\hat{p}_f / (\hat{\mathbf{v}}_f \cdot \mathbf{n}) = Z_n$, with Z_n defined as the normal impedance on the boundary.

$$\frac{\partial \hat{p}_f}{\partial n} + j\rho_0 \omega \frac{\hat{p}_f}{Z_n} = 0 \quad \text{on} \quad \partial\Omega_{f,R} \quad (3.9)$$

Additionally, for unbounded fluid media the Sommerfeld radiation condition indicated in Eq. (3.10) must be satisfied [46]. This condition ensures that the wave amplitude vanishes at infinity and that no energy from infinity can be radiated into the field.

$$\lim_{r \rightarrow \infty} r \left(\frac{\partial \hat{p}_f}{\partial r} + jk \hat{p}_f \right) = 0 \quad (3.10)$$

An analytical solution of the system of equations formed by the Helmholtz equation (Eq. (3.5)) and the corresponding boundary conditions is only possible for very simple problems. For most applications, however, it is necessary to employ numerical approaches for the resolution. As indicated in Section 3.1, the Finite Element Method is the best suited technique for the current application. Next, the main steps to analyze a problem by the FEM are recalled. The detailed procedure for the derivation can be found in [45]. First, the weak integral Galerkin's formulation or functional of the wave equation is obtained (Eq. (3.11)). Next, the fluid domain is divided into a set of discrete elements. The typical elements employed to discretize fluid volumes are three-dimensional tetrahedral and hexahedral elements, but other could also be applied. After the discretization, the elementary matrices can be calculated. Then, these elementary matrices are assembled to form the global matrices with the help of the localization matrix. The boundary conditions are next imposed to the system.

$$\begin{aligned} \mathcal{W}(\hat{p}_f, \delta\hat{p}_f) = & \int_{\Omega_f} [\nabla \hat{p}_f \cdot \nabla \delta\hat{p}_f - k^2 \hat{p}_f \delta\hat{p}_f] dV - \int_{\delta\Omega_{f,N}} \rho_0 \omega^2 \bar{\mathbf{u}}_f \cdot \mathbf{n} \delta\hat{p}_f dS \\ & + \int_{\delta\Omega_{f,R}} j \frac{\rho_0 \omega}{Z_n} \hat{p}_f \delta\hat{p}_f dS = 0 \end{aligned} \quad (3.11)$$

Finally, the application of the stationarity condition on the discretized functional results in the matrix system described by Eq. (3.12). The vector $\{\hat{p}_f\}$ contains the unknowns of the system. For a fluid medium, these unknowns or degrees of freedom (DOF) are the values of acoustic pressure at the discretization points.

$$(-\omega^2 [Q] + j\omega [A] + [H]) \{\hat{p}_f\} = \{\hat{Q}\} \quad (3.12)$$

The global matrices $[Q]$, $[A]$ and $[H]$ are square, banded and symmetric. The matrix $[Q]$ relates the pressure to the displacements and represents a compressibility matrix. The matrix $[H]$ represents an inverse mass or mobility matrix, linking the pressure to the acceleration. In the literature these matrices are also referred to as acoustic mass matrix and acoustic stiffness matrix, analogously to their counterparts in the structural FEM. The matrix $[A]$ corresponds to the acoustic damping matrix induced by the impedance boundary condition [47]. The vector $\{\hat{Q}\}$ includes all the external acoustical loads.

Description of elastic solid media

The equations governing the dynamic behavior of an elastic solid occupying a volume Ω_s can be obtained from the combination of the equations of conservation of mass and conservation of momentum together with the constitutive law of the solid. The linearized equation in Eq. (3.13) is derived under the assumption of small deformations around the equilibrium state. The mass density of the solid is indicated with ρ_s and the external excitation \mathbf{F}_b is a body force per unit volume.

$$\rho_s \frac{\partial^2 \mathbf{u}_s(\mathbf{x}, t)}{\partial t^2} = \nabla \underline{\sigma}_s(\mathbf{x}, t) + \rho_s \mathbf{F}_b(\mathbf{x}, t) \quad (3.13)$$

The component σ_s^{ij} of the stress tensor $\underline{\sigma}_s$ is defined as the i -th component of the force applied to a unit area perpendicular to the j -axis direction. For a linear elastic solid, the constitutive or Hooke's law of the material relates the strain tensor $\underline{\varepsilon}$ of the solid to the acting stress through the stiffness tensor $\underline{\mathbf{C}}$ (Eq. (3.14)). The strain tensor can be calculated from the displacement field \mathbf{u}_s as indicated in Eq. (3.15).

$$\underline{\sigma}_s(\mathbf{x}, t) = \underline{\mathbf{C}} \underline{\varepsilon}(\mathbf{x}, t) \quad (3.14)$$

$$\underline{\varepsilon}(\mathbf{x}, t) = \frac{1}{2} \left(\nabla \mathbf{u}_s(\mathbf{x}, t) + (\nabla \mathbf{u}_s(\mathbf{x}, t))^T \right) \quad (3.15)$$

The operator T denotes the transpose of the tensor. Under an excitation with harmonic time dependence $\exp(j\omega t)$ the governing equation Eq. (3.13) can be rewritten as:

$$-\rho_s \omega^2 \hat{\mathbf{u}}_s(\mathbf{x}) = \nabla \hat{\underline{\sigma}}_s(\mathbf{x}) + \rho_s \hat{\mathbf{F}}_b(\mathbf{x}) \quad (3.16)$$

One can impose two basic types of boundary conditions to elastic solid media as illustrated in Figure 3.2:

- The Dirichlet boundary condition: The displacement field $\bar{\mathbf{u}}_s$ is specified on the boundary.

$$\hat{\mathbf{u}}_s = \bar{\mathbf{u}}_s \quad \text{on} \quad \partial\Omega_{f,D} \quad (3.17)$$

- The Neumann boundary condition: The contact forces per unit area $\bar{\mathbf{F}}$ are specified on the boundary.

$$\hat{\underline{\sigma}}_s \cdot \mathbf{n} = \bar{\mathbf{F}} \quad \text{on} \quad \partial\Omega_{f,N} \quad (3.18)$$

The application of the principle of virtual displacements leads to the following variational formulation for an elastic solid:

$$\mathcal{W}(\hat{\mathbf{u}}_s, \delta \hat{\mathbf{u}}_s) = \int_{\Omega_s} \hat{\underline{\varepsilon}}(\hat{\mathbf{u}}_s) : \underline{\mathbf{C}} : \hat{\underline{\varepsilon}}(\delta \hat{\mathbf{u}}_s) dV - \int_{\Omega_s} \rho_s \left[\hat{\mathbf{F}}_b + \omega^2 \hat{\mathbf{u}}_s \right] \delta \hat{\mathbf{u}}_s dV - \int_{\partial\Omega_{s,N}} \bar{\mathbf{F}} \delta \hat{\mathbf{u}}_s dS = 0 \quad (3.19)$$

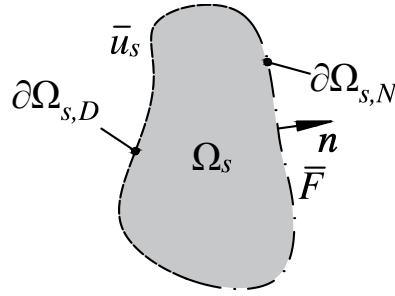


Figure 3.2: Schematic representation of the solid domain (adapted from [45]).

The combination of Eq.(3.19) together with the corresponding boundary conditions forms the base on which the Finite Element discretization is conducted. A solid domain is usually divided into discrete volume elements analogously to a fluid domain. After that, the elementary matrices describing each finite element are combined to build the global matrices of the solid medium. A complete overview of the calculations to obtain the matrices is found, for instance, in [48]. The resulting system of equations in the frequency domain has the form:

$$(-\omega^2 [M] + j\omega [D] + [K]) \{\hat{u}_s\} = \{\hat{F}\} \quad (3.20)$$

The matrices $[M]$ and $[K]$ denote the mass matrix and stiffness matrix of the elastic solid, respectively. The damping matrix $[D]$ includes the losses in the solid medium. Here, a viscous damping model has been applied, but other models may also be used. The external forces acting on the elastic solid are condensed in the vector $\{\hat{F}\}$. The degrees of freedom of the system $\{\hat{u}_s\}$ are the three unknown displacement components at each nodal point of the Finite Element discretization.

In many practical applications the elastic solids consist of structures in which one dimension is much smaller than the other two. If such solid domains are discretized by means of standard volume elements, inaccuracies occur because of the so-called shear locking. This results in an overestimation of the shear energy as the thickness to length ratio of the elements decreases. To overcome this issue an under integration of the shear energy is usually recommended. Alternatively, special thin shell type finite elements are used [49, 50]. These elements have three displacement degrees of freedom and additionally three rotational degrees of freedom at each node.

One drawback of the thin shell elements is that, since they include rotational degrees of freedom, the coupling to other solid elements is not straightforward [51]. To deal with such problems different coupling strategies are available [52]. As another option, one can use a special class of elements known as solid or continuous shell elements, which are three-dimensional elements like the standard solid ones. Nevertheless, they circumvent the sensitivity to the locking phenomena by techniques like the Assumed Natural Strain or Enhanced Assumed Strain, which adopt certain distributions of the strain along the thickness as shown in [53] or in [54]. In this thesis solid shell elements have been employed for the modeling of thin plates.

Vibroacoustic coupling

In vibroacoustic applications we typically deal with the interaction of a fluid domain with an elastic solid medium. Depending on whether the fluid domain is bounded or

unbounded, the problems are classified into interior, exterior or mixed problems. At the interface between the two media $\partial\Omega_{sf}$ the continuity relations have to be satisfied. On the one hand, the displacements in the direction normal to the interface \mathbf{n} need to be compatible:

$$\frac{\partial \hat{p}_f}{\partial n} = \rho_0 \omega^2 \hat{\mathbf{u}}_s \cdot \mathbf{n} \quad \text{on} \quad \partial\Omega_{sf} \quad (3.21)$$

On the other hand, the pressure loading from the fluid must equal the stresses on the boundary of the structure:

$$\hat{p}_f \mathbf{n} = \hat{\boldsymbol{\sigma}}_s \cdot \mathbf{n} \quad \text{on} \quad \partial\Omega_{sf} \quad (3.22)$$

The system of equations for the coupled system is given in Eq. (3.23). It results from the combination of the two additional compatibility conditions (Eq. (3.21) and (3.22)) together with the governing equations for the fluid (the Helmholtz equation in Eq. (3.5)), for the elastic solid (the elasto-dynamic equation in Eq. (3.16)), and the corresponding boundary conditions for the fluid and solid domains.

$$\begin{bmatrix} [K] - \omega^2 [M] & - [C_{sf}] \\ -\omega^2 [C_{sf}]^T & [H] - \omega^2 [Q] \end{bmatrix} \begin{Bmatrix} \{\hat{\mathbf{u}}_s\} \\ \{\hat{p}_f\} \end{Bmatrix} = \begin{Bmatrix} \{\hat{F}\} \\ \{\hat{Q}\} \end{Bmatrix} \quad (3.23)$$

The matrix $[C_{sf}]$ is the surface coupling matrix between the fluid and the elastic solid. The unknowns of the system are the displacements of the structure $\{\hat{\mathbf{u}}_s\}$ at the nodes of the solid body and the acoustic pressure $\{\hat{p}_f\}$ at the nodes of the fluid.

Convergence analysis

To ensure the convergence of the Finite Element solution, a sufficiently fine discretization for both the fluid and the structural components has to be chosen. The error associated to the approximation of the solution is proportional to the product of the wave number and the element size. This means that for higher frequencies smaller elements are necessary in order to keep the error delimited. As a rule of thumb, it is a common practice to make use of 8 to 10 linear elements, or 4 to 6 quadratic elements for the shortest wavelength of interest [55, 56]. Nevertheless, as the frequency increases, the pollution error becomes larger and more elements per wavelength are required to obtain a constant global error, as shown by Bayliss *et al.* [57]. This issue especially affects to shape functions of lower order like linear and quadratic elements.

The wavelength λ_f of a longitudinal wave, sometimes also called compressional wave, propagating in a fluid medium is given by:

$$\lambda_f = \frac{c_0}{f} \quad (3.24)$$

The frequency range of interest covers up to 2.5 kHz. At this frequency the compressional wave propagating in the fluid has a wavelength of 152 mm. In the case of elastic solids, because of their ability resist shear deformation, not only longitudinal waves are present like in fluid media, but also shear waves can propagate inside the material. The wavelength $\lambda_{s,l}$ of the compressional wave propagating inside a plate structure is:

$$\lambda_{s,l} = \frac{1}{f} \sqrt{\frac{E}{\rho_s (1 - \nu^2)}} \quad (3.25)$$

with E representing the Young's modulus and ν the Poisson's coefficient. The shear wavelength $\lambda_{s,s}$ is given by:

$$\lambda_{s,s} = \frac{1}{f} \sqrt{\frac{G}{\rho_s}} \quad (3.26)$$

where the shear modulus G for isotropic materials is related to the elasticity modulus and the Poisson's coefficient by $G = E/(2(1 + \nu))$. The structures in which one or two dimensions are small compared to the internal wavelength, such as beams and plates, radiate the most sound energy by flexural bending. The wavelength $\lambda_{s,b}$ associated to bending waves is:

$$\lambda_{s,b} = 2\pi \sqrt[4]{\frac{D}{\rho_s h_s \omega^2}} \quad (3.27)$$

The parameter h_s is the thickness of the plate, and the flexural rigidity D is defined as $D = Eh_s^3/(12(1 - \nu^2))$.

In order to check the suitability of the chosen Finite Element discretization, we evaluated the acoustic power radiated by a thin plate. The system object of the analysis is shown in Figure 3.3. It is formed by a square steel plate of side length one meter and 0.76 mm thickness. This value is a common thickness for automotive constructions. Standard material properties have been employed for the steel plate ($E = 2.1e11$ Pa, $\nu = 0.31$, $\rho_s = 7772$ kg m⁻³, and a structural damping coefficient $\eta_s = 0.01$). The highest examined frequency at 2.5 kHz has a wavelength of 55 mm and is associated to the bending wave. The plate was discretized with quadratic solid shell elements of maximum size e_s . On the edges of the plate the displacement in the direction of the thickness was set to zero to represent simply supported boundary conditions.

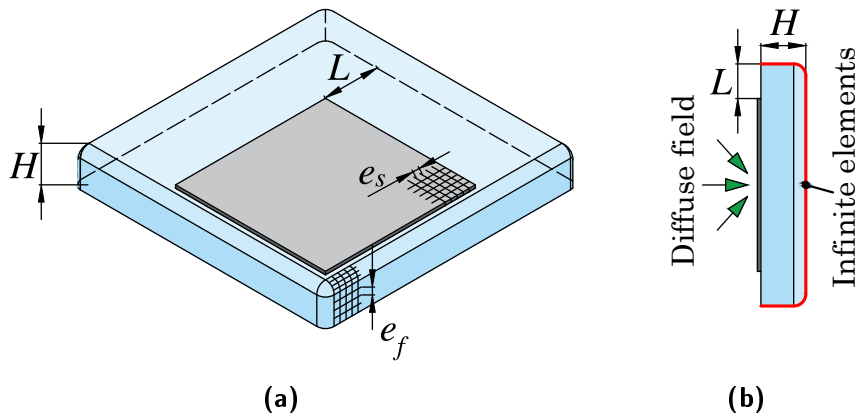


Figure 3.3: (a) Isometric and (b) side views of the vibroacoustic system employed for the convergence analyses including the examined parameters: maximum element size for the structural e_s and fluid e_f components, lateral extent L and height H of the finite fluid domain.

The plate was coupled on one of its faces to a semi-infinite fluid into which it radiated. This semi-infinite fluid domain was modeled by the combination of a finite fluid volume together with infinite elements applied on its uppermost layer, which is marked in red in Figure 3.3b. This is a standard procedure to numerically extend a fluid domain and thus to fulfill the Sommerfeld radiation condition [37] without requiring an absorbing boundary

condition to prevent reflections [58]. Each infinite node carries a single acoustic pressure degree of freedom. The infinite domain is defined by a reference ellipsoidal coordinate system with the radial coordinate r and the angular coordinates (θ, φ) . In the present application the Astley-Leis conjugated formulation is implemented [59]. The associated shape function Φ has the form:

$$\Phi(r, \theta, \varphi) = \exp(-jkr) \sum_{n=1}^m \frac{F_n(\theta, \varphi)}{r^n} \quad (3.28)$$

where m is the radial interpolation order and $F_n(\theta, \varphi)$ is a regular function continuous in the infinite fluid domain. The test function ϖ is the complex conjugate of the shape function weighted by the geometrical factor $1/r^2$:

$$\varpi(r, \theta, \varphi) = \exp(jkr) \sum_{n=1}^m \frac{F_n(\theta, \varphi)}{r^{n+2}} \quad (3.29)$$

The main advantage of this formulation is that the resulting integrand does not include any oscillating functions since the frequency-dependent terms cancel out.

The finite volume of the receiving domain was discretized with linear tetrahedral and hexahedral elements of maximum length e_f . The fluid domain had a height H and an extended lateral length L with respect to the edges of the plate. The size of this domain should be large enough in order to allow the fluid to propagate freely and to avoid that energy is reflected from the infinite medium. Over the outer surface of the receiving domain the total radiated power could be retrieved.

On the other face of the steel plate a diffuse pressure field was applied, which is indicated by the green arrows in Figure 3.3b. The diffuse excitation was represented in the numerical model by a superposition of plane waves having randomly determined phases and directions. The statistical information defining the waves can be summarized in the cross power spectral density matrix (CPSD). By means of a Cholesky decomposition of the CPSD matrix one can directly obtain the pressure distribution acting on the input surface of the steel plate, as described in [60]. This definition of the incident field avoided the explicit modeling of the sending room, thus significantly reducing the size of the numerical domain.

The chosen method for solving the system of linear equations in Eq. (3.23) was a direct frequency analysis. This means that the response of the system was only computed at a number of discrete frequencies. Alternatively, one may make use of a modal superposition technique. However, modal approaches are not suitable for the resolution of systems including poroelastic media since they have a high dissipative, frequency-dependent behavior, as indicated later in Chapter 4. Because each frequency step is solved independently, the calculation time proportionally increases with the number of selected frequencies. Nevertheless, the frequency resolution for the direct analysis needs to be fine enough, so that the frequency averaged results, like in third octave bands, include all the relevant information. For instance, the averaged power W in a frequency band i between $f_{min,i}$ and $f_{max,i}$ for a continuous frequency spectrum is given by:

$$\langle W \rangle_i = \frac{1}{f_{max,i} - f_{min,i}} \int_{f_{min,i}}^{f_{max,i}} W(f) df \quad (3.30)$$

The brackets $\langle \rangle$ indicate that the quantity is averaged. If only a finite number of frequency steps N is calculated, the average power within a frequency band is approximated by:

$$\langle W \rangle_i \approx \frac{1}{f_{max,i} - f_{min,i}} \sum_{j=1}^N W(f_j) \cdot (f_j^+ - f_j^-) \quad (3.31)$$

where f_j^- and f_j^+ are the geometric mean of the discrete frequency f_j and the previous and following discrete frequency values inside the band, respectively. The difference $(f_j^+ - f_j^-)$ gives therefore the frequency range in which it is assumed that the calculated power $W(f_j)$ remains constant.

In order to reduce the total computation time, the use of a non-uniform frequency step is advisable, since the energetic distribution becomes more homogeneous as the frequency increases and single eigenmodes are not longer distinguishable. Some preliminary tests were conducted to determine a sufficient frequency resolution to obtain accurate results. To that end, the power radiated by the introduced setup with a simply supported steel plate under a diffuse field excitation was first calculated with a 1 Hz frequency step. The averaged radiated power in third octave bands was then obtained according to Eq. (3.31) for different multiples of this resolution. In Figure 3.4 the results are displayed for the low and the high frequency ranges.

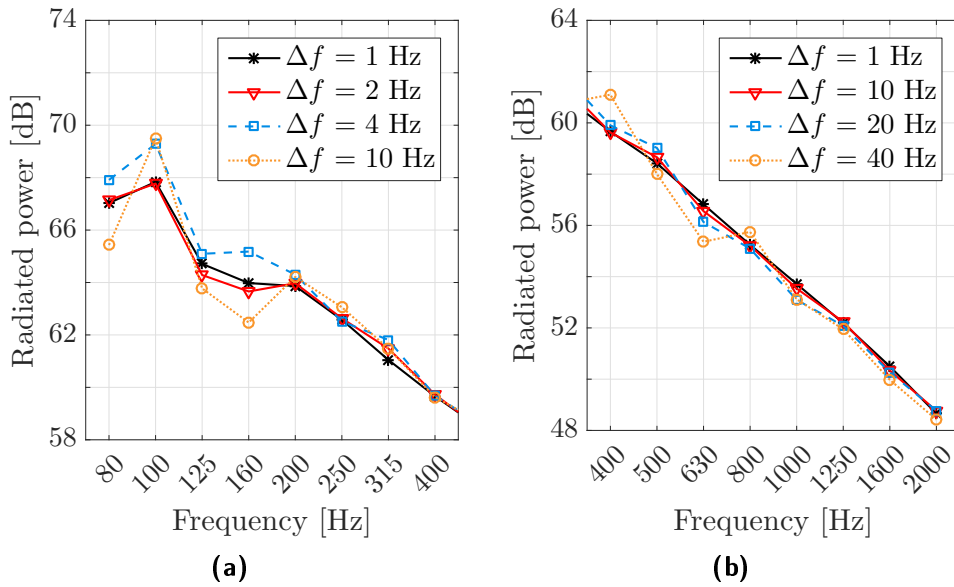


Figure 3.4: Convergence of the radiated power averaged in third octave bands for different frequency resolutions: (a) low frequency range, (b) high frequency range.

By comparison with the reference solution for $\Delta f = 1$ Hz it is possible to identify the required resolution for reliable results. In all the following models we employ the non-uniform frequency step below:

$$\Delta f = \begin{cases} 2 \text{ Hz,} & \text{for } f < 250 \text{ Hz} \\ 10 \text{ Hz,} & \text{for } 250 \text{ Hz} \leq f \leq 1250 \text{ Hz} \\ 20 \text{ Hz,} & \text{for } f > 1250 \text{ Hz} \end{cases}$$

Another important aspect to ensure the comparability of the results is the diffusivity of the excitation, which is controlled by the number of realizations chosen for the Cholesky decomposition. The excitation is defined as diffuse if the response is not affected in the case that this number is increased, that is, if additional plane wave sources with other phases and directions are included. For verification we have evaluated the transmission of the acoustic energy through the steel plate with different numbers of realizations between 10 and 50. The results are evaluated in terms of the transmission loss (TL). This quantity is defined as the ratio between the incident power W_{in} and the radiated power W_{rad} in linear units (usually watt). Its value is commonly given in decibel scale as indicated in Eq. (3.32).

$$\text{TL [dB]} = 10 \log \frac{W_{\text{in}} [\text{watt}]}{W_{\text{rad}} [\text{watt}]} \quad (3.32)$$

The comparison of the transmission loss performance for different numbers of realizations are summarized in Figure 3.5. For clarity the results are displayed averaged in third octave bands. Since the variations are small, the transmission loss of the setup with 50 realizations is taken as reference, and the deviation of the TL with respect to this reference is calculated. The percent deviation of a quantity X_i is calculated according to Eq. (3.33). For the models with 30 and 40 realizations the maximum deviation was approximately 0.5 %, which is an acceptable fluctuation. Therefore, for all the following analyses a total of 30 realizations was chosen for the decomposition.

$$\Delta X [\%] = \frac{|X_i - X_{\text{ref}}|}{X_{\text{ref}}} \cdot 100 \quad (3.33)$$

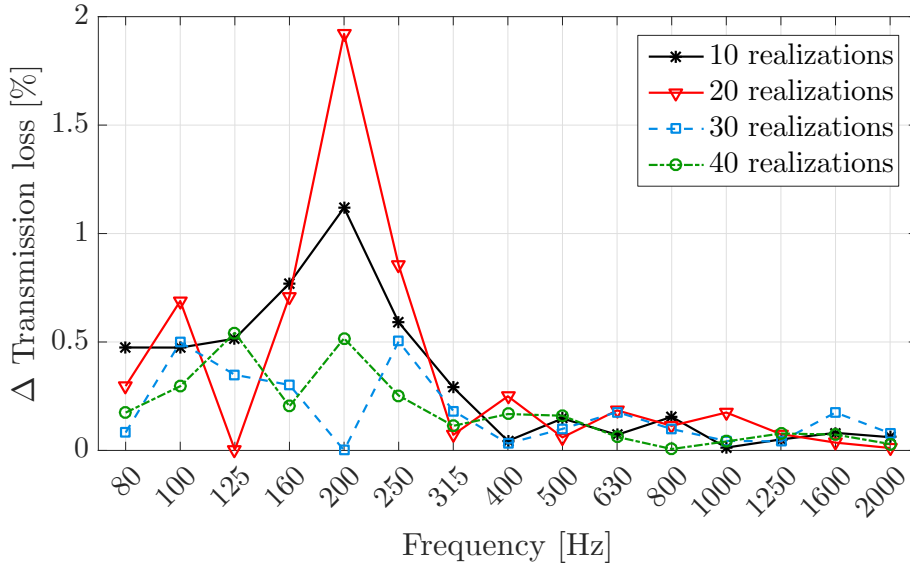


Figure 3.5: Percent deviation in the transmission loss results for different numbers of realizations for the Cholesky decomposition. The reference solution was calculated with 50 realizations.

On the receiving side it is essential to ensure that the Sommerfeld radiation condition is fulfilled, so that spurious reflections at the interface between the finite and infinite elements are prevented. Moreover, the radiation characteristics towards infinity have to be correctly represented. The accuracy of an infinite element relies on the choice of the shape functions,

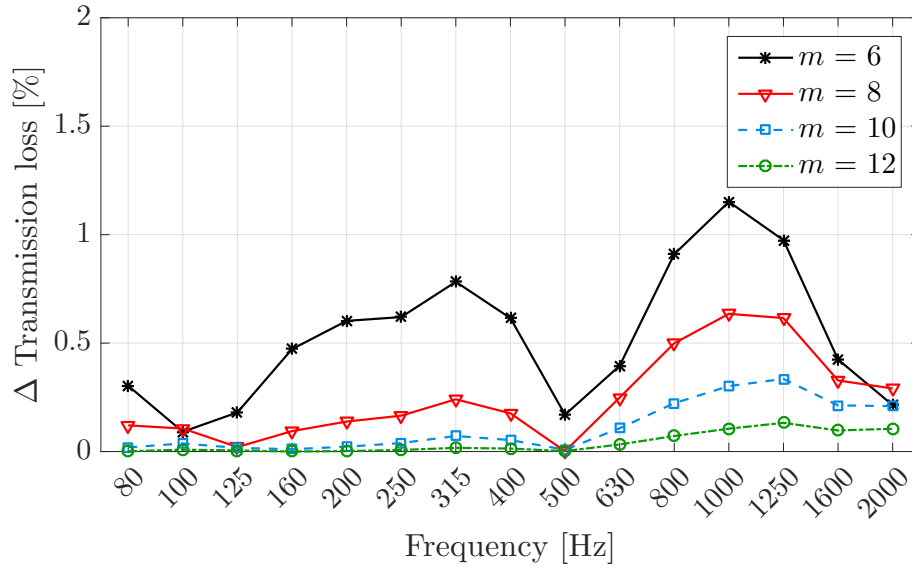


Figure 3.6: Percent deviation in the transmission loss results for different polynomial orders of the infinite elements. The reference solution was calculated with $m = 14$.

typically polynomial or radial functions, and on the order of interpolation m [58]. As the frequency of the analysis rises, the radiation pattern becomes more complex and the higher order terms gain importance. For the radiating plate configuration interpolation orders for the infinite elements between 6 and 14 were tested. Figure 3.6 shows the calculated results, where the solution with the highest interpolation order serves as reference. Functions of 10th and 12th order gave deviations under 0.5 % in the frequency range of interest. The interpolation order $m = 10$ was chosen as suitable for the aimed application.

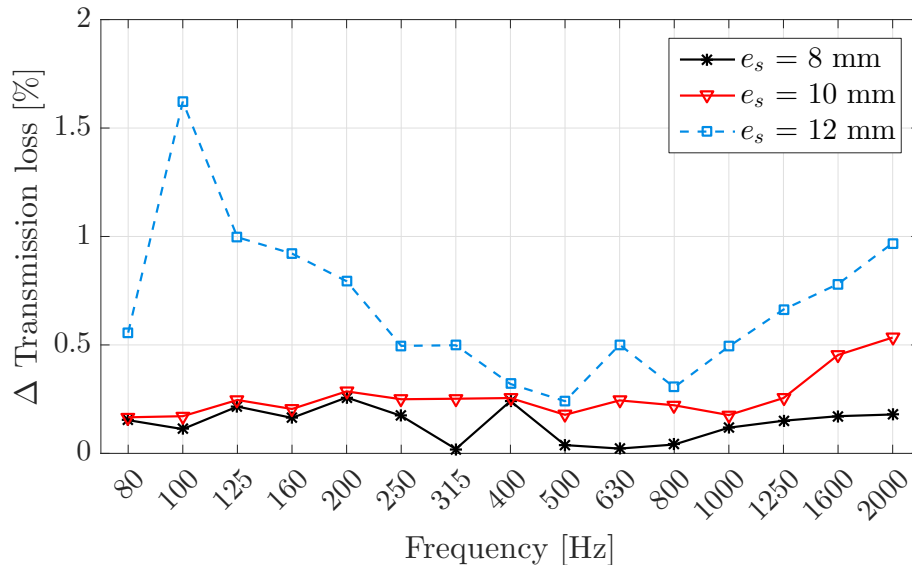


Figure 3.7: Percent deviation in the transmission loss results for different fluid element sizes. The reference solution was calculated with $e_s = 6$ mm.

Other parameters that influence the convergence of the solution and were also analyzed are marked in Figure 3.3. They include the maximum length of the elements in the steel

plate e_s , the maximum length of the elements in the fluid domain e_f , and the lateral L and vertical H dimensions of the fluid domain.

Figure 3.7 displays the deviation in the transmission loss for different discretizations of the steel plate. The results with $e_s = 12$ mm presented a large deviation in the low frequency range due to small shifts in the calculation of the eigenfrequencies. Above 800 Hz for the 12 mm elements and above 1250 Hz for the 10 mm elements the solution diverged from the reference. Therefore, a maximum element size of 8 mm was selected for the steel plate, which corresponds to seven quadratic elements per wavelength at the highest examined frequency.

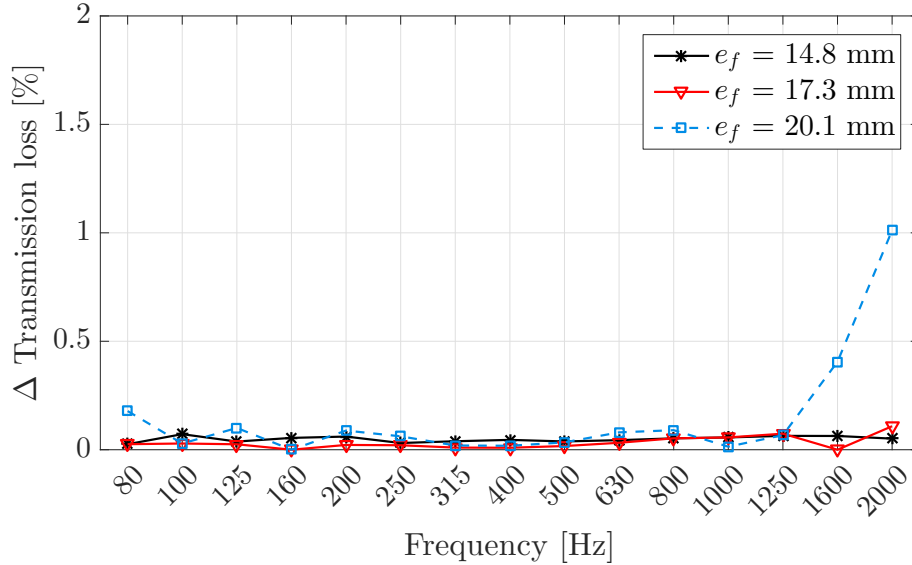


Figure 3.8: Percent deviation in the transmission loss results for different fluid element sizes. The reference solution was calculated with $e_f = 12.0$ mm.

The discretization of the finite fluid domain is analyzed in Figure 3.8. The reference value employed for the maximum element size e_f is 12 mm. The solution with the coarsest discretization, $e_f = 20.1$ mm, diverged above 1600 Hz, whereas the deviation for the other two investigated discretizations remained under 0.1% in the complete frequency range of interest. For that reason, the finite fluid domain was discretized with combined tetrahedral and hexahedral elements whose maximum element size is 17.3 mm. At 2.5 kHz this resolution is equivalent to nine linear elements per wavelength.

In Figure 3.9 the impact of the size of the finite fluid volume is detailed. The inspection of the results showed that the height of the fluid domain H had the greatest effect on the total results, whereas the lateral dimension L presented a secondary influence. In the studied state, due to the flat geometry and the diffuse field excitation, most of the energy was transmitted in the direction normal to the plate. Hence, the interaction of the waves with the finite fluid domain is more sensitive to the size in that direction. A minimum number of finite element layers between the plate surface and the interface should be employed in order to ensure that the radiation pattern is not affected by the dimensions of the receiving domain. The size of the fluid volume for the investigations in the further chapters was set to $L = 100$ mm and $H = 100$ mm, for which the deviation to the reference solution is lower than 0.5%.

A cut view of the resulting fluid mesh is represented in Figure 3.10. One can identify the hexahedral and the tetrahedral elements employed. The use of a hexahedral core helps to

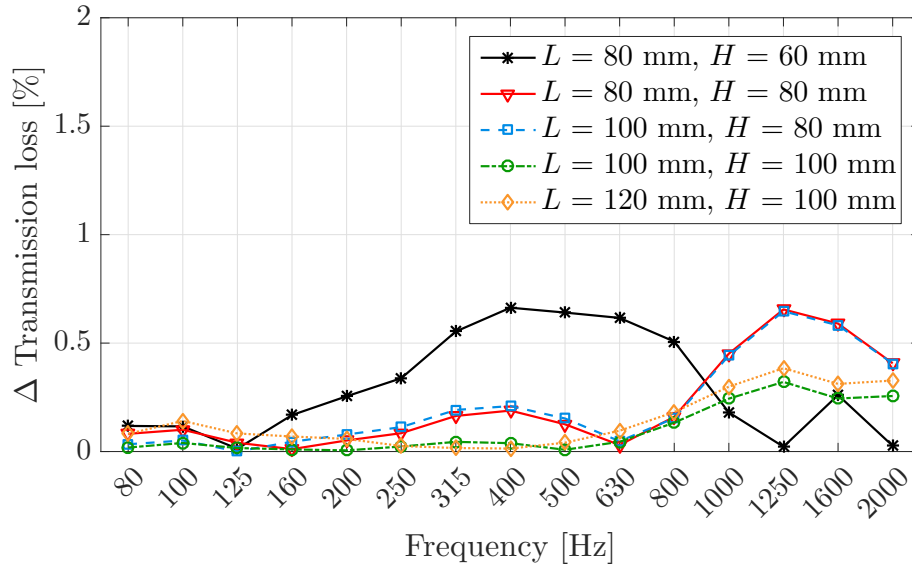


Figure 3.9: Percent deviation in the transmission loss results for different fluid volume sizes. The reference solution was calculated with $L = 120$ mm, $H = 120$ mm.

reduce the total number of elements, whereas the tetrahedral outer layers are necessary to adapt to curved geometries as well as to connect to components with other element sizes.

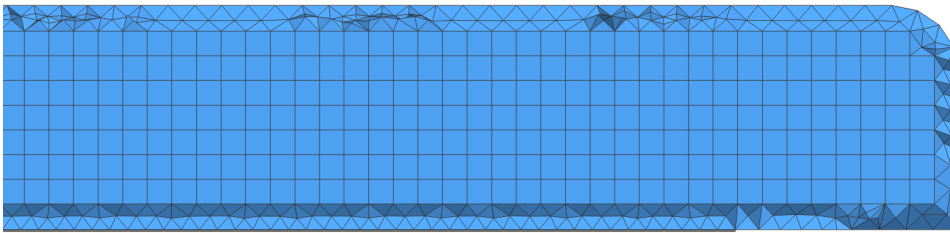


Figure 3.10: Cut view of the finite fluid mesh.

Chapter 4

Modeling of poroelastic components

The presence of noise control treatments (NCT) strongly modifies the transmission of the acoustic energy through the structural and acoustic components, as previously indicated in Chapters 1 and 2. These sound proofing materials can dissipate energy by means of absorption, damping and insulation. Consequently, a reliable model for the prediction of the airborne sound propagation should consider the impact of the sound packages on the global system response. Many of the trim components employed in the automotive industry contain one or more layers of poroelastic materials, like the spring-mass systems and absorbers marked in the Figures 4.1 and 4.2.

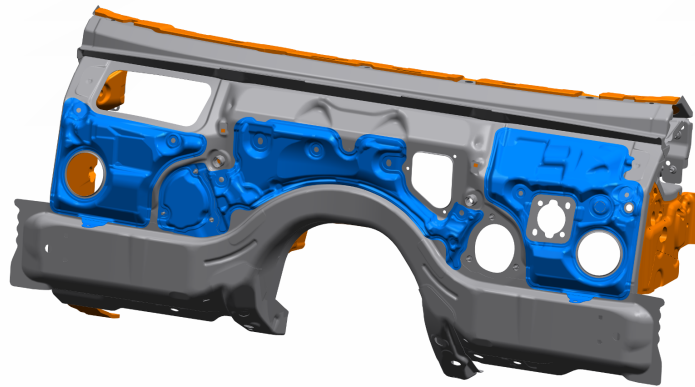


Figure 4.1: Poroelastic noise control treatments applied on the engine compartment side of the firewall. The absorbers are marked in blue.

Poroelastic materials consist of an elastic solid phase, also referred to as frame or skeleton, and a fluid phase that fills the pores in the solid. The interaction between the two phases controls the dynamic behavior of the medium. Besides the structural damping losses typical of the elastic solids and the thermal and viscous losses present in fluid media, poroelastic materials can dissipate energy by two additional mechanisms. On the one hand, the friction between the fluid and the walls of the pores increases the viscous losses. On the other hand, there exists an inertial coupling effect due to different accelerations between the two phases.

The biphasic nature of the poroelastic media is therefore responsible for their good ability to reduce energy, which makes them very effective in the application as acoustic treatments. Nevertheless, this complex dissipative behavior is, in turn, difficult to capture in a mathematical model. In Section 4.1 the main concepts and equations underlying the poroelasticity theory are reviewed. A special focus is drawn on the physical meaning of the material parameters and how they can be determined. After that, in Section 4.2, the Finite Element implementation for the resolution of vibroacoustic problems with poroelas-

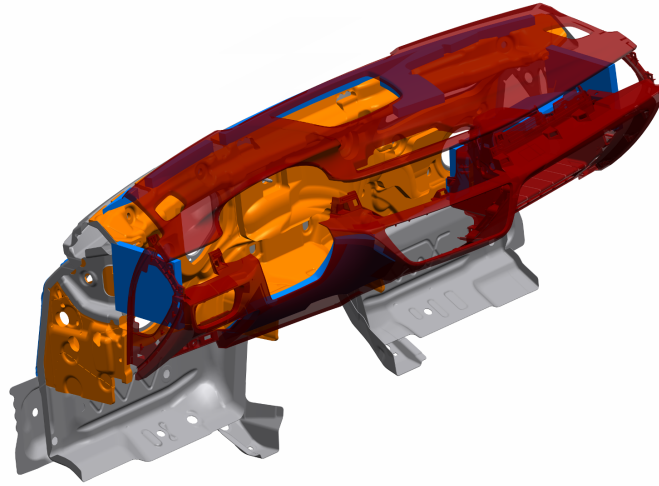


Figure 4.2: Poroelastic noise control treatments on the passenger compartment side of the firewall. The absorbers are marked in blue, the spring-mass systems in orange and the dashboard in dark red.

tic components is presented. Lastly, the accuracy of a numerical model for a vibroacoustic system including poroelastic acoustic treatments is analyzed.

4.1 Description of poroelastic media

The first general concept for the dynamic behavior of a poroelastic medium including the elastic effects of the frame is attributed to M.A. Biot, who gave a theoretical description of the coupled wave propagation taking place. The work by Biot was published in two papers, divided into the low frequency [61] and the high frequency range [62]. The originality of this approach lies in the assumption that the biphasic material can be described as a homogeneous continuum where the solid and the fluid phases are superposed in space and time. This theory first found application for porous rocks filled with a heavy fluid such as water. Later, the theory was revised by Allard for the sound propagation in porous media [63]. Over the years, several improvements have been proposed, especially for the middle frequency range and to account for other dispersion and attenuation mechanisms, as for example the work by Johnson [64].

The poroelasticity equations are obtained from the combination of the dynamic strain-stress relations for the elastic solid phase, the Navier-Stokes equations for the fluid phase, and the Darcy's law of diffusivity. As mentioned above, the main assumption of the theory is homogeneity, in other words, the fluid and solid phases are simultaneously present at every point in the medium. That way, the resolution of the medium at the microscopic scale is avoided. This is a valid approach if the wavelengths of interest are large compared to both the pores size and to the dimensions of the volume of homogenization [65]. Other underlying hypotheses in the derivation include small deformations of the elastic solid, linear wave propagation, that the filling fluid is initially at rest, and that all the pores are connected. Again, harmonic time dependence $\exp(j\omega t)$ is presumed in this research. The equations shown here are for isotropic media in which the material properties are the same in all directions. However, the homogenization procedure of the Biot theory can also be applied to anisotropic and orthotropic poroelastic components as indicated in [66, 67].

The original motion equations formulated by Biot are in terms of the displacement fields for the solid and fluid phases. However, we preferably make use of the mixed displacement-pressure (\mathbf{u}, p) formulation by Atalla [68]. This derivation in terms of skeleton displacements \mathbf{u} and fluid pressure p presents two main advantages over the original formulation. First, the number of state variables is reduced from six (three displacement components for each phase) to four (three displacement components for the solid phase and the acoustic pressure for the fluid phase). The variable change for the fluid component does not affect the accuracy since no additional assumptions are introduced [69]. Second, the (\mathbf{u}, p) formulation facilitates the coupling to fluid components because the same degree of freedom as for fluid materials is used. The resulting governing equations for poroelastic media are:

$$\nabla \cdot \hat{\underline{\sigma}}^s(\hat{\mathbf{u}}) + \omega^2 \tilde{\rho} \hat{\mathbf{u}} + \tilde{\gamma} \nabla \hat{p} = 0 \quad (4.1)$$

$$\nabla^2 \hat{p} + \frac{\tilde{\rho}_{22}}{\tilde{R}} \omega^2 \hat{p} + \frac{\tilde{\rho}_{22}}{\phi^2} \tilde{\gamma} \omega^2 \nabla \cdot \hat{\mathbf{u}} = 0 \quad (4.2)$$

The tilde symbol $\tilde{}$ in Eq. (4.1) and (4.2) indicates that the corresponding material parameter is complex and frequency-dependent. This system of differential equations has the form of a fluid-structure interaction (FSI) problem. However, contrary to a classical FSI, where the interaction is limited to the interfaces between the two spatially separated fluid and solid phases, the coupling in a poroelastic medium is of volume nature [67] because the two phases are superposed in space and time. The open porosity ϕ gives the ratio of free fluid volume to the total volume of the material. Under this definition, the fluid restrained inside closed pores is included in the solid phase volume.

The stress tensor $\hat{\underline{\sigma}}^s(\hat{\mathbf{u}})$ corresponds to the elastic solid assumed in vacuo, that is, when the filling fluid is drained off. It is only dependent on the strain state of the frame and can be calculated analogously to an elastic solid with the help of the stress-strain relations in Eq. (3.14) and (3.15). The coefficient $\tilde{\gamma}$ couples the dynamics of the two phases and is given by Eq. (4.3) [68].

$$\tilde{\gamma} = \phi \left(\frac{\tilde{\rho}_{12}}{\tilde{\rho}_{22}} - \frac{\tilde{Q}}{\tilde{R}} \right) \quad (4.3)$$

For simplification, the effective density $\tilde{\rho}$ relating the different mass coefficients has been employed in Eq. (4.1):

$$\tilde{\rho} = \tilde{\rho}_{11} - \frac{\tilde{\rho}_{12}^2}{\tilde{\rho}_{22}} \quad (4.4)$$

Several mass coefficients are present in the equations to include the viscous interactions between the two phases and the corresponding viscous losses. There is a mass coefficient associated to the frame $\tilde{\rho}_{11}$, one related to the fluid phase $\tilde{\rho}_{22}$, and one associated to the viscous and inertial coupling $\tilde{\rho}_{12}$. Their definitions are given in Eq. (4.5), (4.6) and (4.7).

$$\tilde{\rho}_{11} = (1 - \phi) \rho_s + \phi \rho_0 (\tilde{\alpha} - 1) \quad (4.5)$$

$$\tilde{\rho}_{22} = \phi \rho_0 \tilde{\alpha} \quad (4.6)$$

$$\tilde{\rho}_{12} = -\phi \rho_0 (\tilde{\alpha} - 1) \quad (4.7)$$

The parameter ρ_s is the mass density of the material from which the solid frame is made of, and ρ_0 is the mass density of the filling fluid. The complex coefficient $\tilde{\alpha}$ is known as the dynamic tortuosity and accounts for the dissipation due to the viscous effects in the fluid phase. A proper constitutive model is required for the expression of the dynamic tortuosity. Different models can be found in the literature, as for example the semi-phenomenological ones introduced by Johnson [64], by Pride [70] or by Wilson [71]. These models analyze the phenomena of the viscous friction and the inertia interactions. In this research we make use of the Johnson's model, where the dynamic tortuosity is given by:

$$\tilde{\alpha} = \alpha_\infty - j \frac{\phi \sigma}{\omega \rho_0} \sqrt{1 + j \frac{4\alpha_\infty^2 \eta_0 \rho_0 \omega}{(\sigma \Lambda \phi)^2}} \quad (4.8)$$

The dynamic viscosity of the filling fluid is represented by η_0 . The good agreement of the chosen model with the measured dynamic densities for different kinds of foams was proved in [72]. The expression in Eq. (4.8) links the microscopic viscous effects at a local level with the macroscopic behavior of the homogenized medium. The root term is a correction factor that quantifies how the pore flow differs from an ideal Poiseuille flow as the frequency increases [73]. This relationship requires a set of poro-mechanical parameters, namely, the flow resistivity σ , the tortuosity α_∞ and the viscous characteristic length Λ . A detailed explanation of the physical meaning of each parameter and a review of the techniques to determine their value are given later in this section.

The elasticity coefficients \tilde{Q} and \tilde{R} include the thermal effects in the material. The coefficient \tilde{Q} can be interpreted as a measure of the coupling between the deformations of the two phases, whereas the coefficient \tilde{R} is the dynamic bulk modulus of the fluid phase occupying a fraction ϕ of the porous material. For most of the porous media employed in acoustic applications it is possible to assume that the bulk modulus of the material from which the solid phase is made is much larger than the bulk modulus of the filling fluid and than the bulk modulus of the skeleton in vacuo. Under this assumption, the expressions for \tilde{Q} and \tilde{R} can be simplified to [67]:

$$\tilde{Q} = (1 - \phi) \tilde{K}_f \quad (4.9)$$

$$\tilde{R} = \phi \tilde{K}_f \quad (4.10)$$

Both coefficients are related to the dynamic bulk modulus of the air in the pores \tilde{K}_f . This modulus accounts for the thermal dissipation between the two phases [73]. Again, a model is necessary to relate the thermal effects at the microscopic scale and the macroscopic dynamic bulk modulus. In this research we use the semi-phenomenological expression derived by Champoux and Allard [74]:

$$\tilde{K}_f = \frac{\zeta P_0}{\zeta - (\zeta - 1) \left[1 - j \frac{8\eta_0}{\Lambda^2 Pr \omega \rho_0} \sqrt{1 + j \frac{\Lambda^2 Pr \rho_0 \omega}{16\eta_0}} \right]^{-1}} \quad (4.11)$$

The properties of the filling fluid are given by the adiabatic index ζ , the static pressure P_0 and the Prandtl number Pr . The poro-mechanical parameter controlling the thermal exchanges is the thermal characteristic length Λ' . The selected Champoux-Allard model correctly predicts the dynamic bulk modulus of polyurethane foams, as the comparisons to measured data in [75] demonstrated.

Waves propagating inside a poroelastic material

From the poroelasticity equations it is possible to obtain the wave numbers of the bulk waves propagating inside the medium. The detailed derivation is included in many references, as for example in [67, 76]. Three different waves propagate inside a poroelastic material, in contrast to the single compressional wave found in fluid media, and the compressional and shear waves present in elastic solids.

The wave equations for the longitudinal waves are obtained after applying the divergence operator to Eq. (4.1) and (4.2) [77]. The resulting squared wave numbers k_1^2 and k_2^2 for the two compressional waves in a poroelastic material are given by:

$$k_{1/2}^2 = \frac{\omega^2}{2(\tilde{P}\tilde{R} - \tilde{Q}^2)} \left[\tilde{P}\tilde{\rho}_{22} + \tilde{R}\tilde{\rho}_{11} - 2\tilde{Q}\tilde{\rho}_{12} \pm \sqrt{\Delta} \right] \quad (4.12)$$

with

$$\Delta = \left[\tilde{P}\tilde{\rho}_{22} + \tilde{R}\tilde{\rho}_{11} - 2\tilde{Q}\tilde{\rho}_{12} \right]^2 - 4(\tilde{P}\tilde{R} - \tilde{Q}^2)(\tilde{\rho}_{11}\tilde{\rho}_{22} - \tilde{\rho}_{12}^2) \quad (4.13)$$

$$\tilde{P} = \frac{E(1-\nu)}{(1+\nu)(1-2\nu)} + \frac{(1-\phi)^2}{\phi} \tilde{K}_f \quad (4.14)$$

The longitudinal waves are not related to a specific phase and propagate simultaneously in both the fluid and the skeleton. In contrast, the shear wave is characteristic of the elastic solids and, therefore, only propagates in the frame. The shear wave equation is derived after applying the curl operator to Eq. (4.1) [77], and its associated squared wave number k_3^2 is:

$$k_3^2 = \frac{2\omega^2(1+\nu)}{E} \left(\frac{\tilde{\rho}_{11}\tilde{\rho}_{22} - \tilde{\rho}_{12}^2}{\tilde{\rho}_{22}} \right) \quad (4.15)$$

For each of the propagating waves the corresponding wavelength is obtained from the wave number as:

$$\lambda_i = \frac{2\pi}{\text{Re}(k_i)} \quad i = 1, 2, 3 \quad (4.16)$$

Dissipated power inside a poroelastic medium

A key factor to correctly capture the acoustic effectivity of a poroelastic treatment is the proper modeling of the dissipation mechanisms taking place. Losses are generally related to either the real or the imaginary part of the material coefficients. Below, the expressions for the dissipated power by the different mechanisms are indicated for the (\mathbf{u}, p) formulation. These relations were derived in [78]. The dissipated power can be divided into three classes: the structural damping W_{str} , the viscous losses W_{visc} and the thermal effects W_{th} . The viscous dissipated power is, in turn, the sum of viscous losses in the solid phase W_{visc}^s , in the fluid phase W_{visc}^f and due to the interaction between the two phases W_{visc}^{sf} . The total losses are obtained by integration over the poroelastic material domain Ω_p .

$$W_{str} = \pi \int_{\Omega_p} \text{Im}(\hat{\underline{\sigma}}^s(\hat{\mathbf{u}})) : \varepsilon(\hat{\mathbf{u}}^*) dV \quad (4.17)$$

$$W_{visc} = W_{visc}^s + W_{visc}^f + W_{visc}^{sf} \quad (4.18)$$

with

$$W_{visc}^s = -\pi\omega^2 \int_{\Omega_p} \text{Im}(\tilde{\rho}) |\hat{\mathbf{u}}|^2 dV \quad (4.19)$$

$$W_{visc}^f = \pi \int_{\Omega_p} \text{Im}\left(\frac{\phi^2}{\tilde{\rho}_{22}\omega^2}\right) |\nabla\hat{p}|^2 dV \quad (4.20)$$

$$W_{visc}^{sf} = -2\pi \int_{\Omega_p} \text{Im}\left(\frac{\phi}{\tilde{\alpha}}\right) \text{Re}(\hat{\mathbf{u}}^* \nabla\hat{p}) dV \quad (4.21)$$

$$W_{th} = \frac{\phi^2 \pi \text{Im}(\tilde{R})}{|\tilde{R}|^2} \int_{\Omega_p} |\hat{p}|^2 dV \quad (4.22)$$

The operators $\text{Re}()$ and $\text{Im}()$ refer to the real and imaginary part of a quantity, respectively. The superscript $*$ indicates the complex conjugate of a variable. The structural damping W_{str} is exclusively dependent on the elastic properties of the frame in vacuo, which are included in the stress tensor $\hat{\underline{\sigma}}^s(\hat{\mathbf{u}})$. Conversely, the thermal dissipation is only related to the fluid phase, whereas the viscous losses include contributions of both phases and their interactions. The relative contribution of each dissipation mechanism to the total losses inside the material is not exclusively a function of the material properties. Other external elements such as the excitation nature and the boundary and coupling conditions have an influence too. In Chapter 5 the effect of the coupling conditions together with the impact of the material parameters are addressed.

Simplifications of the poroelasticity equations

In case that one of the two phases dominates the material behavior, it is possible to derive two limiting states directly from the poroelasticity theory. If the contribution of the dissipation in the filling fluid is neglected, the two first terms of Eq. (4.1) describe the dynamic behavior of an elastic solid in vacuo, as shown in Eq. (4.23). The effective density $\tilde{\rho}$ should now be replaced by the bulk mass density of the solid phase $\rho_1 = (1 - \phi)\rho_s$. This simplified equation has the same form as the harmonic governing equation for an elastic solid given in Eq. (3.16). Therefore, in the following we refer to this model as *elastic*.

$$\nabla \cdot \hat{\underline{\sigma}}^s(\hat{\mathbf{u}}) + \omega^2 \rho_1 \hat{\mathbf{u}} = 0 \quad (4.23)$$

Analogously, it is possible to exclude the influence of the solid frame in two situations. First, we speak of a *rigid* model if the skeleton is assumed to be extremely rigid and motionless. The resulting expression in Eq. (4.24) is derived from the first two terms of Eq. (4.2). It represents the dynamic behavior of an acoustic fluid as in Eq. (3.5) but with a modified dynamic density $\tilde{\rho}_{eq} = \tilde{\rho}_{22}/\phi$ and a modified dynamic bulk modulus $\tilde{K}_{eq} = \tilde{R}/\phi$ [79]. These frequency-dependent density and bulk modulus allow the inclusion of the additional dissipation effects due to the porous nature of the material.

$$\nabla^2 \hat{p} + \frac{\tilde{\rho}_{eq}}{\tilde{K}_{eq}} \omega^2 \hat{p} = 0 \quad (4.24)$$

Second, when the skeleton is extremely soft or *limp*, the elastic forces in the solid phase are negligible against the inertial and pressure forces, and the frame moves together with the fluid phase without increasing the stress stiffness of the system. In this case, the presence of the solid phase only contributes to the inertial term, that is, only the mass of the frame is considered. As a result, the dynamic density of the equivalent fluid for the rigid case $\tilde{\rho}_{eq}$ is replaced by $\tilde{\rho}_{limp}$ in Eq. (4.25), which includes the inertial effects introduced by the solid frame [80].

$$\tilde{\rho}_{limp} = \frac{\tilde{\rho}_{eq}(\rho_1 + \phi\rho_0) - \rho_0^2}{\rho_1 + \phi\rho_0 + \tilde{\rho}_{eq} - 2\rho_0} \quad (4.25)$$

In the current analysis the limp formulation is employed because it is better suited for applications where the porous material is mounted on a vibrating structure, as indicated in [81]. For consistency purposes, in the following sections we identify the limp model as *porous*.

Characterization of the poroelastic parameters

The material parameters present in the poroelastic model introduced above can be classified into three groups:

- Fluid properties: fluid density ρ_0 , dynamic viscosity η_0 , adiabatic index ζ , Prandtl number Pr .
- Elastic properties: Young's modulus E , solid density ρ_s , Poisson's ratio ν , damping coefficient η .
- Poro-mechanical properties: porosity ϕ , flow resistivity σ , tortuosity α_∞ , viscous characteristic length Λ , thermal characteristic length Λ' .

Assuming that the properties of the filling fluid are known and remain constant at room temperature, there are nine parameters left that need to be determined. In the next paragraphs we describe some of the experimental methods available for the characterization of poroelastic media, including the ones employed in this research.

Elastic properties

The mass density of a poroelastic material can be expressed in different forms. In the previous sections we have introduced the mass density ρ_s of the material from which the solid frame is made of and the density ρ_1 of the frame in vacuo. They are both related by the fraction of solid volume $(1 - \phi)$:

$$\rho_1 = (1 - \phi) \rho_s \quad (4.26)$$

Moreover, the total density of the porous aggregate ρ_T is obtained by adding the mass density of the fluid fraction $\rho_T = \rho_1 + \phi\rho_0$. As it can be noticed, the determination of the density is strongly linked to the definition of the porosity. Salissou and Panneton [82] developed a procedure to obtain both parameters simultaneously. This non-acoustical method is based on the measurement of the mass and the pressure of a sealed container filled with a gas. First, the tank is measured at one low pressure and one high pressure state. After that, the poroelastic sample is placed inside the container and the measurements at the two pressure states are repeated. From the difference of the masses combined with the perfect gas law the values for the porosity ϕ and for the mass density ρ_1 of the frame in vacuo are calculated. This procedure is very stable and has good reproducibility.

The determination of the other elastic properties is more challenging and numerous techniques are available. The skeleton of polymeric poroelastic materials, like the polyurethane foams commonly applied as acoustic treatments in the automotive industry, have a viscoelastic behavior. This means that under deformation the material exhibits viscous as well as elastic characteristics [83]. For the typical deformation amplitudes that noise control treatments undergo, the behavior remains in the linear viscoelasticity regime. Additionally, in the present study we have assumed that the materials are isotropic. A schematic force-displacement diagram for a viscoelastic material has been represented in Figure 4.3. Unlike elastic materials, the loading and unloading paths for a cyclic force are not the same. The area enclosed between the two curves is called the hysteresis loop and corresponds to the energy dissipated per cycle inside the material because of the viscoelastic losses.

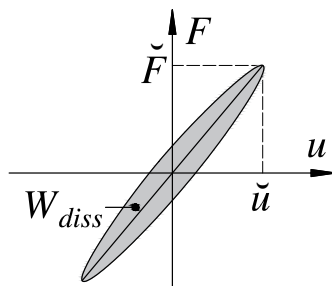


Figure 4.3: Force-displacement curve for a linear viscoelastic material under oscillatory loading (adapted from [83]).

In order to include the skeleton dissipation in the poroelastic equations we make use of complex expressions for the elasticity and shear moduli as indicated in Eq. (4.27). The loss factor η expresses the ratio between the real and imaginary parts. All quantities can be frequency-dependent, as it will be stated later in this section.

$$\begin{aligned}\tilde{E}(\omega) &= E_r(\omega) + jE_i(\omega) = E_r(\omega) [1 + j\eta(\omega)] \\ \tilde{G}(\omega) &= G_r(\omega) + jG_i(\omega) = G_r(\omega) [1 + j\eta(\omega)]\end{aligned}\quad (4.27)$$

The methods for the characterization of the elastic parameters can be classified in three groups [84]. First, there are approaches based on the velocity at which waves propagate inside the poroelastic material. For instance, the velocity of the Rayleigh waves can be related to the shear modulus G and the Poisson's ratio ν of the material [85, 86]. A layer of poroelastic material is fixed to a rigid plate on one of its ends. On the other end, the layer is excited with a harmonic signal through a shaker. A laser vibrometer is employed to measure the displacement on the surface. The Fourier transform of the signal permits to identify the wave number k of the modes, which is linked to the phase velocity v as $v = \omega/k$. The fitting of the theoretical and the measured phase velocities delivers frequency-dependent values for G and ν . The poro-mechanical parameters need to be previously measured by other means to calculate the theoretical solution.

Second, the shear modulus and the Poisson's coefficient can also be calculated with the help of acoustic methods. A material sample with rigid backing is excited by a monopole source. A microphone located near the sample measures the pressure resulting from the direct and the reflected fields. After that, the poroelastic material is replaced by a rigid, impervious surface and the procedure is repeated. The ratio between the two pressures

is then built. Again, out of the contrast between the obtained values and the theoretical solution, provided that the poro-mechanical parameters are known, the elastic parameters can be derived [87].

The third group is formed by the vibrational methods, which are based on the response of the material subjected to a mechanical excitation. The vibrational approaches are further broken down into two categories: the quasi-static methods, in which the inertial effects are neglected, and the dynamic techniques, which include them. An example of the former class is the quasi-static uniaxial compression. A schematic representation of the experimental setup is depicted in Figure 4.4 (left). The poroelastic sample is placed between two rigid plates. One plate is rigidly connected to a fixed wall through a force transducer that measures the reaction force. The other plate is excited by a shaker, and the resulting acceleration is measured by an accelerometer attached to this plate. The shaker employs a random excitation in a frequency range under the first resonance of the sample. The compression stiffness and the loss factor are calculated from the modulus and the phase of the force-displacement transfer function, respectively. In the approach proposed by [88] two material samples of different shape factor are measured. The shape factor is defined as the ratio of half the radius to the thickness of the sample. After that, several Finite Element simulations on elastic solids under compression are run to obtain polynomial relations that link the measured compression stiffness to the elasticity modulus, the Poisson's ratio and the shape factor.

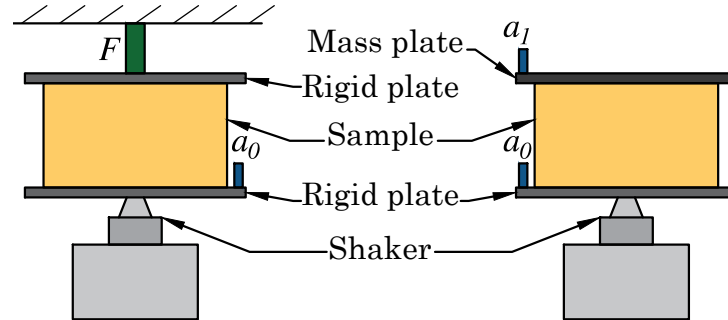


Figure 4.4: Experimental setup for the uniaxial compression loading: (left) rigid backing for the quasi-static compression method, (right) spring-mass configuration for the dynamic resonance approach. F is a force transducer, a indicates the position of the acceleration sensors. Note that the components are not scaled.

In order to account for the inertial effects, this setup can be modified to conduct a dynamic uniaxial compression, like the configuration presented by Pritz [89, 90]. The adapted measurement setup is displayed in Figure 4.4 (right). The fixed plate is replaced by a rigid mass with known weight. The maximum frequency of the shaker excitation is increased, so that the first resonance of the system f_r can be captured. From the frequency f_r together with the geometrical properties of the sample, the real part of the Young's modulus can be calculated as specified by Eq. (4.28). The mass m_T is the sum of the weight of the poroelastic sample and the upper mass, h is the thickness of the foam sample and A its transversal area. The damping factor η is obtained from the 3 dB bandwidth of the resonance Δf as Eq. (4.29) defines.

$$E_r = (2\pi f_r)^2 \frac{m_T h}{A} \quad (4.28)$$

$$\eta = \frac{\Delta f}{f_r} \quad (4.29)$$

A review of other quasi-static and dynamic experimental methods, including torsion and shear loadings too, can be found in [84] and [91]. In the scope of this research six different poroelastic foams were analyzed. The elastic properties employed for the investigations in the next chapters are presented in Table 4.1. Those values correspond to the average of the measurements on at least three foam samples of the same material. The method applied for the determination is indicated in each property. It can be noticed that the values of the elasticity modulus obtained with the compression method [88] are systematically lower than the ones provided by the resonance method [89] since the former neglects the inertial effects. As the frequency increases, the inertial force increases with respect to the elastic force in the system [92] and the utilization of dynamic characterization techniques becomes necessary.

Parameter	E		ρ_1	η		ν	h
Units	Pa		kg m^{-3}	-		-	mm
Method	[88]	[89]	[82]	[88]	[89]	[88]	-
Sample A	43440		64.83	30.5%		0.452	10.8
Sample B	139050	174330	54.87	37.5%	53.0%	0.357	15.8
Sample C	33690		67.83	11.4%		0.397	25.3
Sample D	15900	23670	73.10	17.4%	19.3%	0.346	13.2
Sample E	15000	18330	68.80	14.8%	17.7%	0.363	21.9
Sample F	109800		27.40	8.0%		0.411	25.9

Table 4.1: Elastic foam parameters measured by different characterization approaches.

Poro-mechanical properties

The airflow resistivity σ is a measure of the material resistance to an airflow and is related to the viscous losses. Its value can be obtained as indicated in the Standard ISO 9053 [93]. The test sample is placed in a so-called static airflow resistance meter, where a quasi-static flow Q is forced through the material and the required pressure drop Δp is measured, as indicated in Figure 4.5. The specific flow resistivity is calculated with the expression in Eq. (4.30), where h is the thickness of the sample. The use of this methodology for the determination of σ is wide extended. The values for typical poroelastic materials range between 1000 and 1000000 N s m^{-4} .

$$\sigma = \frac{\Delta p}{Q \cdot h} \quad (4.30)$$

The tortuosity α_∞ is a non-dimensional parameter defined as the average fluid path length through the material normalized by the thickness of the material and accounts for the apparent increase in the fluid density when the fluid saturates a porous structure. It usually takes values between 1 and 3. The viscous characteristic length Λ is an average of the radius of the smaller pores, where the viscous losses dominate over the thermal losses. Conversely, the thermal characteristic length Λ' is an average of radius of the larger pores,

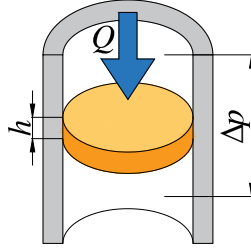


Figure 4.5: Schematic representation of the flow resistivity meter.

where the thermal losses dominate over the viscous losses. Both characteristic lengths have values in the range between 10 and 1000 μm , and the length Λ' is always larger than Λ . Regarding the determination of these three poro-mechanical properties we face the issue that no standards are available [94]. The methods employed for their characterization can be divided into two groups: direct and inverse methods. A direct procedure to obtain the tortuosity is described in [95]. At high frequencies, the viscous losses become negligible. Consequently, the phase velocity of the air wave propagating in the sample is only dependent on the inertial effects, that is, on the effective density of the air in the pores, which is proportional to the tortuosity (recall Eq. (4.8)). From the high-frequency asymptotic value of the phase velocity is possible to determine the tortuosity. The viscous and thermal characteristic lengths can be directly extracted from ultrasonic measurements as explained by Leclaire *et al.* [96, 97]. The method is based on the high frequency limit of the velocity and attenuation curves with two different filling fluids, namely air and helium.

The main drawback of the direct methods is the requirement of complex, specific laboratory instruments like ultrasonic and vacuum equipment. Alternatively, the inverse procedures like the ones reported in [72, 75, 98, 99] combine simpler measurement techniques and analytical models. The approaches in [98, 99] are based on measured values of the specific normal impedance of a material probe in an impedance tube. A differential evolution algorithm is applied to simultaneously find the material tortuosity and the two characteristic lengths that minimize the difference between the measured value and the estimated one. For this estimation, the Johnson-Champoux-Allard model is commonly used (Eq. (4.8) and (4.11)). Panneton and Olny [72, 75] also make use of impedance measurements. From the resulting dynamic density it is possible to calculate the viscous characteristic length and the tortuosity with the help of analytical expressions. Analogously, the measured dynamic bulk modulus is utilized to derive the value of the thermal characteristic length. The major advantage of the inverse approaches lies in the fact that they use experimental data obtained in an impedance or Kundt's tube, which is a measurement equipment of wide application in acoustic laboratories.

The results of the material characterization obtained for the investigated samples are summarized in Table 4.2 for the poro-mechanical parameters. The characterization measurements were conducted by the company Mecanum [100] with only one method for each parameter, except for the tortuosity. The parameter α_∞ was determined with a direct and an inverse technique, but both approaches delivered comparable results and only the values for the direct approach are included here.

A critical issue in the characterization of poroelastic media arises from the lack of reproducibility. On the one hand, the tested samples often include inhomogeneities or imperfections as a result of the manufacture processes, as illustrated in Figure 4.6. On

Parameter	ϕ	σ	α_∞	Λ	Λ'
Units	-	N s m^{-4}	-	μm	μm
Method	[82]	[93]	[95]	[98]	[98]
Sample A	0.950	30210	2.579	44	154
Sample B	0.954	18664	1.440	42	250
Sample C	0.932	18630	1.526	67	165
Sample D	0.921	15450	1.660	86	163
Sample E	0.921	14640	1.440	85	154
Sample F	0.955	3400	1.310	121	386
Sample S	-	18669	1.910	69	197

Table 4.2: Poro-mechanical foam parameters measured by different characterization approaches.



Figure 4.6: Examples of non-uniformly distributed random size bubbles inside the foam samples resulting from the manufacturing process.

the other hand, the measurement equipment and techniques applied suffer from reproducibility issues, as highlighted in [101, 102]. Therefore, we have additionally defined a standard set of the poro-mechanical parameters, with exception of the porosity ϕ , that is calculated from the average of the measured properties from the foam samples A to F. These parameters as indicated in Table 4.2 as Sample S. The porosity has been excluded since its characterization procedure is stable and it has a small variation range for most acoustical materials [103]. The influence of the variations or inaccuracies in the material parameters is assessed later in Chapter 5.

All the methodologies presented above are based on the macroscopic behavior of the materials. Another option is to derive the poro-mechanical parameters from the microstructure of the material. The approaches presented by Zieliński [104] and by Perrot *et al.* [105] are founded upon the behavior of the visco-thermal dissipation at the low and high frequency limits. In these regimes it is possible to simplify the dissipation into boundary-value problems that are solved in a representative unit cell. The main hypothesis is that the acoustic wavelength is much larger than the size of the cell. Out of the geometry of the representative unit cell, which can be obtained with the help of X-ray computed tomographic images [105], one can determine ϕ and Λ' . The porosity ϕ is, by definition, the ratio of free fluid volume to the total material volume, whereas the thermal character-

istic length Λ' is twice the ratio of the volume of fluid domain Ω_f to the surface of the solid-fluid interface $\partial\Omega_{sf}$ [104]:

$$\Lambda' = 2 \frac{\int_{\Omega_f} dV}{\int_{\partial\Omega_{sf}} dS} \quad (4.31)$$

At low frequencies, the viscous forces predominate over the inertial forces and the fluid movement inside the pores is simplified to a Stokes flow. The linear relation between the exciting gradient of pressure and the resulting velocity field is the tensor field of viscous static permeability \underline{k} . For isotropic media, the scalar permeability k_0 is calculated as the average of the permeability tensor over the fluid domain and scaled by the porosity $k_0 = \phi \langle \underline{k} \rangle_f$, where $\langle \rangle_f$ indicates the average in the fluid domain. This quantity can be linked to the flow resistivity by:

$$\sigma = \frac{\eta_0}{k_0} \quad (4.32)$$

In the high frequency range, the inertial effects dominate over and the viscous ones. The fluid flow can be then represented as an electrical problem in which the insulating solid phase is filled with a conductive fluid and a constant electric field is applied. The result of this equivalent problem is the electric field \mathbf{E} . For an isotropic material the tortuosity is given by:

$$\alpha_\infty = \frac{\langle \mathbf{E} \cdot \mathbf{E} \rangle_f}{\langle \mathbf{E} \rangle_f \cdot \langle \mathbf{E} \rangle_f} \quad (4.33)$$

The viscous characteristic length is calculated from:

$$\Lambda = \frac{\int_{\Omega_f} \mathbf{E} \cdot \mathbf{E} dV}{\int_{\partial\Omega_{sf}} \mathbf{E} \cdot \mathbf{E} dS} \quad (4.34)$$

Determination of frequency-dependent elastic properties

As introduced in the previous subsection on the elastic parameters, the dynamic behavior of the solid frame is viscoelastic and frequency-dependent. In [69] and [106] two examples are given on the modeling of a poroelastic layer that covers a structurally excited plate. In both cases the foam layer was described using the full poroelastic formulation. It was first found that the application of the quasi-static elastic parameters resulted in a poor comparability with the experimental data. In a second step, a frequency-dependent profile for the elastic properties was defined by fitting the calculated predictions to the reference data sets. Even if this derivation leads to a good prediction of the vibroacoustic behavior, it presents the great disadvantage that a measurement of the complete setup is needed in order to obtain the frequency-dependent parameters.

An alternative to the complex poroelastic modeling is, as mentioned before, the simplification of the material as an elastic solid. This approach has the major advantage of avoiding the characterization of the pro-mechanical properties, which is a laborious task and requires specific test equipment. However, since the presence of the fluid phase is neglected, some dissipation mechanisms inside the poroelastic medium may not be correctly represented, especially at high frequencies. An option to include the missing mechanisms is to condense the additional effects by means of frequency-dependent elastic parameters.

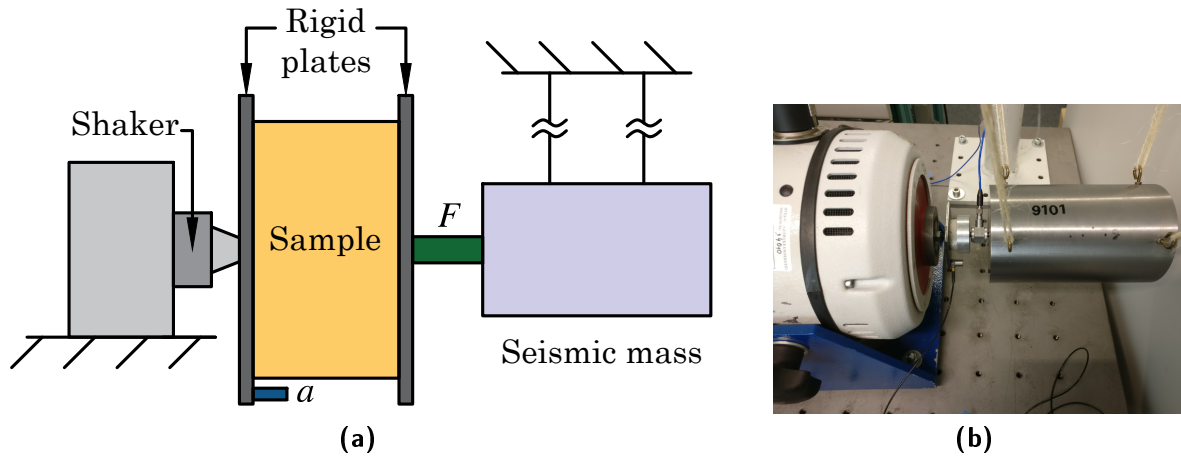


Figure 4.7: Experimental setup with seismic mass employed for the determination of frequency-dependent elastic properties: (a) schematic representation, F is the force transducer and a indicates the position of the acceleration sensor (note that the components are not scaled), (b) measurement device in operation.

Just few references are available in the literature on the frequency-dependent characterization of poroelastic materials, which is conducted analogously to that of classic viscoelastic media [107, 108]. One general trend that can be identified is that the real part of the Young's modulus E_r increases with frequency. This is a common progression for polymers and other viscoelastic materials, which do not have a cristaline structure [109, 110]. Since the frame of investigated polyurethane foams is also a viscoelastic material, such a frequency behavior is to be expected. Duvigneau *et al.* [111, 112] proposed a dynamic characterization procedure to determine the frequency-dependent elastic properties of foam materials. In this approach, the sample is assumed to behave like a single degree of freedom spring-mass-damper system whose stiffness and damping coefficients need to be obtained.

During the characterization measurement the material sample is placed between two plates, which are supposed to be rigid. The cylindrical test specimen has a thickness h and a cross-sectional area A . One of the plates is excited by a shaker that provides a harmonic excitation. A discrete number of frequencies within the frequency band of interest is selected and sequentially tested. The mechanical response of the foam is acquired with the help of an acceleration sensor located on the excitation plate. The other plate is rigidly connected to a termination through a force transducer that measures the force applied on the sample. Two different terminations have been investigated, namely a seismic mass suspended from the ceiling (Figure 4.7) and a rigid block (Figure 4.8). Both terminations have a very large mass and work as a fixed clamping. The main advantage of the seismic mass is that, thanks to the free-free mounting conditions, the eigenresonances only appear at frequencies close to zero hertz. For the metal block, conversely, other resonances occur around 1 kHz, which can affect the results in the frequency range of interest. However, the suspended mass presents other difficulties like the determination of the zero position for the uncompressed sample. The results obtained with the two terminations are comparable and show good reproducibility. Because of the simpler setting, the configuration with the rigid block is the preferred solution.

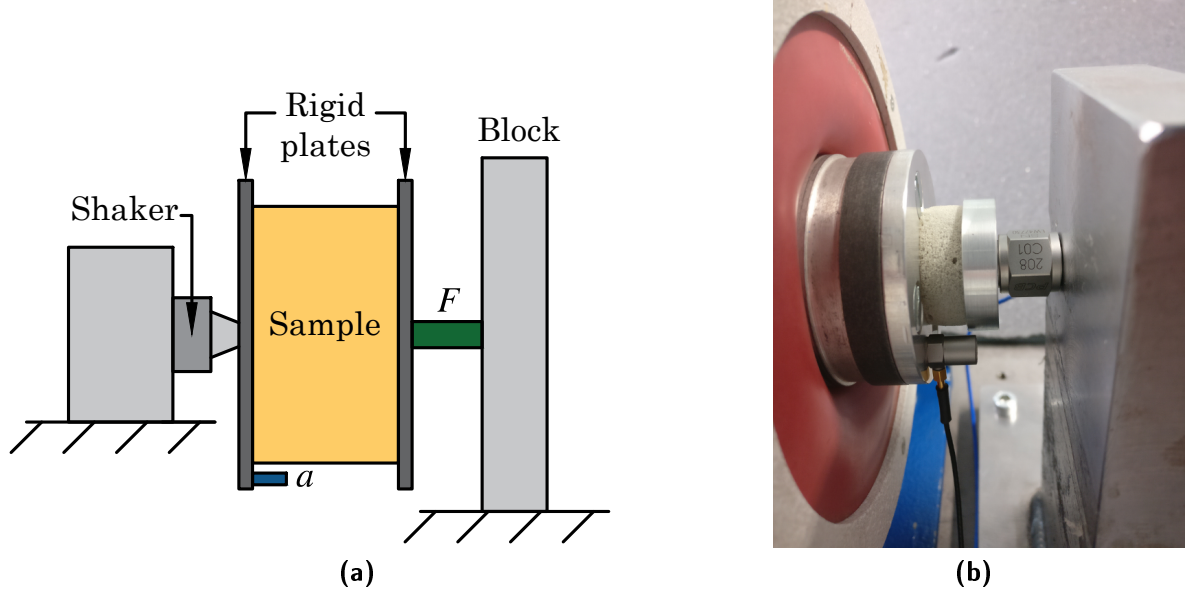


Figure 4.8: Experimental setup with rigid block employed for the determination of frequency-dependent elastic properties: (a) schematic representation, F is the force transducer and a indicates the position of the acceleration sensor (note that the components are not scaled), (b) measurement device in operation.

During the experiment, the force and acceleration are recorded for different frequencies. Since the excitation is harmonic, the resulting displacement $u = |u| \exp(j\omega t)$ is directly linked to the measured acceleration $a = d^2u/dt^2$ by:

$$u = \frac{a}{(j\omega)^2} \quad (4.35)$$

The measured data are then evaluated at each frequency of interest. The stiffness constant c of the one-dimensional spring-mass-damper system is:

$$c = \frac{\check{F}}{\check{u}} \quad (4.36)$$

being \check{F} the maximum force and \check{u} the maximum displacement in the force-displacement curve (recall Figure 4.3). The damping coefficient d is given by:

$$d = \frac{W_{diss}}{\check{u}^2 2\pi^2 f} \quad (4.37)$$

where the total hysteresis loss W_{diss} corresponds to the area enclosed in a loading and unloading cycle:

$$W_{diss} = \oint F du \quad (4.38)$$

The real and imaginary part of the elasticity coefficients are lastly obtained with the help of the geometrical dimensions of the sample from the relations in Eq. (4.39) and (4.40).

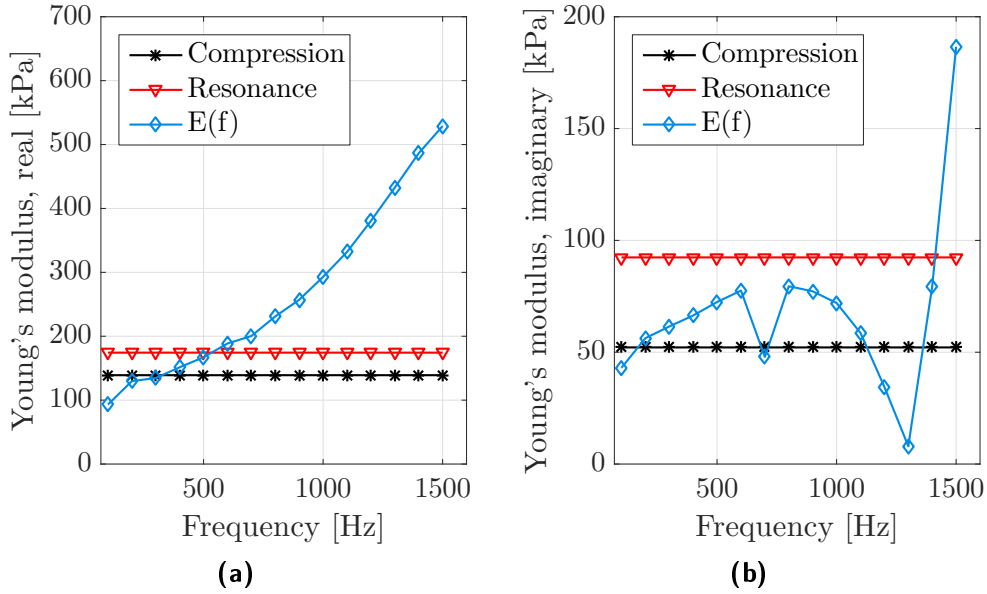


Figure 4.9: Comparison of the Young's modulus obtained with different characterization techniques for the foam sample B: (a) real part, (b) imaginary part.

$$E_r = c \frac{h}{A} \quad (4.39)$$

$$E_i = \frac{W_{diss}}{\check{u}^2 \pi} \frac{h}{A} \quad (4.40)$$

The calculated frequency-dependent parameters can be applied either in combination with the full poroelastic model or in the simplified elastic formulation. In Figure 4.9 the results of the presented characterization method $E(f)$ are contrasted to those of the compression [88] and resonance techniques [89] for the foam sample B. The obtained values are consistent with the expected progression for the real part of the elasticity modulus. The irregularities in curve for the imaginary part may be attributed to some inaccuracies in the determination of the dissipated power W_{diss} . The measured data may be smoothed out by a curve approximation, either with a linear interpolation or with any other material model. For instance, in [106] the material behavior was described according to the damping formulation of the augmented Hooke's law.

4.2 Numerical methods for poroelastic media

The numerical description of poroelastic media requires the resolution of the complex, frequency-dependent poroelasticity equations in Eq. (4.1) and (4.2), which implies cumbersome calculations. Techniques based on the discretization of the spatial domain are widely spread, among which the Finite Element Method is the most commonly used. Alternatively, the semi-analytical methods constitute a compromise between accuracy and speed, but they are only appropriate under certain conditions [113]. The next paragraphs summarize the underlying assumptions of each methodology and their application scope. The second part of this section focuses on the implementation of the FEM for poroelastic media, including a convergence analysis.

Semi-analytical techniques for poroelastic media

The main advantage of the semi-analytical methods is that they avoid the resolution of the three-dimensional coupled partial equations of the Biot-Allard theory, thus saving up computational resources. The behavior of the poroelastic material is reduced to its behavior in the thickness direction, in other words, the material is locally reacting. Consequently, the interactions along the in-plane directions are neglected.

If a poroelastic component is directly coupled to an acoustic fluid, the simplest semi-analytical technique to include it is the impedance boundary condition. The material on the surface of the fluid is only characterized by its normal impedance \tilde{Z}_n [114], which relates the pressure perturbation to the velocity normal to the surface (recall Eq. (3.2)). Its value can either be obtained by direct measurement in an impedance tube [115], or out of the modified dynamic density $\tilde{\rho}_{eq}$ and dynamic bulk modulus \tilde{K}_{eq} that define the porous simplification with the relation in Eq. (4.41) [116]. Since only acoustic fluids can include an impedance boundary condition, this approach can be convenient for evaluating the absorptive effect of a poroelastic material applied on the walls of a fluid cavity, as shown later in Section 7.2. Nevertheless, it is unsuited for sound transmission problems.

$$\tilde{Z}_n = \left(\frac{\tilde{\rho}_{eq}}{\tilde{K}_{eq}} \right)^{1/2} \quad (4.41)$$

In that case, the wave propagation through a poroelastic medium can be modeled in terms of a square transfer matrix. The transfer matrices relate the stresses and velocities at each side of a material layer, but also neglect the in-plane effects [67]. Flat components with constant thickness and infinite lateral dimensions are assumed. This description enables to model all kinds of materials, including poroelastic, porous, fluid and elastic media. The matrices of different components can easily be coupled to each other in order to evaluate the performance of multi-layered systems, which is the basis of the Transfer Matrix Method [117]. The size of the transfer matrix and the evaluation of the matrix coefficients depend on the number and nature of the waves propagating inside the material. For the description of a layer of poroelastic material it is also possible to combine the transfer matrix with a Finite Element model like shown in [118]. For instance, the transfer matrix can be applied as coupling condition at the interface between a vibrating structure and a fluid on which the acoustic treatment is placed.

Such simple approaches can give a good first estimation of the behavior of a sound package and allow a qualitative comparison of different noise treatments, always in consideration of the underlying assumptions. Some corrections have been proposed to include finite size effects, curved panels or non-isotropic behaviors [67, 119]. Nevertheless, the application of the semi-analytical methods is usually restricted to the high frequency range, since they fail to represent the three-dimensional in-plane interactions.

Discretization techniques for poroelastic media: The Finite Element Method

The approaches based on the spatial discretization of the poroelastic domain are the same techniques as those available for the conventional vibroacoustic problems. Tanneau *et al.* [120] developed a bi-dimensional Boundary Element formulation to represent the impact of a porous layer on a vibrating structure. Even if less elements than for a FE model are needed, the fully populated system of matrix equations that is obtained

decreases the computational efficiency of the BEM. The Wave Based Method has also been employed for describing poroelastic media, as explained in [121]. This approach results in relatively small number of equations to be solved, which has a high potential in reducing the total computational effort. However, its application is nowadays limited to convex, two-dimensional domains and only implemented in the in-house codes of the developing research institutions.

In contrast, the calculation by means of Finite Element analysis is extended for three-dimensional problems and can currently be found in many commercial solvers. The main advantage of the method is that there are no geometrical restrictions.

The early attempts to include poroelastic media in FE simulations exclusively considered the porous simplification with rigid frame. An example is the Finite Element for rigid absorbing materials developed by Craggs [122]. The weak formulation for the coupled poroelastic equations was first derived in the 1990s for the original displacement formulation, whereas Atalla *et al.* [68] presented the first derivation for the mixed pressure-displacement formulation. In the present research we make use of the latter because it means a reduction in the number of unknowns per node from six to four. A comprehensive review of the historical development of the FEM for poroelastic materials can be found in [123].

The initial weak variational formulation in the mixed formulation was later reviewed in order to facilitate the Finite Element implementation [124]. The resulting weak integral formulation reads:

$$\begin{aligned} \mathcal{W}(\hat{\mathbf{u}}, \delta\hat{\mathbf{u}}, \hat{p}, \delta\hat{p}) &= \int_{\Omega_p} \hat{\underline{\sigma}}^s(\hat{\mathbf{u}}) : \hat{\underline{\varepsilon}}^s(\delta\hat{\mathbf{u}}) \, dV - \omega^2 \int_{\Omega_p} \tilde{\rho}\hat{\mathbf{u}} \cdot \delta\hat{\mathbf{u}} \, dV - \int_{\Omega_p} \frac{\phi}{\tilde{\alpha}} \delta(\nabla \hat{p} \cdot \hat{\mathbf{u}}) \, dV \\ &+ \int_{\Omega_p} \left(\frac{\phi^2}{\omega^2 \tilde{\rho}_{22}} \nabla \hat{p} \cdot \nabla \delta\hat{p} - \frac{\phi^2}{\tilde{R}} \hat{p} \delta\hat{p} \right) \, dV - \int_{\Omega_p} \phi \left(1 + \frac{\tilde{Q}}{\tilde{R}} \right) \delta(\hat{p} \nabla \cdot \hat{\mathbf{u}}) \, dV \\ &- \int_{\partial\Omega_p} (\hat{\underline{\sigma}}^t \cdot \mathbf{n}) \delta\hat{\mathbf{u}} \, dS - \int_{\partial\Omega_p} \phi (\hat{\mathbf{U}} \cdot \mathbf{n} - \hat{\mathbf{u}} \cdot \mathbf{n}) \delta\hat{p} \, dS = 0 \end{aligned} \quad (4.42)$$

On the boundaries of the poroelastic domain $\partial\Omega_p$ two variables have been introduced for simplification of the expressions. The total stress tensor $\hat{\underline{\sigma}}^t(\hat{\mathbf{u}}, \hat{p})$ of the material is defined by the relation in Eq. (4.43), with \underline{I} indicating the identity matrix. The vector $\hat{\mathbf{U}}$ represents the displacements in the fluid phase and can be calculated from the displacements in the solid phase and the acoustic pressure as indicated in Eq. (4.44).

$$\hat{\underline{\sigma}}^t(\hat{\mathbf{u}}, \hat{p}) = \hat{\underline{\sigma}}^s(\hat{\mathbf{u}}) - \phi \hat{p} \underline{I} \quad (4.43)$$

$$\hat{\mathbf{U}}(\hat{\mathbf{u}}, \hat{p}) = \frac{\phi}{\tilde{\rho}_{22}\omega^2} \nabla \hat{p} - \frac{\tilde{\rho}_{12}}{\tilde{\rho}_{22}} \hat{\mathbf{u}} \quad (4.44)$$

After the discretization of the integrals present in the variational formulation and the assembling of the element matrices, one obtains the following global system:

$$\begin{bmatrix} [\tilde{K}] - \omega^2[\tilde{M}] & -[\tilde{C}] \\ [\tilde{C}]^T & \frac{1}{\omega^2}[\tilde{H}] - [\tilde{Q}] \end{bmatrix} \begin{Bmatrix} \{\hat{\mathbf{u}}\} \\ \{\hat{p}\} \end{Bmatrix} = \begin{Bmatrix} \{\hat{F}\} \\ \{\hat{Q}\} \end{Bmatrix} \quad (4.45)$$

The nodal variables are the displacements in the solid phase $\{\hat{u}\}$ and the acoustic pressure $\{\hat{p}\}$. This system has the same form as the matrix for a fluid-structure coupled problem (refer to Eq. (3.23)), but there is a difference in the spatial definition of the nodal variables. In a fluid-structure problem the nodal pressures are defined in the fluid domain and nodal displacements describe the state of the structural domain. Because of the homogenization assumption, however, in a poroelastic medium both variable sets are defined simultaneously at every point of the domain.

The global matrices $[\tilde{K}]$ and $[\tilde{M}]$ are the equivalent mass and stiffness matrices of the skeleton. The matrices $[\tilde{H}]$ and $[\tilde{Q}]$ are the equivalent kinetic and compression energy matrices for the fluid phase, respectively. The volume coupling between the two phases is expressed in the global matrix $[\tilde{C}]$. As the tilde symbol indicates, the matrices associated to a poroelastic medium are frequency-dependent since they are functions of the coefficients $\tilde{\rho}$, $\tilde{\alpha}$ and \tilde{R} . This entails that the system matrices need to be calculated at each frequency. Furthermore, the non-linearity of the associated eigenvalue problem in the frequency hinders the application of standard modal techniques [125].

Coupling conditions

As already mentioned throughout this chapter, the main advantages of the mixed (\mathbf{u}, p) formulation are the reduction of the number of variables from six to four unknowns per node, and the straightforward coupling of the poroelastic domains to other media. When solving a general vibroacoustic problem including poroelastic components, as shown in Figure 4.10, each subdomain is governed by the partial differential equations of the medium together with the corresponding set of boundary conditions. At the interfaces between two domains the coupling conditions must satisfy the continuity relationships of the field variables.

At the coupling surface between a poroelastic and a fluid domain $\partial\Omega_{pf}$ the two first relations in Eq. (4.46) ensure the continuity of the normal stresses for the solid and the fluid phases, respectively. The third equation guarantees the continuity of the displacements normal to the interface.

$$\begin{aligned} \hat{\underline{\sigma}}^t(\hat{\mathbf{u}}, \hat{p}) \cdot \mathbf{n} &= -\hat{p}_f \cdot \mathbf{n} \\ \hat{p} &= \hat{p}_f \\ (1 - \phi) \hat{\mathbf{u}} \cdot \mathbf{n} + \phi \hat{\mathbf{U}} \cdot \mathbf{n} &= \frac{1}{\rho_0 \omega^2} \frac{\partial \hat{p}_f}{\partial n} \end{aligned} \quad (4.46)$$

Eq. (4.47) shows the continuity conditions at an interface between a poroelastic and an elastic medium $\partial\Omega_{ps}$. The first equation refers to the continuity of the normal stresses, the second sets the fluid flux across the interface to zero, and the third relation ensures the continuity of the displacements in the solid phase of the poroelastic material and the elastic medium.

$$\begin{aligned} \hat{\underline{\sigma}}^t(\hat{\mathbf{u}}, \hat{p}) \cdot \mathbf{n} &= \hat{\underline{\sigma}}_s(\hat{\mathbf{u}}_s) \cdot \mathbf{n} \\ \hat{\mathbf{U}} \cdot \mathbf{n} &= \hat{\mathbf{u}} \cdot \mathbf{n} \\ \hat{\mathbf{u}} &= \hat{\mathbf{u}}_s \end{aligned} \quad (4.47)$$

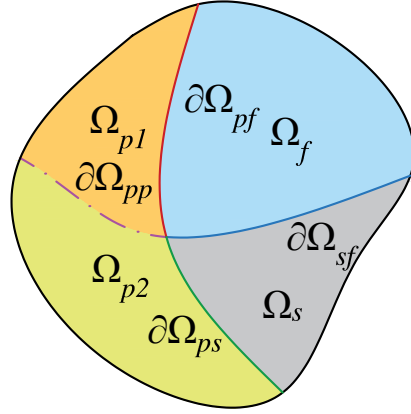


Figure 4.10: Schematic representation of a vibroacoustic domain including poroelastic media (adapted from [67]).

If two poroelastic media 1 and 2 are coupled, it must be satisfied at their interface $\partial\Omega_{pp}$ that the normal stresses, the normal fluid flux, the solid phase displacements and the pressure are continuous, as Eq. (4.48) indicates.

$$\begin{aligned}
 \hat{\underline{\sigma}}_1^t(\hat{\mathbf{u}}_1, \hat{p}_1) \cdot \mathbf{n} &= \hat{\underline{\sigma}}_2^t(\hat{\mathbf{u}}_2, \hat{p}_2) \cdot \mathbf{n} \\
 \phi_1(\hat{\mathbf{U}}_1 \cdot \mathbf{n} - \hat{\mathbf{u}}_1 \cdot \mathbf{n}) &= \phi_2(\hat{\mathbf{U}}_2 \cdot \mathbf{n} - \hat{\mathbf{u}}_2 \cdot \mathbf{n}) \\
 \hat{\mathbf{u}}_1 &= \hat{\mathbf{u}}_2 \\
 \hat{p}_1 &= \hat{p}_2
 \end{aligned} \tag{4.48}$$

From the above continuity relations, only the kinematic relations need to be explicitly imposed in the assembling step of the FE implementation [124]. All other coupling conditions are automatically taken into account in the weak integral formulations.

Accuracy and efficiency considerations

Inside a poroelastic medium three different bulk waves propagate, namely, two compressional waves and one shear wave, as indicated in the section before. Especially for materials with a low frame stiffness, the shear wavelength is very short. At the interfaces between a poroelastic domain and other media different surface waves can be identified. Feng and Johnson [126] found three surface waves and named them pseudo-Rayleigh, pseudo-Stoneley and true Stoneley waves by analogy with the surface waves propagating in classical fluid and solid domains. As the frequency of interest increases, the wavelengths become shorter and a high number of elements are necessary to ensure the convergence of the results. This increasing number of degrees of freedom represents one of the major drawbacks of the Finite Element approach in the middle and high frequency analysis [127]. In the literature there are diverse attempts to enhance the efficiency of the Finite Element implementation in applications including poroelastic domains. One option may be the decomposition of the problem into subsystems that are separately solved and then merged, thus reducing the size of the partial problems to be calculated. For instance, with the substructuring Patch Transfer Function (PTF) method [128] the subsystems are coupled at their interfaces through impedance relations. An example on the combination of the

PTF with Finite Element models was given in [129] and showed a good potential for the improvement of the numerical efficiency.

Order reduction techniques are another possibility to consider. As mentioned before, the eigenvalue problem associated to a poroelastic domain is non-linear in the frequency. Consequently, standard reduction approaches are unsuited. Nevertheless, a few procedures to overcome this issue are in development and have been successfully applied to academic examples. Dazel [130] suggested the separation of the two phases into substructures, so that a decoupled mode basis could be defined for each one. However, such division procedure is inappropriate for poroelastic systems with a strong coupling between the two phases. A recent alternative to retain that coupling state was presented by Lappano *et al.* [131]. They proposed a parametric model order reduction (pMOR) scheme in which the frequency is the parameter of interest. The pMOR results could achieve a reduction in the required calculation time.

Besides, several publications address the convergence issues of the Finite Element analysis of poroelastic components. In [132] it was stated that more than twelve linear elements per wavelength are required in compression problems. Dauchez *et al.* [133] analyzed in detail the convergence performance of the different wave types for the displacement formulation. Using linear elements, the classical rule of six elements per wavelength also works for each of the propagating waves in a one-dimensional problem. For three-dimensional propagation, nevertheless, the convergence is slower and this criterion was found to be insufficient. One of the causes of this behavior is the locking of the poroelastic elements undergoing bending deformation. In this state, the interpolation of the linear elements is not enough and results in an excessive stiffness predicted by the numerical model. In their work two types of locking were identified. First, the shear locking associated to a bad interpolation of the deflection. This can be solved by a mesh refinement in the in-plane direction, either with a larger number of elements or with a higher order of the basis functions. Second, the locking because of a bad interpolation of the dilatation in the thickness direction, which leads to the so-called thickness locking. A refinement in the thickness direction helps to alleviate this kind of locking problem. The investigation could not derive a rule for the minimal number of elements per wavelength for poroelastic materials. In addition, the use of elements with order higher than one was recommended. Further studies dealt with the implementation of hierarchical elements for the resolution of the poroelasticity equations, as for example the work by Rigobert [134] and by Hörlin [135]. Hierarchical elements employ high order polynomials for the interpolation of the basis functions, which allows for a significant reduction of the number of nodes, as well as it reduces the locking phenomena. Another interesting aspect included in [134] in order to optimally exploit the numerical properties of the hierarchical elements was the use of different interpolation orders for each of the two phases. To sum up, high order elements show a big potential to improve the performance of Finite Element Method applied to three-dimensional poroelastic materials.

In the scope of the present investigation, quadratic basis functions have been employed, which are the only high order elements currently available in commercial vibroacoustic programs. The minimum size of the poroelastic elements necessary to achieve converged results has been examined for the different foam samples and for each material formulation available. Exemplarily, some results are next shown for a 10.8 mm thick layer of the material sample A, whose measured properties are summarized in Tables 4.1 and 4.2. The corresponding wavelengths are displayed in Figure 4.11. The wavelength λ_0 of the longitudinal wave propagating in the free air is also included for completeness. The three

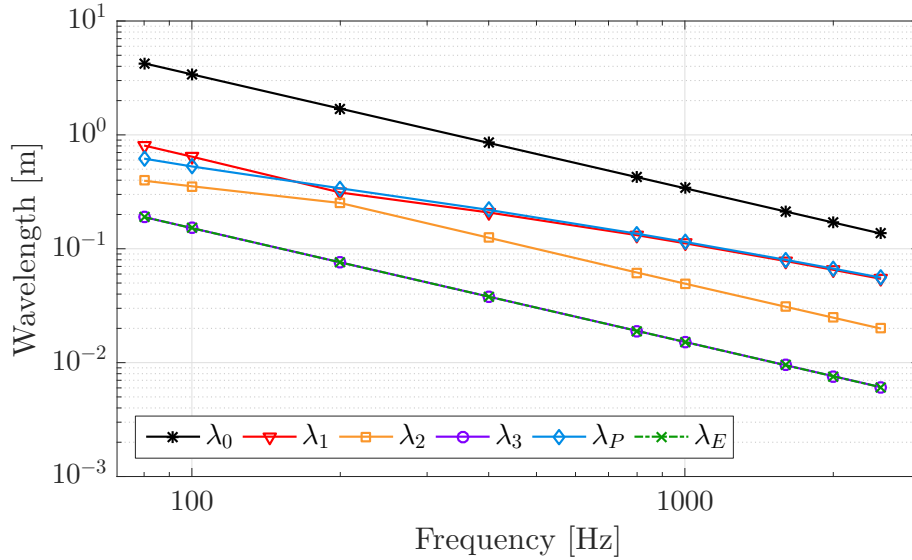


Figure 4.11: Wavelengths for air λ_0 and for the poroelastic material A in the different formulations: poroelastic (λ_1 , λ_2 , λ_3), porous (λ_P) and elastic (λ_E).

bulk waves of the poroelastic formulation are denoted as λ_1 , λ_2 and λ_3 . The wavelength associated with the porous simplification λ_P has a similar length as the largest of the compressional poroelastic waves λ_1 , whereas the shear wave of the elastic simplification has a wavelength λ_E that is as long as the shear wave of the poroelastic model λ_3 . This last fact suggests that similar mesh requirements may apply to the full poroelastic formulation and the elastic simplification.

Parameter	E	ρ	ν	η	h	c_0
Units	Pa	kg m^{-3}	-	-	mm	m s^{-1}
Steel plate	2.1e11	7800	0.31	1.0%	0.75	-
Heavy layer	2.4e8	1390	0.33	24.0%	2.80	-
Air	-	1.225	-	0.0%	-	340

Table 4.3: Material properties for the elastic and fluid components employed in the convergence analysis.

The convergence behavior has been investigated with the help of the cavity setup displayed in Figure 4.12. All lateral surfaces of the fluid cavity were set to be rigid but one. There, a spring-mass system formed by the poroelastic layer and an elastic plate (also called heavy layer) was attached to a thin steel plate. Such multi-layered aggregates are the main subject of the research in the next chapters. The material properties employed for the steel plate, the heavy layer and the air are summarized in Table 4.3. The excitation came from a point force of an amplitude of 1 N that was acting on the steel plate. The vibrational energy was then transmitted to the spring-mass system, which radiated into the fluid cavity.

Different quantities are at disposal to evaluate the working performance of the tested discretizations. On the one hand, one can make use of spatially averaged results such as the average pressure level inside the cavity, or the mean vibrational state or dissipated

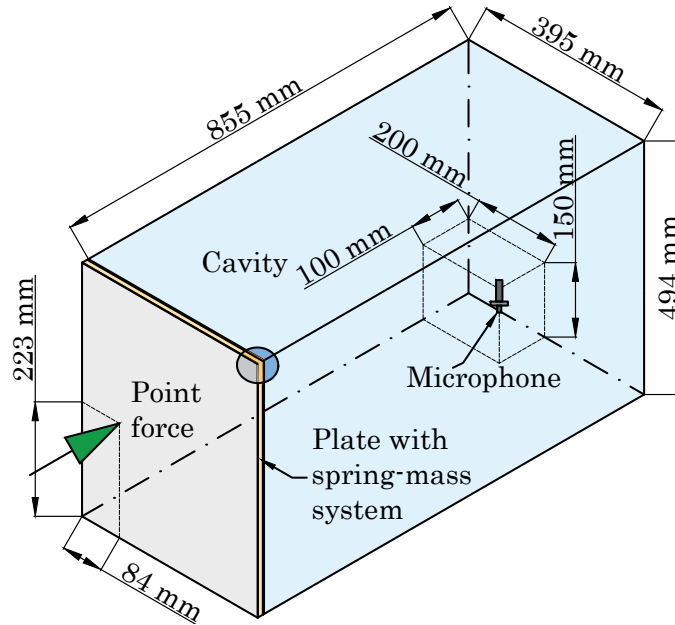


Figure 4.12: Cavity configuration employed for the convergence analyses.

power of each structural component. On the other hand, local variables can be used too. For this purpose, a microphone was placed inside the air cavity, so that the sound pressure level at the point indicated in Figure 4.12 could be retrieved. It was observed that both local and averaged results lead to the same conclusions and could be indistinctly employed in the analyses. Like in the previous chapter, the percent deviation (Eq. (3.33)) is applied to compare the calculated quantities. The reference value is indicated in each case.

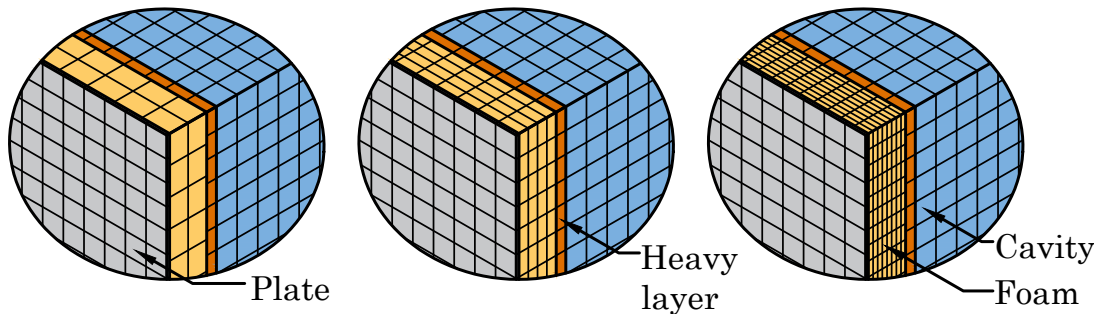


Figure 4.13: Detail view of Figure 4.12 with different mesh discretizations employed for the foam component. The modified parameters are the lateral size of the elements e and the number of layers in the thickness direction t : (left) $e = 8$ mm, $t = 2$, (middle) $e = 6$ mm, $t = 4$, (right) $e = 4$ mm, $t = 8$.

The element size of all components except for the poroelastic layer remained unchanged during the tests. The steel plate and heavy layer were each discretized with a layer of 6 mm quadratic solid shell elements, whereas the fluid cavity was divided with 6 mm linear hexahedral elements. These meshes were selected to be fine enough so that the mesh discretization of the foam component was the only influence factor on the convergence of the results.

As previously stated, two kinds of locking may affect the convergence of poroelastic elements. To avoid these issues, we examined the response of the foam to the refinement in the thickness direction (number of layers in the thickness direction t was varied from one to eight) and in the in-plane direction (lateral element size e ranged between 4 mm and 10 mm). Both parameters were combined, giving a total of 20 different meshes. The detail views in Figure 4.13 depict some of the meshes studied.

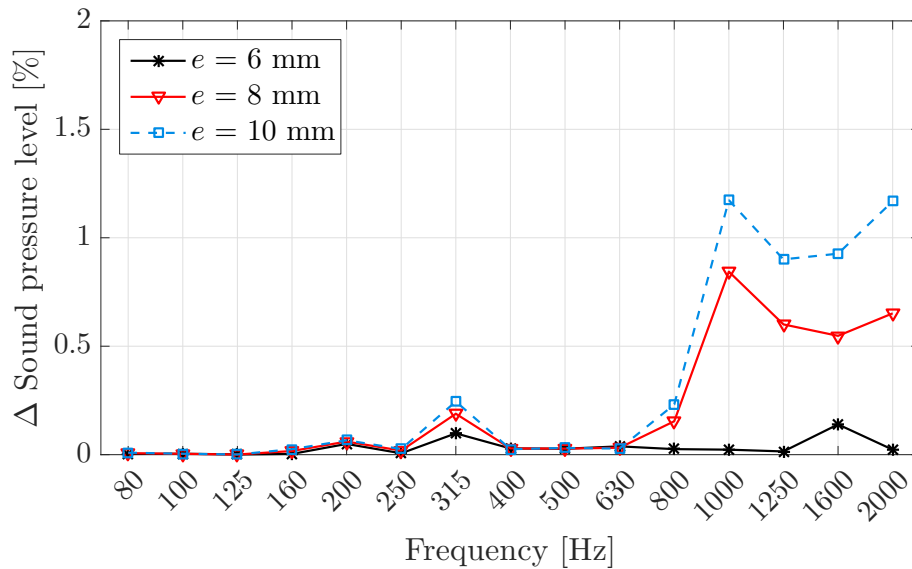


Figure 4.14: Percent deviation in sound pressure level at the microphone position for the poroelastic formulation with eight layers in the thickness direction and different element sizes. The reference solution has 4 mm elements.

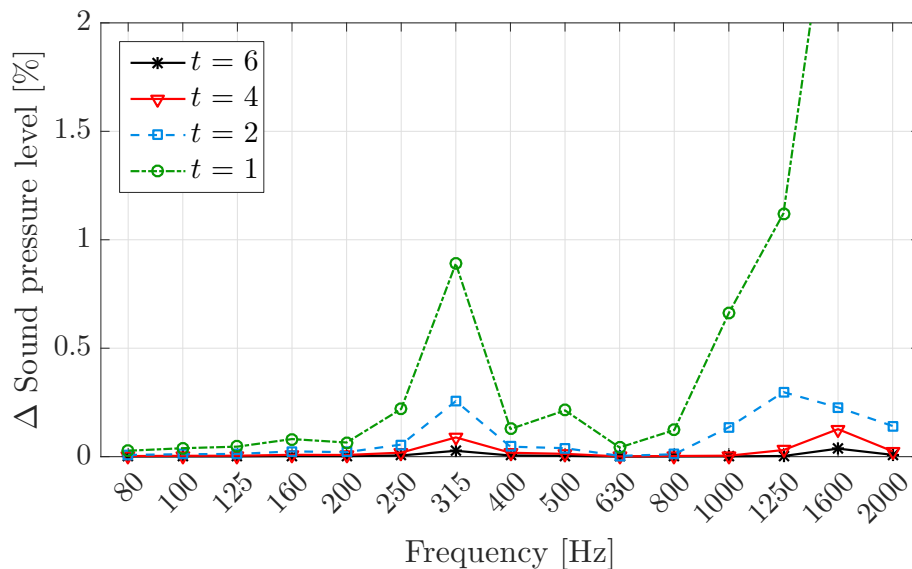


Figure 4.15: Percent deviation in sound pressure level at the microphone position for the poroelastic formulation with 6 mm elements and different thickness discretizations. The reference solution has eight layers in the thickness.

First we analyzed the impact of the element size e with fixed eight layers in the thickness direction, which was the finest discretization considered for this parameter. Figure 4.14

displays the variation in the sound pressure level at the microphone position between the different element sizes and the reference configuration with elements of a lateral size $e = 4$ mm. All the results in this section have been averaged in third bands in order to improve legibility, unless otherwise indicated. One can observe that the model with 6 mm elements is good enough, with a maximum deviation of 0.2 % with respect to the reference. The other two coarser meshes diverge from the reference solution as the frequency increases.

Next, the effect of the thickness refinement for the 6 mm element mesh was investigated. The reference solution had eight layers in the thickness direction. The pressure variations in Figure 4.15 show that at least more than one element should be used in the thickness direction, and a minimum of four layers are necessary to obtain results for the poroelastic formulation with a deviation under 0.2 %.

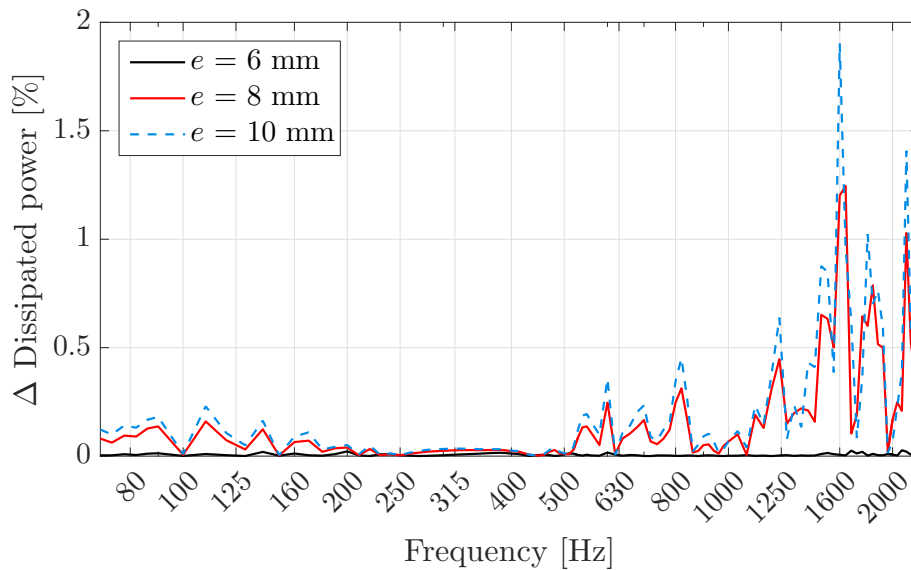


Figure 4.16: Percent deviation in the structurally dissipated power for the elastic formulation with eight layers in the thickness direction and different element sizes. The reference solution has 4 mm elements.

Besides that, since the shortest wavelength for the elastic simplification and for the full poroelastic formulation have the same length, it was expected that the two material models exhibit a comparable convergence behavior. As an example, the difference in the dissipated power by the structural losses inside the foam is represented in Figure 4.16 for the elastic formulation in narrow band. Analogously to the first test for the poroelastic model, the number of layers in the thickness direction was set to eight and the element size was modified. A discretization with $e = 4$ mm serves as reference. Like for the poroelastic model, an element size of 6 mm provided a converged result with almost no distinguishable deviation with respect to the fine 4 mm mesh.

In contrast, as shown in Figure 4.11, the wavelength for the porous model is of the same order of magnitude as the first compressional wave and, thus, much larger than the poroelastic shear wave. For this reason, when modeling a foam component as a porous material, it is possible to employ a much coarser mesh without affecting the accuracy. If we compare the results in Figure 4.17 for the porous model to the ones obtained with the poroelastic formulation in Figure 4.15 we observe that the deviations due to the thickness refinement are at least three orders of magnitude smaller.

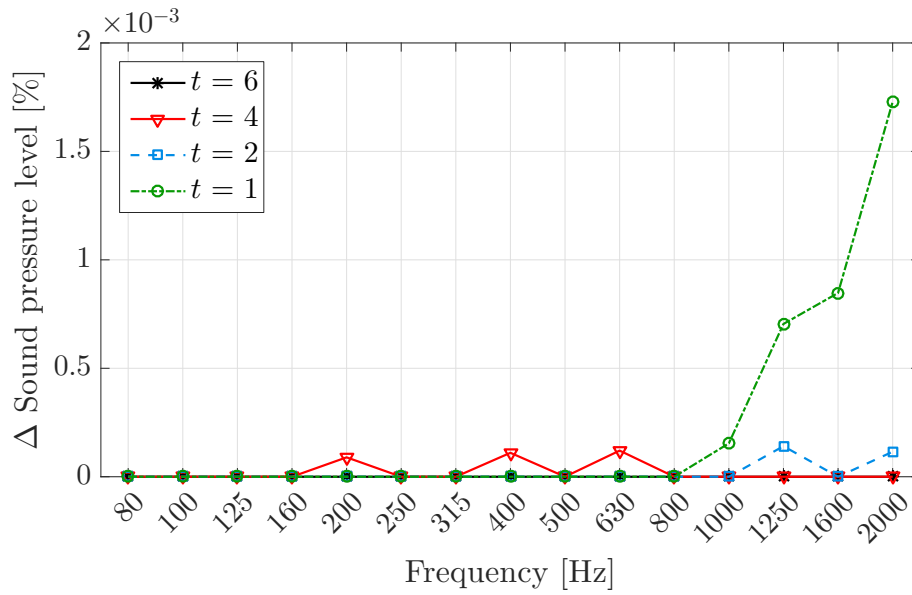


Figure 4.17: Percent deviation in sound pressure level at the microphone position for the porous formulation with eight layers in the thickness direction and different element sizes. The reference solution has 4 mm elements.

In short, no general mesh criterion could be derived to ensure the convergence of the Finite Element discretization with poroelastic media. Therefore, an explicit analysis is necessary for each material. The use of second or higher order elements is recommended to minimize the locking issues and to speed up the convergence. Since the propagating wave predicted by the porous model is larger than the waves in the poroelastic and the elastic formulations, the use of a specific, coarser mesh is advisable for this model.

Chapter 5

Evaluation of vibroacoustic models for poroelastic media

In the present chapter the performance of the numerical models for poroelastic media proposed in Chapter 4 are evaluated in a real application environment. The main focus of the investigation lies on the utilization of poroelastic materials in spring-mass systems, which are two-layered aggregates composed of a foam layer and a visco-elastic damping layer, the latter usually designated as heavy layer. For the evaluation of the predicted vibroacoustic behavior, the simulated results for different materials have been compared to measured data obtained in a window test bench. The chapter begins with an explanation about the vibroacoustic performance of spring-mass systems. The configuration employed for the investigations is introduced in Section 5.2. Next, the experimental procedure to obtainment of the reference information is explained. After that, the contrast between the measured and calculated results follows in Section 5.4. At the end of this chapter, the conclusions on the suitability of the presented models are summarized.

5.1 Working principle of spring-mass systems

The object of the following analyses are the so-called spring-mass systems. They are acoustic insulators based on the working principle of double walls, that is, the insulation behavior of the aggregate is better than that of two single walls added. The filling of the middle gap with an absorbing material such a poroelastic layer further enhances the performance. For this reason, spring-mass systems are widespread as passive noise control treatments in automotive applications [7]. One of the most common examples is located in the upper part of the firewall area, as depicted in Figure 5.1. The steel sheet of the firewall is the first wall, and the second wall is a visco-elastic damping layer made of bitumen or heavy rubber commonly known as heavy layer. The poroelastic middle layer may have a varying thickness in order to facilitate the geometrical integration.

The acoustic behavior of a spring-mass system employed as a sound barrier is usually described by either the transmission loss (TL) in Eq. (3.32) or the insertion loss (IL) curves. The insertion loss is defined as the difference between the transmission loss of the plate with the attached noise control treatment (NCT) and the transmission loss of the bare basis plate, as indicated in Eq. (5.1).

$$IL [dB] = TL_{NCT} [dB] - TL_{plate} [dB] \quad (5.1)$$

In Figure 5.2 a typical curve progression for the transmission loss of a laterally infinite single wall partition is compared to the performance of double walls with the same total mass. The presence of the elastic gap between the two walls or plates forms a vibration

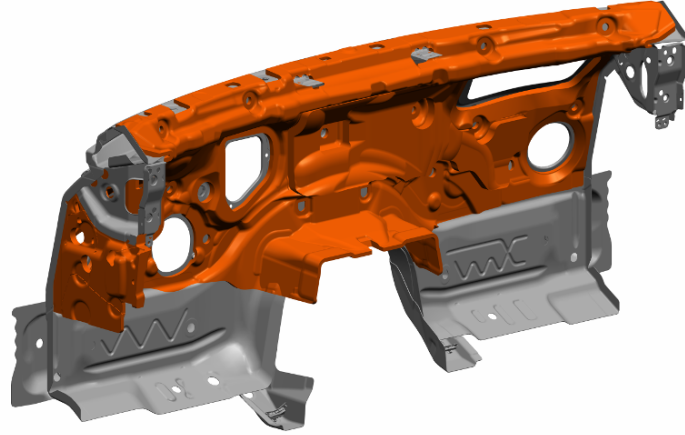


Figure 5.1: Firewall of a passenger car including the insulating spring-mass system on the upper section (marked in orange).

system. The plates have the mass per unit surface $m_1'' = \rho_1 d_1$ and $m_2'' = \rho_2 d_2$, respectively, and the spring constant per unit surface of the gap is K'' . The natural frequency of the spring-mass system f_{res}^{S-M} is approximated by [136]:

$$f_{\text{res}}^{S-M} = \frac{1}{2\pi} \sqrt{\frac{K''}{m''}} \quad (5.2)$$

with

$$m'' = \frac{m_1'' \cdot m_2''}{m_1'' + m_2''} \quad (5.3)$$

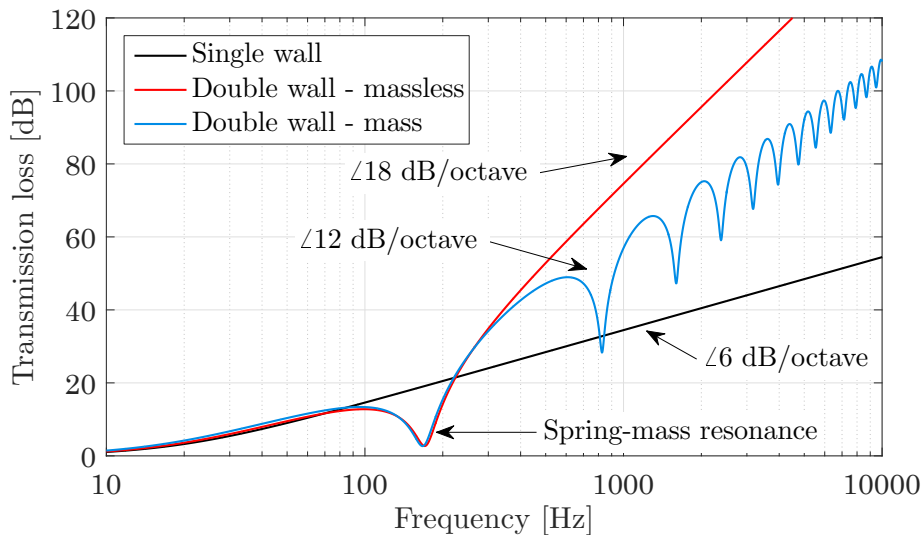


Figure 5.2: Typical transmission loss curves for flat single and double wall systems of infinite lateral extent (adapted from [26]).

We can identify three regions in the transmission loss curve progression of spring-mass systems. Below the resonance frequency, the behavior of the double wall system does not improve that of the single wall. At the spring-mass resonance there is a visible degradation of the insulation performance. The strength of this resonance depends on the damping

properties of the middle layer or gap. The resonance frequency is the most important design criteria of spring-mass systems. In order to avoid undesirable effects, its value should be chosen so low that it is not excited in the frequency range of interest [137].

Above the resonance, the performance of the double walls is notably superior to that of a single wall. The theoretical improvement results in a three times larger slope in the high frequency range of 18 dB/octave (curve labeled as *Double wall - massless*) in contrast to the 6 dB increase per frequency doubling for a single wall. For real applications, however, in which the material between the two plates has a finite mass, this maximum insulation cannot be reached because of several resonances that appear in the middle layer (curve labeled as *Double wall - mass*). These resonances are not associated with the double wall dynamics, but caused by standing quasi-longitudinal waves in the elastic middle layer [26], hence they are also designated as thickness resonances [127]. The position of those minima can approximately be determined with Eq. (5.4). The high frequency slope is the second design parameter when evaluating the insulation of a spring-mass system.

$$f_{\text{res}}^{\text{HF}} = \frac{n}{2h} \sqrt{\frac{E}{\rho_1}} \quad \text{with } n = 1, 2, \dots \quad (5.4)$$

Briefly, during the design process of spring-mass-like acoustic treatments two features determine the suitability of a system for a given application. Those are the value of the resonance frequency $f_{\text{res}}^{\text{S-M}}$ and the slope of the transmission or insertion loss curves above this resonance. Therefore, the analyses of the results in the following sections pay particular attention to the right prediction of these two quantities.

5.2 Description of the numerical configuration

A correct prediction of the acoustic performance of a spring-mass system requires a proper description of the dynamic behavior of the poroelastic middle layer. The evaluation of the material formulations presented in Section 4.1 is conducted with the help of a vibroacoustic Finite Element model. The basis geometry is a one-meter square flat steel plate of thickness 0.76 mm, which is a common value in the automotive constructions. Different spring-mass systems containing the foams characterized in the previous chapter are attached to this plate.

The setup for the numerical analyses is homologous to the configuration applied in Section 3.2 for the convergence study of a radiating steel plate. The only difference is that the spring-mass system is now placed between the plate and the receiving fluid, as Figure 5.3a illustrates. The main characteristics of the selected setup are shortly recalled. The system is excited through a diffuse pressure field acting on the outer surface of the steel plate. In the FE model, the diffuse excitation is represented by the superposition of plane waves. As previously indicated in Section 3.2, the statistical information of the incident field is summarized in a Cholesky decomposition of the cross power spectral density with 30 realizations. The finite volume of the receiving domain has a lateral size and a height of 100 mm and is discretized with linear elements of a maximum length of 17.3 mm. The Sommerfeld radiation condition is fulfilled by the numerical extension of the fluid domain with infinite elements whose basis functions are of 10th order. After each simulation, the total input power acting on the steel plate W_{in} and the power radiated on the outer surface of the finite fluid W_{rad} are retrieved to calculate the transmission and insertion losses.

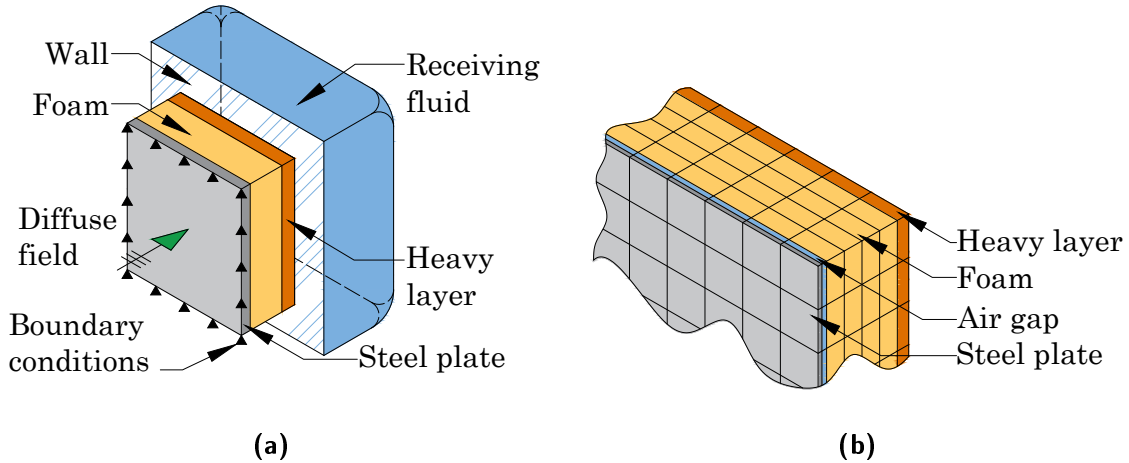


Figure 5.3: Model employed for the Finite Element calculations: (a) schematic representation (note that the thicknesses are not scaled), (b) detail view of the mesh discretization for the decoupled mounting condition.

For the structural components second order elements have been chosen. The steel plate as well as the heavy layer are discretized with a single layer of quadratic solid shell elements of 8 mm length. The displacement of the nodes on the outer edges of the steel plate has been restricted in the transverse direction in order to represent a simply supported boundary condition. For the discretization of the foam middle layer an analysis analogous to the one described in Section 4.2 must be conducted for each material, since the different samples do not have the same wavelengths and no general discretization rule could be yet derived for poroelastic materials. Because of the flat, regular geometry only hexahedral elements are used. The number of degrees of freedom (DOFs) at each node depends on the chosen material description. Four DOFs are needed for the full poroelastic formulation (three solid displacement components and one acoustic pressure), one DOF in the case of the equivalent porous model (acoustic pressure) and three DOFs for the elastic model (three solid displacement components). The lateral faces of the foam layer are acoustically rigid, that is, no acoustic energy is radiated through these surfaces, whereas the structural DOFs are set free.

Parameter	E	ρ_s	ν	η	h_s	$m'' = \rho_s h_s$
Units	Pa	kg m^{-3}	-	-	mm	kg m^{-2}
Heavy layer 2	2.52e8	1693	0.33	22.3%	1.17	1.98
Heavy layer 3	2.40e8	1390	0.33	24.0%	2.80	3.89
Heavy layer 4	2.42e8	1753	0.33	19.5%	2.29	4.01

Table 5.1: Material properties for the visco-elastic heavy layers.

The coupling conditions of the poroelastic layer to other components have a large impact on the dynamics of the material and, consequently, influence the suitability of a given model to describe the foam behavior. Several publications addressed this issue at frequencies under 1 kHz from a numerical point of view [19, 106, 138], highlighting that the interface conditions strongly affect the relative importance of the different dissipation mechanisms in the system. To account for different mounting conditions between the

steel plate and the poroelastic layer two setups are proposed. In the first configuration the two components are directly coupled at the complete interface, whereas the second setup includes a thin air gap in order to decouple the plate from the foam. A detail view of the decoupled FE mesh can be seen in Figure 5.3b. Preliminary investigations showed that the thickness of this gap has a relatively small influence on the overall results, as it is later detailed described in the section 5.4, Figure 5.12. Hence, a value of 1 mm for the gap thickness is adopted. This air gap is discretized with second order hexahedral elements of 8 mm length to simplify the coupling to the structural components. The heavy layer and the porous material are directly connected at their interface nodes for all configurations.

In some cases, because of the different element size of the foam discretization with respect to the plate and heavy layer components, there exists a mesh incompatibility, that is, the nodes of the adjoining bodies are not located in the same positions. The coupling of the non-congruent meshes at each face of the poroelastic layer is handled with the help of an interface, a numerical tool that projects the nodes of the first coupling surface onto the second coupling surface to ensure the continuity of the field variables [139]. The projection procedure is exemplified in Figure 5.4. The surface with the finest discretization is selected as coupling surface 1. For the projection, a pseudo-mesh is built around the coupling surface 2. Two geometrical parameters control the dimensions of the pseudo-mesh. The gap tolerance determines the size of an extrusion of the elements of the second surface in its normal direction. The plane tolerance is a percent extension of this extrusion in all directions. The nodes of the coupling surface 1 that are located inside of the pseudo-mesh are projected onto the coupling surface 2. For instance, the projection of the node 1 is 1'. Note that in the example in the Figure the node 5 cannot be projected since it is outside of the pseudo-mesh. Later, during the calculation step, the results of the projected nodes on the coupling surface 2 are mapped to the original nodes in the coupling surface 1.

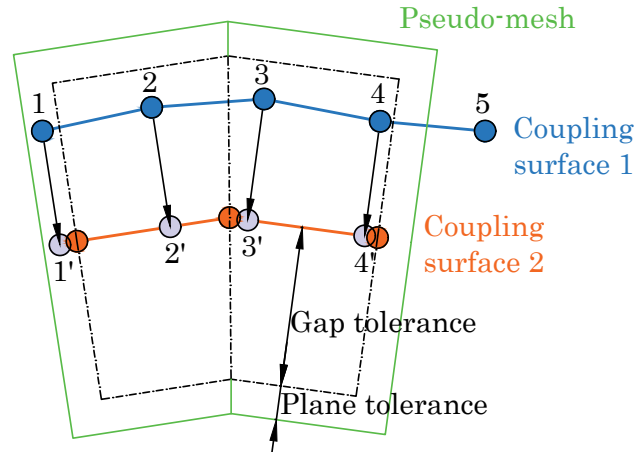


Figure 5.4: Projection procedure for non-congruent meshes with the help of an interface (adapted from [139]).

The material properties employed for the different components have been previously indicated in Tables 4.1, 4.2, 4.3 and 5.1. In the following sections the spring-mass systems are named with an alphabetic and a numeric letter that correspond to the foam sample and the heavy layer, respectively. For example, the spring-mass system B3 is composed by the foam B in combination with the heavy layer 3. A summary of the type, order and number of nodes for each component are given in Table 5.2. The information concern-

Component	Element type	Order	Max. size	Nr. nodes
Plate	Solid shell	2 nd	8 mm	110628
Heavy layer	Solid shell	2 nd	8 mm	110628
Receiving fluid	Hexa/Tetrahedral	1 st	17 mm	82103
Air gap	Hexahedral	2 nd	8 mm	110628

Table 5.2: Details of the numerical model for the one-meter square configuration.

ing the poroelastic component is specified in the next sections, since the meshes vary in element size and number of layers for each tested foam material.

5.3 Measured data for verification

To assess the quality of the numerical predictions and to be able to compare the performance of the different material formulations, several validation measurements were conducted in a window test bench. This test facility is commonly employed for the determination of the airborne insulation [140]. It is formed by two decoupled rooms as displayed in Figure 5.5a, a reverberation chamber and a semi-anechoic room, that are acoustically connected through an opening called window. The test object is placed in this opening. A loudspeaker located in the reverberation chamber produces a broadband diffuse pressure field of amplitude 95 dB that acts upon the test object. The volume of the reverberation chamber (218 m³) ensures the diffusivity of the excitation above 80 Hz. The analyzed plate is fixed on its edges to the frame of the window with plastic sealing material in order to avoid any acoustic leakages.

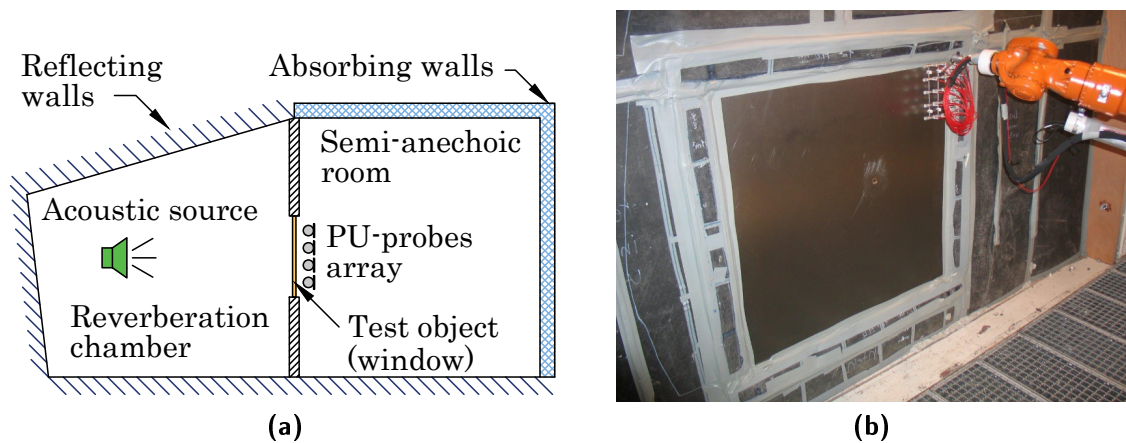


Figure 5.5: Experimental setup: (a) schematic representation of a window test bench: reverberation chamber with the acoustic source on the left, semi-anechoic room with PU-probes array on the right. The test object is placed in the opening window of the partition wall, (b) scan array with PU-probes mounted on the robotic arm in front of a bare steel plate.

The receiving room has absorbing lateral walls and ceiling. The floor of this chamber is reflecting, which serves to realistically represent the radiation conditions of a car on the

road. Inside this semi-anechoic room the acoustic energy transmitted through the test object is determined. To that end, the surface of the sample is scanned in the near field with the help of an array of 1/2 inch Microflow mini PU-probes [141] (Figure 5.6). A PU-probe is a sound probe combining two sensors: a traditional electret condenser microphone and a velocity transducer. The velocity sensor is formed by two wires that are heated at approximately 200°C and whose resistance is dependent on the temperature. When the air moves through the sensor, there is a small temperature shift between the two wires and, consequently, a difference in their resistance that is proportional to the velocity. This way, a PU-probe allows to directly measure at one spot the sound pressure and the acoustic particle velocity simultaneously. The main advantage of the PU-probes compared to the standard PP-probes is that they are less sensitive to background noise [142], which makes them especially appropriate for tests in operational conditions. An accurate measurement requires a delicate phase calibration between the two sensors so that phase mismatch errors are prevented. The PU-probes were calibrated up to a frequency of 6.3 kHz. However, for some material samples with great insulation properties the radiated power at higher frequencies is so low that the ambient noise masks it. For this reason, the measured data has been systematically evaluated up to a frequency of 4 kHz.

The scan array contains twenty PU-probes that are separated from each other by 50 mm, as Figure 5.6b illustrates. To facilitate the measurements and ensure reproducibility, the array is mounted on a robotic arm that systematically moves on a plane 60 mm above the steel plate (Figure 5.5b). Twenty array positions are successively scanned to cover the complete surface of the one-meter square plate, which results in 400 measurement points. The total radiated power W_{rad} is obtained by integration of the normal intensity I_n over the test object surface S . The effective intensity is defined as the time averaged product of the pressure and the normal particle velocity $\langle p v_n \rangle_t$. For harmonic complex variables that product can be calculated out of the complex moduli of the pressure \hat{p} and the normal velocity \hat{v}_n , as indicated in Eq. (5.5) [143]. Lastly, since just a finite number of points i are measured on the surface S , the integral is approximated as a summation for all partial surfaces S_i .

$$W_{\text{rad}} = \int_S I_n dS = \int_S \langle p v_n \rangle_t dS = \int_S \frac{1}{2} \text{Re} (\hat{p} \hat{v}_n^*) dS \approx \frac{1}{2} \sum_i \text{Re} (\hat{p}_i \hat{v}_{n,i}^*) \Delta S_i \quad (5.5)$$

For the evaluation of the experimental results along this thesis, the measured information was exported from the software PAK. This is a test bench measurement system for data acquisition, analysis, assessment and management [144]. In order to validate the configuration set for the export of the data, a simple model with known analytical solution was selected. The one-dimensional duct represented in Figure 5.7 has a piston located at $x = 0$ that oscillates with a velocity amplitude V_0 and a circular frequency ω :

$$v_0(t) = V_0 \exp(-j\omega t) \quad (5.6)$$

At a position situated a distance x downstream of the source, the pressure p and the velocity v are given by:

$$p(x, t) = \rho_0 c_0 V_0 \exp(-j[\omega t - kx]) = \hat{p} \exp(-j\omega t) \quad (5.7)$$

$$v(x, t) = V_0 \exp(-j[\omega t - kx]) = \hat{v} \exp(-j\omega t) \quad (5.8)$$

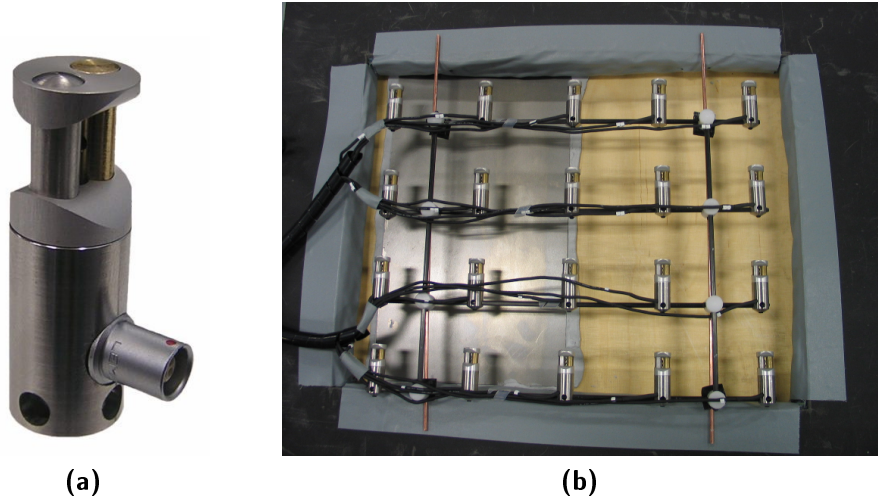


Figure 5.6: The Microflown PU-probe: (a) detail view of a PU-probe, (b) scan array employed in the measurements formed by twenty PU-probes.

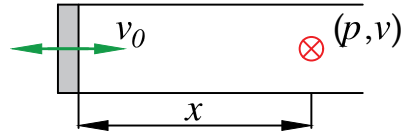


Figure 5.7: Model for one-dimensional wave propagation in a duct with velocity excitation.

where ρ_0 and c_0 are the density and the sound velocity of the filling fluid, respectively, and $k = \omega/c_0$ indicates the wave number. Since no losses are present in the model, the averaged intensity I_{AVG} at every point of the duct remains constant and is equal to [145]:

$$I_{AVG} = \frac{1}{2} \rho_0 c_0 V_0^2 \quad (5.9)$$

In parallel, a transfer path network was built with the help of a PAK module with the structure described in Figure 5.8. A randomly selected velocity excitation is the input of the system. The pressure and velocity responses at the desired position are calculated as the product of the input variable by the corresponding transfer function (TF), which are specified in Eq. (5.10) and (5.11).

$$\text{TF}(p/v_0) = \rho_0 c_0 \exp(jkx) \quad (5.10)$$

$$\text{TF}(v/v_0) = \exp(jkx) \quad (5.11)$$

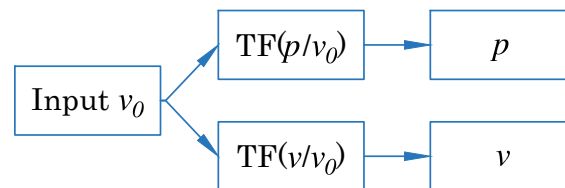


Figure 5.8: Transfer path network of a one-dimensional wave propagation in a duct.

The average intensity I_{AVG} is, by definition, obtained from the time averaged product of the pressure and velocity, which for harmonic quantities holds the relation [137]:

$$I_{AVG} = \langle pv \rangle_t = \frac{1}{2} \text{Re} (\hat{p} \hat{v}^*) = \frac{1}{2} \text{Re} (CPS\{p, v\}) \quad (5.12)$$

The real part of the product of the pressure with the complex conjugate of the velocity v^* is equivalent to the real part of cross-power spectrum (CPS) density between the Fourier transformation of the two variables [146]. The CPS density is the quantity to be calculated in PAK from the measured pressure and velocity data and to be exported for the further analyses. Adding the factor 1/2 to the cross-power spectrum density the total intensity is retrieved. The agreement between the analytical solution and the results obtained from the transfer path network for I_{AVG} is very high, with deviations below 0.04% in the third band averaged results. The export of the CPS values is, therefore, an appropriate quantity to evaluate the radiated intensity.

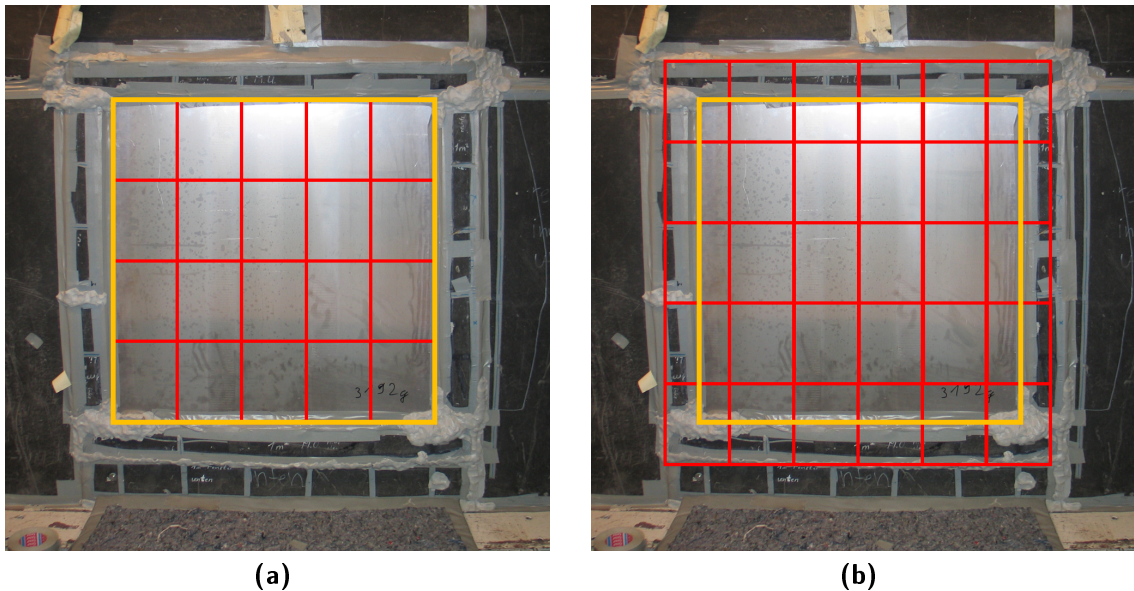


Figure 5.9: Scan array positions (in red) over the one-meter square steel plate (edges in yellow): (a) standard surface definition, (b) extended surface definition.

As already indicated before, the one-meter square surface is covered by twenty different array positions, as marked in Figure 5.9a. A preliminary test was carried out in order to check that the power radiated outside of this surface has a negligible contribution to the results. For this purpose, the scan surface was extended by half an array size in each direction, like Figure 5.9b shows. The total radiated power was then calculated first only with the probe positions inside the plate area, and secondly including the positions outside of the plate area. The deviation between the two values is below 0.6% in the whole frequency range. This fact confirms the assumption that the greatest part of the energy is radiated through the plate and that the measurement in the near field surface over the one-meter square plate is accurate enough. Moreover, this experiment was a good proof to verify that the window was properly sealed and that no undesirable leakages were present.

In an analogous way to the simulation setup, two mounting configurations are experimentally inspected. The measurements provide qualitative information about the influence

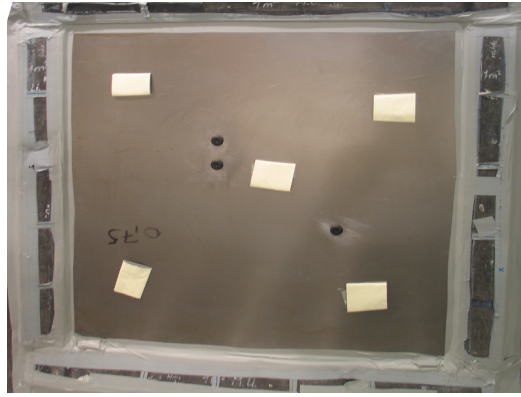


Figure 5.10: Location of the five discrete surfaces for the punctual bonding with double-sided adhesive tape.

of the bonding condition between the steel plate and the foam of the spring-mass system. The *coupled* state is achieved by a full-surface coupling with spray adhesive, whereas for the *decoupled* condition a punctual bonding with two-sided adhesive band at five discrete points (near the four corners and at the center point) is employed. An example of the distribution of the small bonding surfaces is displayed in Figure 5.10.

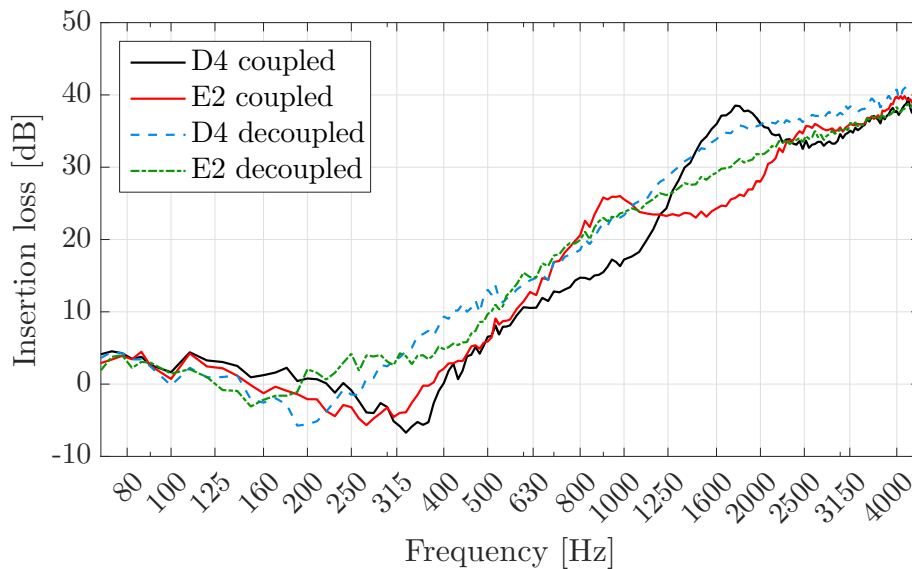


Figure 5.11: Measured insertion loss for the spring-mass systems D4 and E2 in the coupled (solid lines) and decoupled (dashed lines) configurations.

Figure 5.11 shows the measured insertion loss curves for the spring-mass systems D4 (foam sample D with heavy layer 4) and E2 (foam sample E with heavy layer 2). The decoupled configurations exhibit an overall higher and smoother insertion loss curve progression. The presence of the air gap slightly reduces the vibrational energy that is transmitted from the exciting plate to the skeleton of the foam and, thus, to the attached heavy layer. Moreover, the spring-mass resonance for the coupled setups is less damped and slightly shifted towards higher frequencies because of the stiffening effect introduced by the direct attachment of the foam. These observations are in concordance with the results found in [103, 147]. In the frequency range between 1250 Hz and 2500 Hz for the system D4 and between 630 Hz and 1250 Hz for the sample E2 we observe resonance peaks in the

coupled systems that are almost indistinguishable in the decoupled states. This effect points to the thickness resonance phenomena related to the solid phase of the foam that was introduced before in Section 5.1.

5.4 Comparison of numerical and experimental results

In the current section the center of interest is set on the evaluation of the proposed numerical models for the description of poroelastic foam layers. We examine the behavior of different spring-mass systems by comparing the numerical predictions with the experimental data. Another relevant aspect is the impact of the material parameters on the modeling strategy and on the overall results. The analysis of the results has shown that the response of the systems can be classified into two categories depending on the elasticity properties of the poroelastic layer. The foam samples A, B and F have a Young's modulus per unit thickness E/h over 1 kPa mm^{-1} and belong to the group of the stiff materials. Conversely, the material samples C, D and E are included in the class of the soft foams.

Coupling conditions between the foam and the steel plate

Firstly, we investigate the ability of the numerical model to recreate the two coupling conditions tested experimentally in the former section on the spring-mass system E4. For the coupled state, on the one hand, the degrees of freedom of the foam layer component are directly connected to those of the steel plate. On the other hand, two approaches are proposed for the representation of the decoupled setup. The one reproduces the exact mounting employed in the measurements by combination of a thin air gap between the steel plate and the foam together with five small surfaces on which the two components are directly numerically connected. The distribution of these surfaces is similar to that shown in Figure 5.10. The other configuration simplifies the setup by neglecting the small bonding surfaces. In this case only a continuous thin air layer at the interface between the steel plate and the poroelastic material is added. For the latter model different thicknesses for the air gap ranging from 0.1 mm up to 10 mm are simulated.

Because the changes in the overall performance are relatively small for the tested configurations, the results are shown in terms of the insertion loss difference, using a 1 mm thick continuous air layer as reference. Here, positive values indicate that more energy is dissipated than in the reference solution. In Figure 5.12 two exemplary gap thicknesses are displayed, namely, 0.2 mm and 5 mm. The largest differences are found in the low frequency range, and they decrease as the frequency increases. Above 400 Hz the maximum difference for all models is clearly below 0.5 dB, which supports the choice of a 1 mm air layer in the further investigations. The additional setup with the exact decoupled configuration of the experiment is labeled with *Point bonding*. Around the spring-mass resonance this partially decoupled bonding exhibits the greatest influence. This is due to the fact that at the spring-mass resonance the most energy is transmitted to the foam and, consequently, the structural damping of the foam has a large contribution to the total dissipated energy. For that reason, the point bonding configuration has over 1 dB insulation improvement in this frequency range. Outside the resonance the difference remains under 0.3 dB. These results confirm that the additional modeling effort to replicate the exact decoupled state is not necessary and that a continuous air gap can be employed.

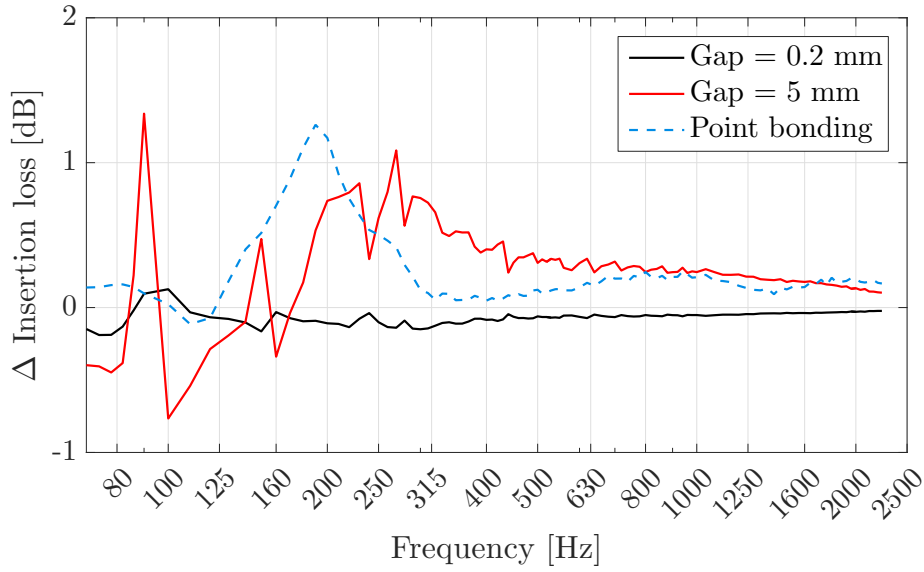


Figure 5.12: Difference in the insertion loss for different decoupled configurations for the spring-mass system E4. The reference solution has a continuous air gap with 1 mm thickness.

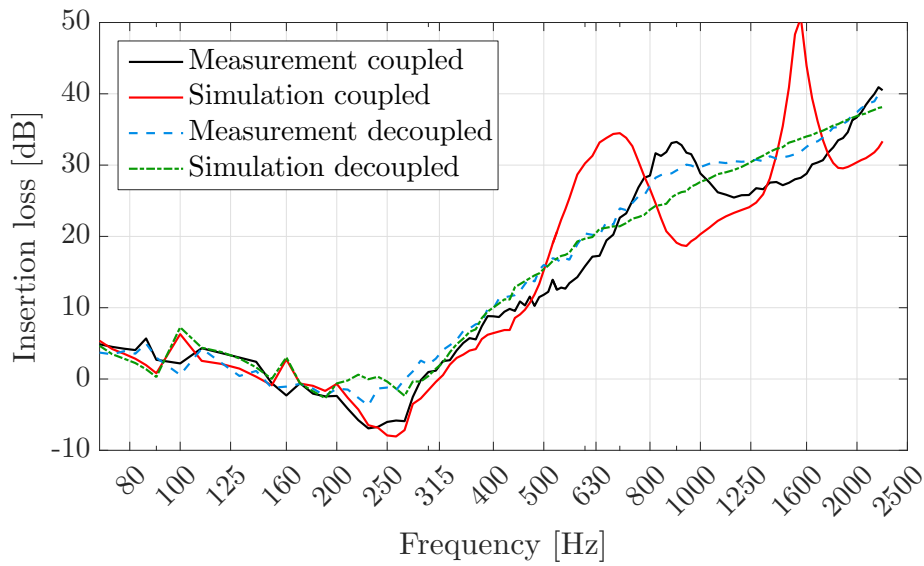


Figure 5.13: Comparison of the measured and simulated insertion loss for the spring-mass system E4 in the coupled (solid lines) and decoupled (dashed lines) configurations.

The insertion loss results for the foam material E with the heavy layer 4 in the two mounting configurations are compared to the corresponding measured information in Figure 5.13. For the Finite Element calculations the foam layer has been described with the full poroelastic formulation using the material parameters obtained in the characterization. The poroelastic component is discretized with six layers in the thickness direction of quadratic elements with 7 mm lateral length, giving a total of 557856 nodes for the foam. The resulting mesh incompatibility is managed by means of an interface, as indicated in Section 5.2. At a first glance, the numerical and the experimental data show qualitatively a good agreement and the predicted behavior meets the main evolution trends of the

reference data sets. Moreover, the differences between the coupled and decoupled states regarding the insulation level at the spring-mass resonance as well as the curve progression in high frequency are accurately captured by the models, which proves the correctness of the chosen modeling approach.

Soft foam in coupled state

Next, we inspect in detail each one of the mounting conditions separately. Figure 5.14 shows the results for the coupled configuration of the spring-mass system E4 with the three available material formulations for the foam layer, namely, the description as a poroelastic, porous and elastic component. Here, the constant elastic properties from the compression method [88] given in Table 4.1 have been used. We first remark that the poroelastic model accurately predicts both the frequency and the absolute power level at the spring-mass resonance. The high frequency resonances, however, appear at lower frequency values than observed in the measurement, which suggests that the assumed material properties underestimate the stiffness of the real foam in this frequency range. The deviations observed in the curve progression for the porous simplification directly originate from the absence of the elastic skeleton. On the one hand, the missing stiffness and damping in the spring-mass resonance range lead to an underestimation of the resonance frequency and of the insertion loss value. On the other hand, the solid phase is responsible for the high frequency resonances, which are consequently not present in the porous curve progression.

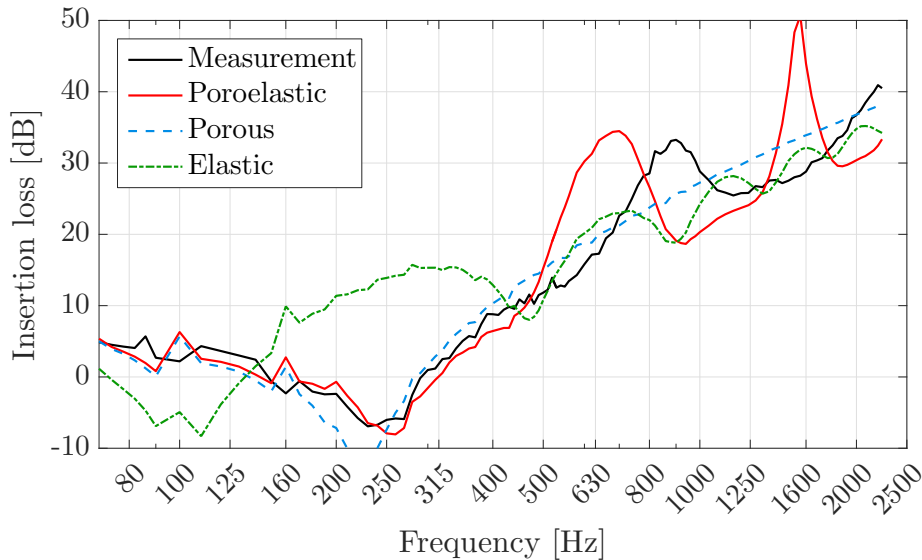


Figure 5.14: Comparison of the measured and simulated insertion loss for the spring-mass system E4 in the coupled configuration with different material formulations.

The behavior predicted by the elastic simplification for the middle layer widely differs from the experimental results in the low frequency range. In order to better understand this mismatch, we take a closer look at the origin of the two resonance phenomena. The first one is the characteristic resonance of double-wall systems, and its value can be approximated by the analytical expression in Eq. (5.2). The spring constant per unit surface K'' of the foam layer for a poroelastic material is defined by:

$$K'' = \frac{1}{h} \left(\tilde{K}_f + \frac{E(1-\nu)}{(1+\nu)(1-2\nu)} \right) \quad (5.13)$$

The variable h represents the thickness of the foam layer. It is important to highlight the two terms present in the equivalent spring stiffness K'' , which is equivalent stiffness of two springs working in parallel [148]. The first term is related to the fluid phase, the second term to the elastic phase. The fluid modulus \tilde{K}_f (previously defined in Eq. (4.11)) is always of the order of magnitude of the fluid bulk modulus ($P_0 = 101300$ Pa for air). For the foam material E, because of the relatively low elasticity modulus of the frame ($E = 15000$ Pa), the fluid phase dominates the position of the spring-mass resonance. For this reason, when making use of the solid modeling, the equivalent stiffness value is missing its major contribution and, therefore, the resonance frequency is largely underestimated. As the frequency increases, the resonances associated with standing waves in the middle layer are visible. We notice in Figure 5.14 that these high frequency resonances are present in both poroelastic and elastic descriptions at the same frequency values, which verifies the supposition that they correspond to the structurally induced thickness resonances in the foam. Those resonance frequencies are proportional to the square root the elasticity modulus of the foam (recall Eq. (5.4)), whereas the amplitude of the resonances and anti-resonances depends on a combination with other material parameters like the Poisson's ratio and the loss factor.

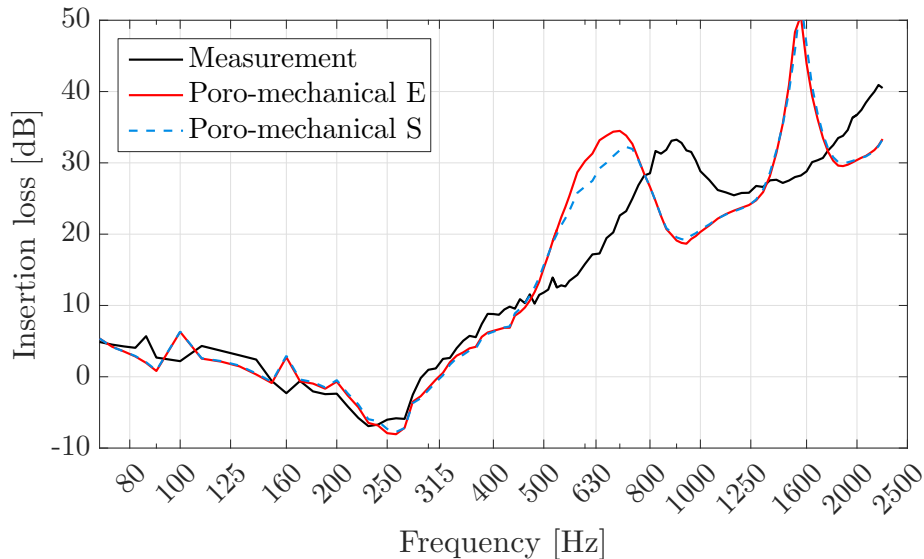


Figure 5.15: Comparison of the measured and simulated insertion loss for the spring-mass system E4 in the coupled configuration for the poroelastic formulation with two different sets of poro-mechanical parameters.

The following investigations examine how sensitive the numerical calculations are to the different poroelastic material properties. To that end, each of the four elastic and five poro-mechanical parameters are sequentially modified with a $\pm 10\%$ variation around their measured value. This variation is in the order of magnitude of the fluctuations observed during the characterization measurements due to the averaging of different test samples, between three and nine, for each material. The obtained results for the variation are compared to the solution with the average parameters in terms of the percent deviation of the transmission loss according to Eq. (3.33).

The influence of the poro-mechanical parameters is found to be almost negligible over the whole frequency range. The highest deviations are obtained for the thermal characteristic length Λ' with a local maximum deviation of 3.3% around the spring-mass resonance and

an average deviation of 0.4% over the complete frequency range of interest. This minor importance of the poro-mechanical properties serves as motivation to question whether a standard set of poro-mechanical properties could be employed. This set is defined as the average of the properties of all samples A to F and labeled with Sample S in Table 4.2. The calculated insertion loss results are displayed in Figure 5.15 together with the measured data and the values obtained with the poro-mechanical parameters of the foam sample E. The elastic properties remain here unchanged. The largest deviation between the two calculated curves is 6.8% and is located at the first high frequency resonance between 630 Hz and 800 Hz. The averaged deviation of 1.4% is a promising result that supports the utilization of the standard parameter set, especially since the correspondence to the measurement is only marginally modified.

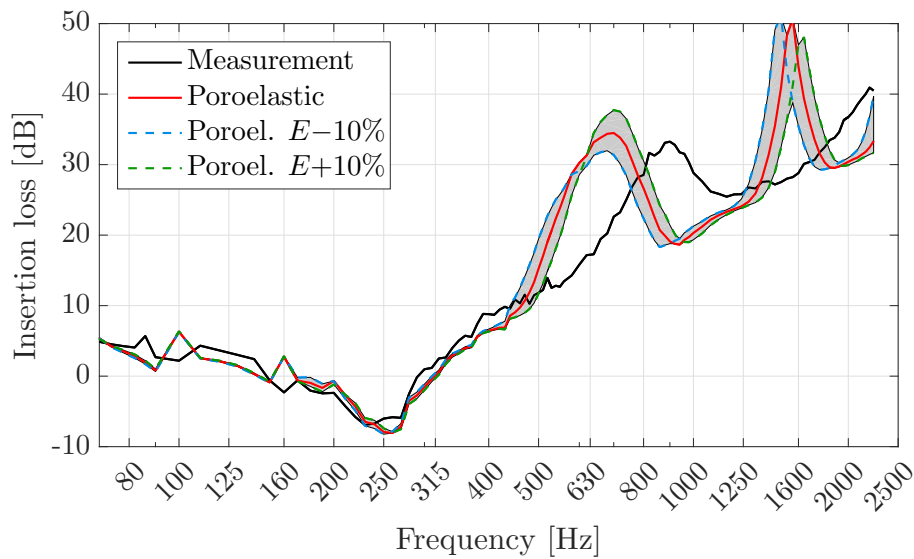


Figure 5.16: Comparison of the measured and simulated insertion loss for the spring-mass system E4 in the coupled configuration for the poroelastic formulation with a $\pm 10\%$ variation of the Young's modulus E .

A greater impact on the response of the model have variations of the elastic parameters. As an example, Figure 5.16 shows the insertion loss results for a $\pm 10\%$ variation of the elasticity modulus E . The values between the minimum and maximum curves have been colored. The trends when modifying the Poisson's ratio ν are very similar to the behavior of a variation of E and, therefore, are not shown here. The effect of the Young's modulus yields local and averaged deviations of 15.1% and 3.6%, respectively. In the case of the poroelastic modeling it is clearly seen that the location of the spring-mass resonance for this material is dominated by the stiffness of the fluid phase and, as a result, is not influenced by the modification of the frame properties. As expected, an increase of the elastic parameter E , or ν , leads to a general curve shift of the thickness resonances towards higher frequencies and, thus, to a slightly better fit with the reference data.

This means that, in order to further improve the agreement between the measured curve and the poroelastic formulation along the complete frequency range, the stiffness of the elastic phase should be larger as the frequency increases. To check this, we make now use of the elastic values obtained by the resonance method [89] indicated in the second column in Table 4.1, which reported a 22% larger elasticity modulus. The results are displayed in

Figure 5.17 as *Poroelastic (1)* for the parameters obtained from the compression approach and *Poroelastic (2)* for those from the resonance method. For the larger Young's modulus the correspondence in the range of the second resonance improves, reducing the averaged percent deviation with respect to the measured data from 12.4% to 11.5%.

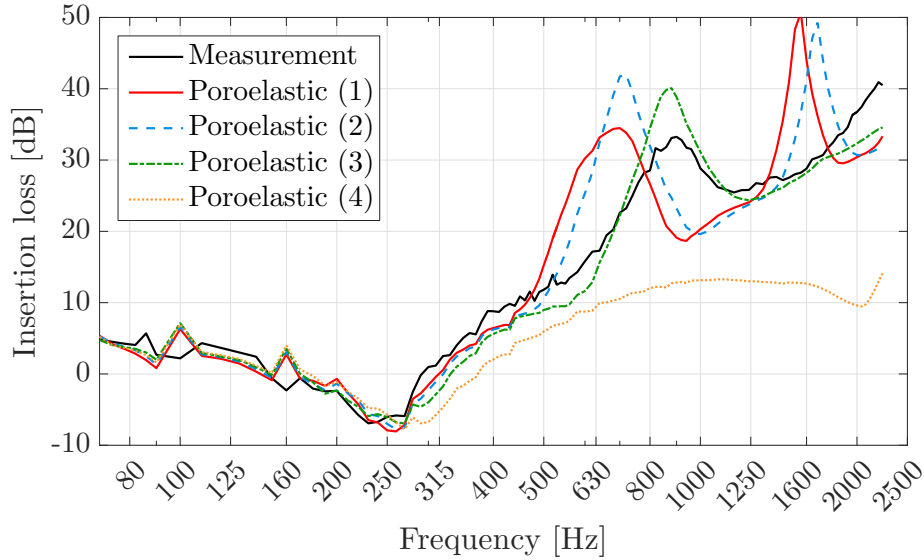


Figure 5.17: Comparison of the measured and simulated insertion loss for the spring-mass system E4 in the coupled configuration with different elastic foam parameters for the poroelastic formulation: (1) compression method, (2) resonance method, (3) frequency-dependent elasticity modulus, (4) dynamic characterization.

In another attempt to get a closer match in the high frequency range, a value for the Young's modulus was estimated with the help of Eq. (5.4) to better meet the resonances in the experimental curve. For the calculation of the curve *Poroelastic (3)* in Figure 5.17 we have employed a frequency-dependent progression for the complex elasticity modulus. The real part has a constant value of 25 kPa for frequencies under 1700 Hz and increases linearly up to 35 kPa for the upper limit frequency 2240 Hz. The damping coefficient η has its quasi-static value of 14.8% up to 450 Hz, then it linearly increases up to 29.6% by 1200 Hz and remains constant above this value. The frequency location of the first thickness resonance is now correct and its level can be adapted by, for example, increasing the damping. The second thickness resonance is accordingly shifted towards higher values too and, hence, no longer visible in the examined frequency range. The model with modified elastic coefficient reduces the standard deviation to 7.7%. The main disadvantage of this approach is that the estimation of the Young's modulus is only possible if measured data of the complete spring-mass system are available beforehand, which limits the practicability of this procedure. To overcome this issue, the dynamic characterization method introduced in Section 4.1 is applied.

The results of the dynamic elasticity characterization are summarized in Figure 5.18 together with the static values from the compression and resonance methods. The values obtained by the dynamic approach $E(f)$ are greater than the ones provided by the static methods for both the real and imaginary parts. Due to the limitation of the power provided by the exciting shaker, the characterization is only possible up to a frequency of 600 Hz. In order to extend the elasticity modulus towards higher frequencies, the experimental real and imaginary parts are approximated by a linear regression (labelled as

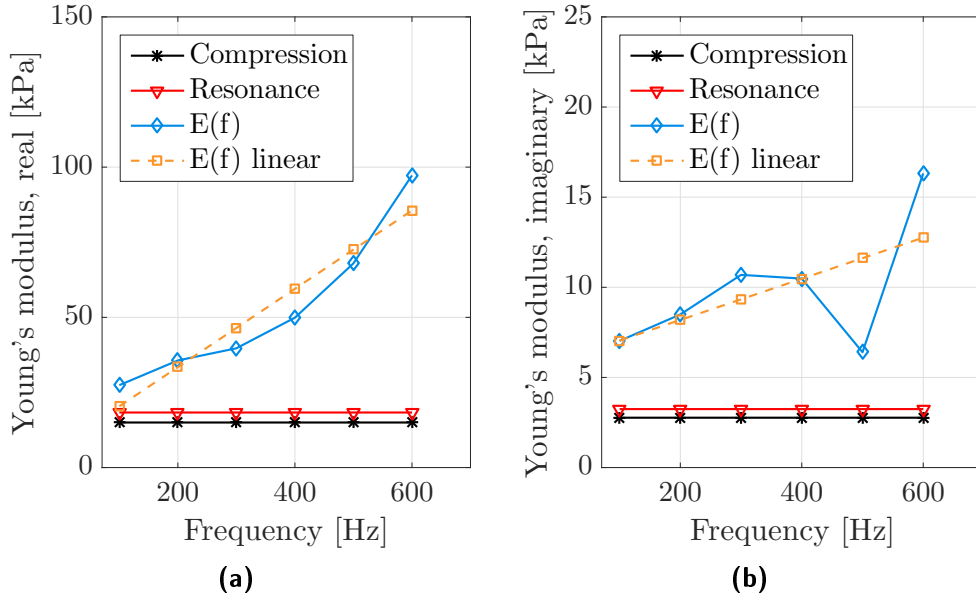


Figure 5.18: Comparison of the Young's modulus obtained with different characterization techniques for the foam sample E: (a) real part, (b) imaginary part.

$E(f)$ linear) and extrapolated to the high frequency range. The orange pointed line in Figure 5.17 (*Poroelastic (4)*) represents the calculated insertion loss curve for the poroelastic formulation with this linearized elasticity modulus from the dynamic characterization. The average deviation to the experimental reference increases up to 22.9%. Out of the curve progression, one can conclude that the determined Young's modulus is too stiff. The almost constant insertion loss value above 800 Hz suggests that the system does not behave like a spring-mass system anymore, but as a single plate with augmented mass. Additional investigations and modifications in the dynamic characterization methodology are still necessary to achieve the desired accuracy level and to obtain a reliable prediction of the elasticity properties [149]. Further insight into this topic is given later in Section 7.2.

Soft foam in decoupled state

For all the results analyzed above there was a direct coupling at the interface between the foam layer and the steel plate. Here, we examine the behavior of the same spring-mass system E4 when the two components are separated through a continuous thin air gap between them. Figure 5.19 shows the measured and calculated insertion loss curves for the decoupled state. The spring-mass resonance frequency and the total power level in this range are again well estimated by the poroelastic model. The first thickness resonances and anti-resonances are slightly visible in the measurement but cannot be observed in the simulation results. This can be attributed to the fact that the introduction of the air gap in the numerical model reduces the structural excitation of the foam skeleton to a higher degree than it actually does in the experimental setup. However, because of the vertical positioning of the system in the window test bench, it is difficult to identify the exact contact areas between the components. Hence, the use of a continuous air gap is a simple solution that correctly captures the overall response of the system, including a right prediction of the high frequency slope of the curve. Above the spring-mass resonance the porous model behaves exactly like the poroelastic model, which strengthens

the statement that the thin air layer numerically decouples the skeleton phase from the plate. At the resonance itself, nevertheless, the use of the porous simplification leads to a large underestimation of the performance of the spring-mass system due to the missing damping coming from the solid phase.

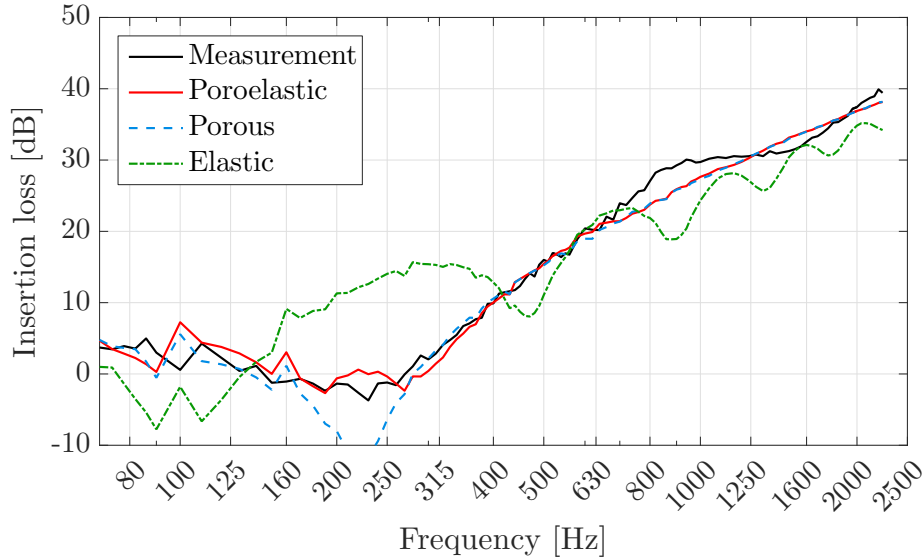


Figure 5.19: Comparison of the measured and simulated insertion loss for the spring-mass system E4 in the decoupled configuration with different material formulations.

Thus, for the decoupled setup of such a soft foam material, one may make use of the porous formulation if some accuracy in the predicted level at the spring-mass resonance is compromised. In return, a great saving in the computational resources with respect to the full poroelastic model can be achieved. The required time for all the considered poroelastic simulations with a total number of nodes between 800 thousand and one million is of the order of magnitude of one day. The calculations were run in parallel on four Intel® Xenon® processors E5-2680 v4 with a processor frequency of 2.40 GHz. Even if the number of nodes remains the same for both models, the poroelastic formulation has four degrees of freedom per node, whereas the porous model has only a single pressure degree of freedom. As a result, the utilization of the porous model results in a reduction of 65% in total computation time and of 55% in memory requirements. These percentages can actually be higher if a specific mesh is used for the foam component in the porous formulation. Since the velocity of the wave propagation is faster in the equivalent fluid, the corresponding wavelength is larger than the shortest wavelength in the poroelastic formulation (recall Figure 4.11), which allows to employ a coarser discretization without affecting the accuracy. By increasing the element size of the foam component from 7 mm to 10 mm a further reduction of 12% in computation time and 9% in memory usage is attained.

Once more, the simplification of the material behavior to its elastic constituent is not adequate for the prediction of the spring-mass resonance of a system with a soft middle layer. Apart from that, since the decoupled mounting condition reduces the energy transmitted through the structural phase, the amplitude of the high frequency resonances decreases in the experiment to a greater degree than in the elastic numerical model.

The introduction of the thin air gap has also an impact on the sensitivity of the model to the elastic material parameters. For example, the average deviation for a $\pm 10\%$ variation

of the elasticity modulus diminishes to 0.9%. The sensitivity to the poro-mechanical parameters, nonetheless, remains unaltered.

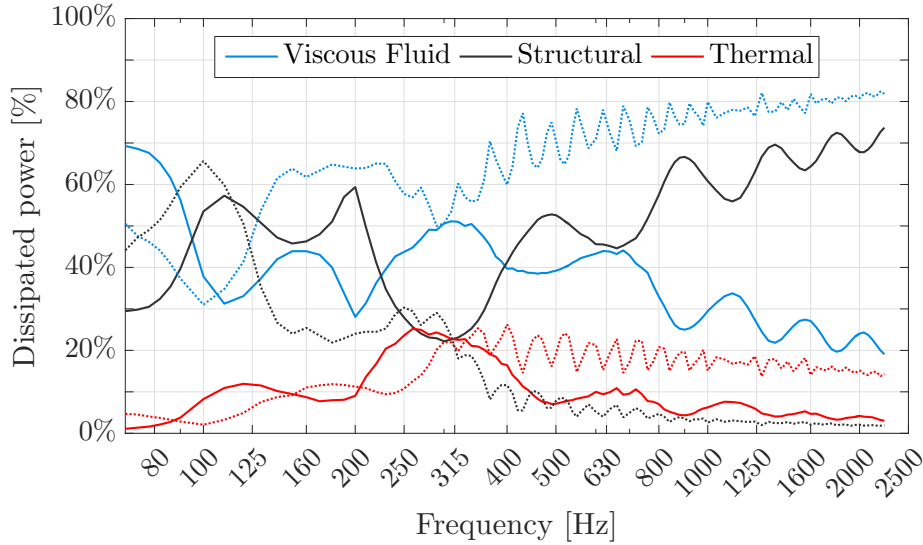


Figure 5.20: Percentage contribution to the total dissipated power of the main dissipation mechanisms inside the poroelastic layer of the system E4 in the coupled (solid lines) and decoupled (dashed lines) configurations.

It is possible to get a better understanding on the effect of the mounting conditions by studying the distribution of the energy dissipation inside of the poroelastic layer. To this end, the results obtained using the full poroelastic model with the constant material parameters from the compression method in the two mounting configurations are contrasted. The resolution by means of the Finite Element Method enables to retrieve the dissipated power inside the poroelastic component and to calculate separately the contribution of each five energy loss mechanisms according to the expressions in Eq. (4.17) to (4.22). Figure 5.20 shows the evolution over the frequency of the three main dissipation mechanisms, that is, the viscous losses in the fluid phase, the structural damping and the thermal effects, for the poroelastic model in both the coupled and decoupled setups. The values indicate the percentage contribution of each mechanism to the total losses.

We can distinguish opposite trends for the two mounting conditions. For the coupled configuration (solid lines) the structural damping is the main dissipation mechanism at almost every frequency. Conversely, the viscous losses in the fluid phase are responsible for most of the energy dissipation when the foam is decoupled (dashed lines). The thermal effects do not have a large contribution for the coupled setup, but they become the second greatest energy sink for the decoupled state above the spring-mass resonance, reaching values close to 20% of the total dissipated energy. As Eq. (4.20) and (4.22) indicate, the fluid viscous dissipation and the thermal losses are exclusively related to the fluid phase. This explains the good match between the poroelastic and the porous models beyond the spring-mass resonance area in the decoupled configuration. The other two dissipation mechanisms introduced in Section 4.1, namely the viscous losses in the structure and due to the solid-fluid coupling, have an overall negligible contribution with values below 3% for both mounting conditions in the frequency range of interest. The total dissipated power inside the foam component is of the same order of magnitude for the two configurations and has very similar curve progression over the frequency. This result was expected since

the two states have a comparable global performance as shown in the experimental results in Figure 5.11.

Stiff foam in decoupled state

For the investigated stiff materials with E/h larger than 1 kPa mm^{-1} only the decoupled state has been measured. For this reason, the model employed for the numerical calculations includes always a thin air gap between the steel plate and the foam. We now analyze the behavior of the spring-mass system B3 on the one-square meter flat plate. The foam layer in the numerical model is discretized with five layers in the thickness direction of 8 mm elements, which results in a total of 363636 quadratic nodes for the poroelastic component. We begin with a comparison of the three available material formulations employing the elastic foam parameters determined by the compression method. The corresponding insertion loss curves are displayed in Figure 5.21. One can observe that the poroelastic and porous models predict correctly the frequency of the spring-mass resonance, but the damping level at this point is not sufficient. Above this resonance, the slope of the insertion loss curve is too steep. In the frequency range between 400 Hz and 800 Hz the measured gradient is 9.1 dB/octave, whereas the simulated slope is 13.8 dB/octave. The poroelastic formulation also shows a thickness resonance in the range between 800 Hz and 1250 Hz that is not distinguishable in the measured data.

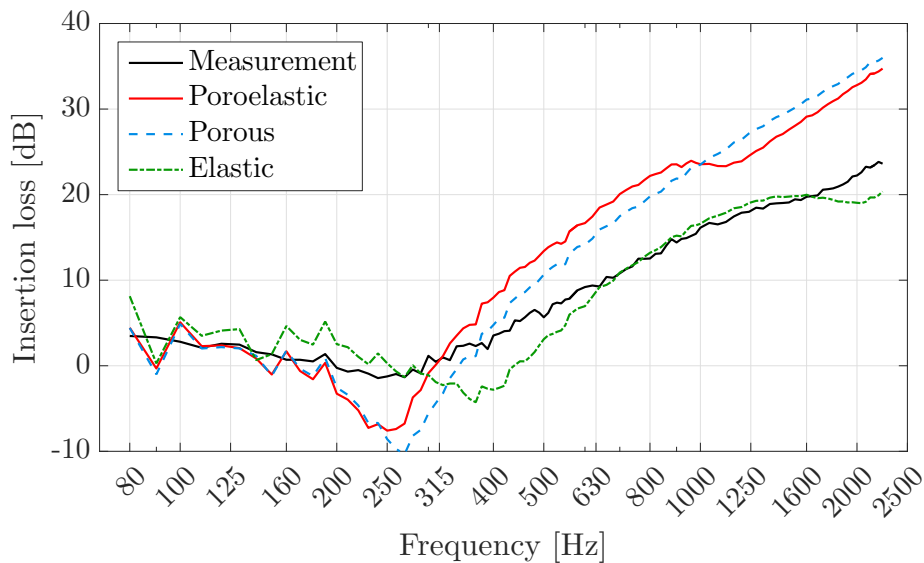


Figure 5.21: Comparison of the measured and simulated insertion loss for the spring-mass system B3 in the decoupled configuration with different material formulations.

The solid formulation, conversely, overestimates the spring-mass resonance frequency by one third octave band. This suggests that a softer elastic material should be represented in the numerical model in this frequency range to improve the match with the experiment. Moreover, the curve shape slightly differs from the measured insertion loss progression in the middle frequency range. Nevertheless, quite good correspondence is found in the frequency range between 630 Hz and 1600 Hz. On the whole, the behavior predicted by the elastic model provides a better approximation of the foam dynamics than the other two available formulations.

Analogously to the study for the spring-mass E4, we next evaluate the impact of each material parameter of the poroelastic formulation in the system response. The sensitivity of the total response to a variation of the Young's modulus of $\pm 10\%$ around its nominal value means an average deviation of 8 %, with maximum percent deviations of up to 26 % because of the shift in the spring-mass resonance frequency. These percentages are significantly larger than for the soft foams. The poro-mechanical parameters, oppositely, yield average deviations under 0.1%. The determinant influence of the solid phase in the dynamic behavior of the foam is also clearly identifiable in the contribution of the different dissipation mechanisms to the total power dissipation. As Figure 5.22 shows, the structural damping in the frame is the main cause for energy loss. Added to the viscous losses in the solid phase, the dissipation mechanisms associated to the frame represent more than 65% of the total dissipated power over the complete frequency range. The thermal dissipation becomes the second largest contribution in the middle frequencies reaching values up to 30%, whereas the viscous losses in the fluid phase and due to the solid-fluid interactions have a minor impact and only reach maximum contributions of 7% and 0.8%, respectively.

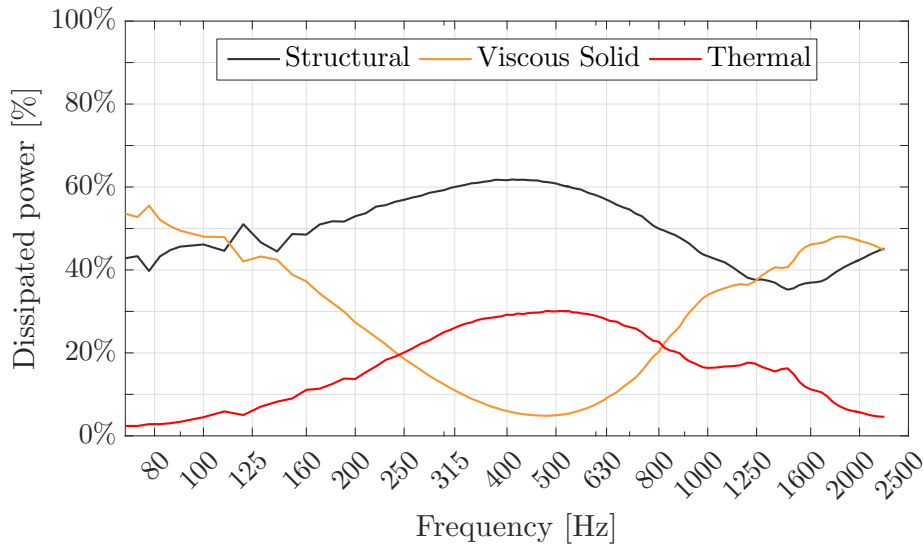


Figure 5.22: Percentage contribution to the total dissipated power inside the poroelastic layer of the main dissipation mechanisms inside the poroelastic layer of the system B3.

On that account, we continue to examine how the material parameters affect the system behavior for the elastic simplification. The results with three different sets of elastic parameters are displayed in Figure 5.23. The curve *Elastic (1)* has been calculated with the properties obtained from the compression method [88], whereas for the curve *Elastic (2)* the results from the resonance method [89] have been employed. The corresponding values are given in Table 4.1. As expected, the increase of the Young's modulus from *Elastic (1)* to *Elastic (2)* shifts the spring-mass resonance towards higher frequencies and worsens the match with the reference measurement in the low and middle frequency ranges. As the frequency increases, nevertheless, this model is better at predicting the high frequency slope. The experiment has a slope of 7.9 dB/octave in the frequency range between 600 Hz and 1600 Hz, the *Elastic (1)* model of 10.8 dB/octave and the *Elastic (2)* model of 8.9 dB/octave. All calculated results exhibit a performance drop above 1600 Hz

that correlates with a thickness resonance, but that phenomenon cannot be identified in the measurement.

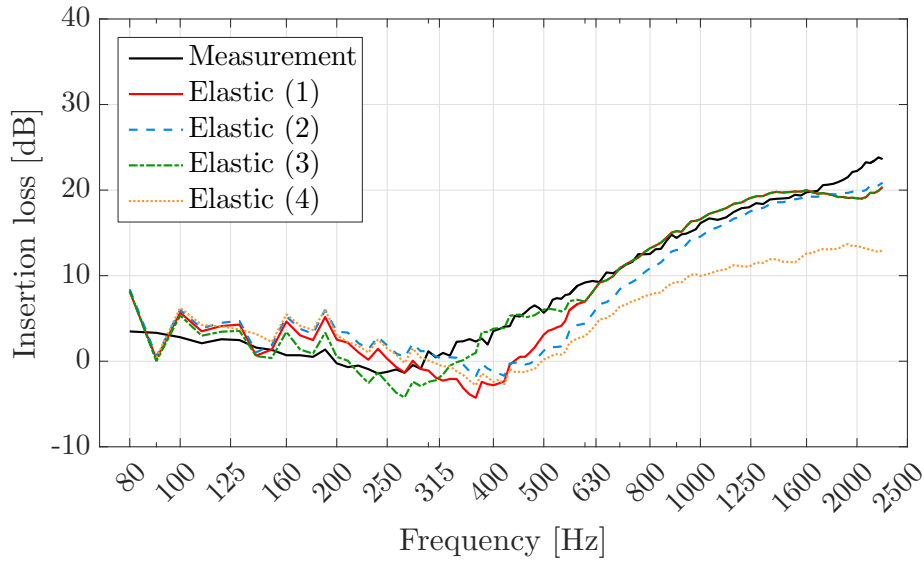


Figure 5.23: Comparison of the measured and simulated insertion loss for the spring-mass system B3 in the decoupled configuration with different elastic foam parameters for the elastic formulation: (1) compression method, (2) resonance method, (3) frequency-dependent elasticity modulus, (4) dynamic characterization.

In order to improve the curve fit around the spring-mass resonance, we define a frequency-dependent progression of the Young's modulus based on the comparison with the experimental curve. In the frequencies up to 400 Hz a softer elasticity modulus of 80 kPa is applied to shift the resonance frequency towards lower values, whereas above 800 Hz the elastic parameters from the compression method are used. The transition range is defined by a linear interpolation between these two values. The loss coefficient measured of the compression method is adopted and remains constant over the whole frequency range. The simulated results with this frequency-dependent Young's modulus are shown in the curve *Elastic (3)* of Figure 5.23. The correspondence with the experimental data is significantly enhanced, reducing the average deviation to 4.5%.

In a homologous way to the previous analysis with the system E4, the elastic coefficient determined by the dynamic method is tested for the spring-mass system B3. In this case, however, the material formulation employed for the foam layer is the elastic simplification. The values for E are given in Figure 4.9 in the previous chapter. The curve *Elastic (4)* in Figure 5.23 shows the response of the system when the dynamic values for the Young's modulus are employed. Anew, the elasticity values measured by the dynamic approach lead to a numerical model that is too stiff. The limitation of the spring-like behavior of middle layer restrains the insulation improvement of the double wall system, leading to a response close to that of a single wall with a nearly constant insertion loss value above 1 kHz.

5.5 Concluding remarks

In this chapter, the sound transmission through a spring-mass system attached to a steel plate has been investigated. This kind of system presents good insulation properties and,

therefore, finds wide application in the industry as passive acoustic treatment. During the product development process reliable tools for the prediction of the acoustic performance of these systems are required. The previous sections focused on the numerical modeling of the poroelastic middle layer of spring-mass systems. The mathematical description of such media is a special challenge because of the interaction of the fluid and the solid material phases. As numerous past works have pointed out, the dynamic behavior of a poroelastic medium does not only depend on the intrinsic material properties, but also on the coupling conditions to other components. In the current research, the influence of these factors on the choice of a proper material model were analyzed. Three different material formulations were compared, namely the full poroelastic model and the simplifications as a porous and as an elastic medium. The performance of each formulation and its suitability was determined by comparing the numerical results with experimental data obtained in a window test bench.

The first examined feature was the mounting condition between the foam layer and the basis steel plate. Using the insulation measurements as reference, we observed that the coupling condition between the basis steel plate and the spring-mass system had a remarkable influence on the total response of the aggregate. This is due to the fact that the coupling modifies the way the acoustic energy and, therefore, the energy dissipation are distributed between the two phases of the poroelastic layer. In order to include the effect of the decoupling into the numerical setup, a thin air gap was introduced between the steel plate and the foam layer.

The study showed that the behavior of the systems could be classified into two groups according to the foam elastic properties. For a relatively soft material such as the foam in the spring-mass system E4, we concluded that the use of the complete poroelastic formulation was necessary if the foam layer was fully coupled to the vibrating steel plate. To improve the match with the resonances at higher frequencies, a larger Young's modulus than the quasi-static value had to be used. In the decoupled setup, however, it was possible to make use of either a poroelastic or a porous model, since the solid phase was only noticeably excited in the range around the spring-mass resonance frequency. The porous simplification led to some overestimation of the total radiated power in that frequency range, but it also allowed to considerably save calculation resources in terms of memory usage and computational time. In turn, in the application for a stiffer poroelastic material like sample B3 the structural phase became dominant, even in the decoupled state. Under these conditions, the description of the foam as an elastic solid gave the best approximation of the overall system behavior.

For both kinds of foams the sensitivity to changes in the poro-mechanical parameters was low. In the example of the spring-mass system E4 it was examined the possibility to replace of the measured poro-mechanical properties by an averaged standard data set. The insulation performance of the system remained nearly unaltered. Such substitution exhibited therefore a great potential to reduce the characterization effort related to poroelastic media. Conversely, the overall system response was more sensitive to variations in the elastic parameters. Particularly, specific modifications of the complex Young's modulus value resulted in a better fit with the experimental results.

A problem arose, however, in the identification of proper values for the elasticity properties in the frequency range of interest. On the one hand, we observed that different characterization methods did not provide the same elastic parameters. Moreover, there was no definite conclusion on which methodology would be better suited for a given material. On the other hand, the dynamics of the aggregate suggested the necessity of frequency-dependent

elastic properties, which are not usually available. The dynamic characterization method introduced in Section 4.1 could deliver such frequency-dependent parameters. Nevertheless, the application of the resulting moduli to the complete spring-mass system pointed to an overestimation of the modeled material stiffness that dampened the spring-like response of the foam. Hence, further refinements of the material characterization techniques are needed to improve the quality of the predictions.

Another critical aspect of the applied numerical approach was the associated high computational effort, especially regarding the long calculation times. Due to the frequency non-linearity introduced by the coefficients in the poroelasticity equations (recall Eq. (4.1) and (4.2)) classical reduction techniques cannot be applied. Several alternatives are found to increase the performance of the resolution. As mentioned in Section 4.2, the use of hierarchical elements largely reduces the number of degrees of freedom and, thus, the size of the matrix system to be solved [135]. Nonetheless, hierarchical elements for poroelastic components are not yet available in commercial solver software. Other possibility is the application of the Transfer Matrix Method to describe multi-layered structures [150]. However, even with the corrections for finite size panels and to include non-locally reacting effects [118], its utilization remains restricted to flat structures, which is a major disadvantage compared to the geometrical flexibility of the Finite Element Method. Alternative options to enhance the numerical efficiency of the Finite Element implementation can be found in substructuring techniques like the Patch Transfer Function [129] or especial model order reduction (MOR) methods as the parametric MOR proposed in [131]. Nevertheless, those procedures are currently in development and their application to industrial applications is still an open question.

Chapter 6

Combination of experimental and numerical results in a hybrid approach

In this chapter the main characteristics of the hybrid approach are presented. Section 6.1 begins with an introduction on the panel contribution analysis (PCA), a methodology that identifies the relative contribution of different surfaces to the sound pressure level at a given point. The PCA serves as the basis of the hybrid approach shortly introduced before in Section 2.3. The mathematical framework underlying the hybrid methodology is outlined in Section 6.2. Essential for the method is the concept of the reciprocally determined transfer functions, that is, the transfer functions obtained when the source and receiver positions are interchanged. In Section 6.3 several numerical models are employed to verify the hybrid technique in a full simulative environment and to gain some insight on the requirements for the hybridization. Finally, Section 6.4 describes the measurement procedure employed for the reciprocal determination of the transfer functions. The difficulties for the later integration of the experimental information with the numerical results are also highlighted here.

6.1 Panel contribution analysis

To track down the energy flow from a vibroacoustic source to a given receiving position through a set of structure-borne and airborne pathways the transfer path analysis (TPA) is commonly applied [151]. The complete vibroacoustic system is described as a source-path-receiver model. The objective of this analysis is to assess the relative contribution of the different paths to the observation point in order to locate the dominant ones. That way it is possible to identify weak spots in the transmission chain and to adopt the proper measures to alleviate or eliminate these issues. Additionally, the impact of modifications in the transmission paths can also be inspected in this manner [152].

The panel contribution analysis is a special application of the airborne TPA in which a group of pathways are summarized into surfaces or panels [153]. In the automotive engineering practice the focus is usually set on the evaluation of the contribution of the defined areas in the interior of the vehicle to one or more reception points inside the passenger cabin in an operational state. A standard observation position is the driver's ear. Both the noise resulting from the panel radiation and from the acoustic leaks are considered. Two different procedures can be employed to determine the panel contributions. In the first one, known as the window method, all the surfaces inside the cabin are first covered with highly insulating material. Next, each partial area is sequentially uncovered and the

sound pressure level at the point of interest is measured. Finally, the solution of an equation system delivers the contribution of each panel. This approach is quite laborious since the complete interior of the vehicle needs to be encapsulated. Furthermore, the massive insulating material added strongly modifies the dynamic behavior of the structure and the absorption properties of the passenger cabin [154].

As alternative an array-based method can be employed [155, 156]. In that case, it is essential that the sensors forming the array are capable to measure the acoustic pressure and velocity simultaneously. The velocity determination can be conducted either indirectly with two microphones, or directly with a special probe like the Microflown introduced in Section 5.3. The array-based process consists of two steps. The first one is called the operational state (Figure 6.1). Here, the vehicle runs in the operational condition of interest and the whole internal surface is scanned with the array. During the second step the airborne transfer functions (TF) from the scanned surface areas to the receiver are calculated (Figure 6.2). Instead of utilizing a costly direct technique to obtain the cabin TF, it is advisable to determine the transfer functions making use of the reciprocity principle. More details on this principle and its application are indicated in the following Sections 6.2 and 6.4. The combination of the operational and the reciprocal results delivers a reconstruction of the sound pressure level at the observation point and the contribution of each panel. This PCA approach exhibits the major advantage that the vibroacoustic system is not altered in the course of the measurement.

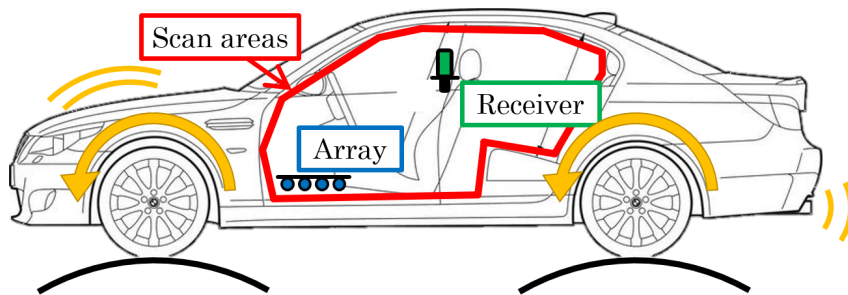


Figure 6.1: Measurement in operational state in a dynamic roller test bench. Different noise sources (engine, tires and exhaust system) are marked in yellow.

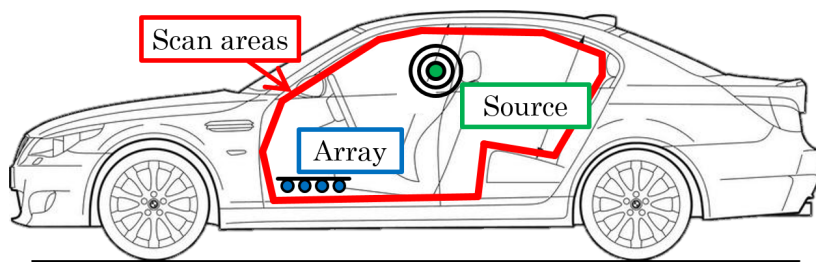


Figure 6.2: Measurement of the cabin transfer functions by means of a reciprocal method.

In the current NVH development process an experimental array-based PCA is particularly employed for troubleshooting and identification of weak spots. The reciprocal determination of the transfer functions inside the cabin needs to be conducted just once for a given vehicle, whereas the operational measurements are carried out for each driving state of interest. These include critical driving states with constant velocity as well as at constant acceleration rates. The operational information can be obtained during road tests [157],

but it is preferred to place the vehicle in a dynamic roller test bench in order to ensure a higher reproducibility of the excitation conditions [158]. An advantageous characteristic from the introduced experimental PCA is that the absorption and reflection properties in the interior of the vehicle are realistically captured in the cabin transfer functions. However, the current process presents the drawback that no information is available about the vibroacoustic system on the excitation side up to the scanned surfaces, but it is regarded as a black box (Figure 6.3). Consequently, improvement and optimization measures are difficult to define.

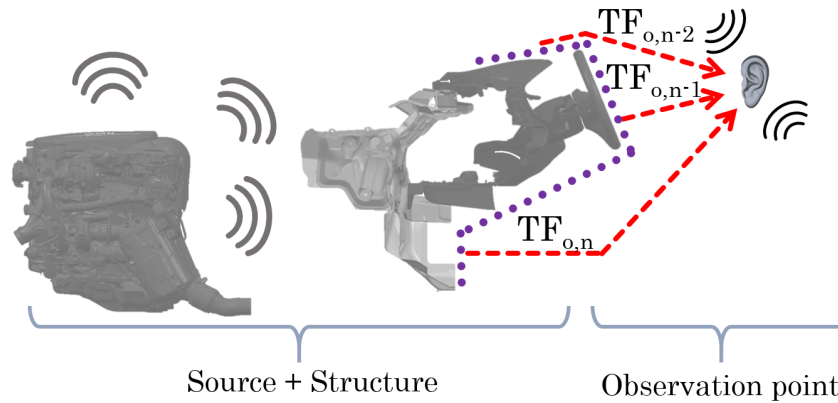


Figure 6.3: Schematic representation of the current panel contribution analysis applied to the vehicle front end.

To overcome that disadvantage we propose a hybrid approach. It combines the numerical description of the structural components with the experimental transfer functions, as Figure 2.4 in Chapter 2 illustrates for the vehicle front end area. The sound transmission chain is divided into its three substantial components, namely, the noise source, the main structural components and the observation point. The link between the components is included by means of several input and output transfer functions TF_i , TF_o . The main benefit is that every component can be independently evaluated by the most adequate method, experimentally or numerically, based on the data at disposal at a given development stage. The pressure distribution generated by the excitation, for instance from the engine radiation, can either be measured at the engine test bench or be the result of a simulation. This information is then mapped onto the interface between the excitation domain and the structural component. By means of a numerical model the propagation of energy through the system is calculated. Lastly, the utilization of the reciprocally measured transfer functions enables the projection of the output of the structural component on the observation point.

This hybrid method allows for the characterization of each one of the three subsystems of the transmission chain separately from the other two components. This independence is an approximation of the real behavior since global interactions may be present, especially at lower frequencies as is the case with the exhaust outlet excitation [159]. The detail level of each component description is updated in the course of the development process as soon as new and more accurate data are available. The comprehensive representation of the excitation distribution on the firewall together with the measured cabin transfer functions allow to obtain robust acoustic predictions taking into consideration the real operational environment of the structural component. As a result, the potential of both experimental and numerical methods can be exploited. On the one hand, the exhaustive inspection

of the structural subsystems by means of a numerical model enables to gain a deeper understanding of the transmission phenomena. On the other hand, the integration with the passenger inner cavity transfer functions automatically includes the vehicle interior absorption and reflection properties and weights the response of the structure to correlate with the passenger's point of view.

6.2 Mathematical description of the hybrid method

In this section the mathematical framework underlying the array-based panel contribution analysis is explained. The objective is to solve the Helmholtz equation for a harmonic time dependence $\exp(j\omega t)$:

$$\nabla^2 \hat{p} + k^2 \hat{p} = 0 \quad (6.1)$$

Using Green's second identity [160] this equation can be represented in integral form. The pressure \hat{p} at an observation point \mathbf{x}_0 is then obtained as the integral over the radiating surface S [161]:

$$\hat{p}(\mathbf{x}_0) = \int_S \left[\hat{p}(\mathbf{x}) \frac{\partial G(\mathbf{x}_0, \mathbf{x})}{\partial n} - G(\mathbf{x}_0, \mathbf{x}) \frac{\partial \hat{p}(\mathbf{x})}{\partial n} \right] dS(\mathbf{x}) \quad (6.2)$$

where $G(\mathbf{x}_0, \mathbf{x})$ indicates the Green's function between the observation point \mathbf{x}_0 and a point \mathbf{x} on the integration surface. The nomenclature employed in the application of these expressions to the passenger cabin is specified in Figure 6.4. The gradient of the pressure on the surface can be rewritten in terms of the normal velocity \hat{v}_n according to Eq. (3.6) as:

$$\frac{\partial \hat{p}(\mathbf{x})}{\partial n} = -j\rho_0\omega\hat{v}_n(\mathbf{x}) \quad (6.3)$$

giving the rewritten Helmholtz integral equation:

$$\hat{p}(\mathbf{x}_0) = \int_S \left[\hat{p}(\mathbf{x}) \frac{\partial G(\mathbf{x}_0, \mathbf{x})}{\partial n} + G(\mathbf{x}_0, \mathbf{x}) j\rho_0\omega\hat{v}_n(\mathbf{x}) \right] dS(\mathbf{x}) \quad (6.4)$$

The Green's function characterizes the transfer properties between the two points \mathbf{x}_0 and \mathbf{x} . It relates the sound pressure in the field to the normal force per unit length $\hat{F}_n(\mathbf{x})$ acting on the differential surface δS :

$$G(\mathbf{x}_0, \mathbf{x}) = \frac{\hat{p}(\mathbf{x}_0)}{\hat{F}_n(\mathbf{x})} = \frac{\hat{p}(\mathbf{x}_0)}{\rho_0\hat{a}_n(\mathbf{x})\delta S} = \frac{\hat{p}(\mathbf{x}_0)}{j\rho_0\omega\hat{v}_n(\mathbf{x})\delta S} \quad (6.5)$$

where \hat{a}_n is the excitation normal acceleration. Eq. (6.5) can be reformulated in terms of the transfer function for the pressure TF_p , which links the sound pressure to the excitation normal velocity:

$$\rho_0 j\omega G(\mathbf{x}_0, \mathbf{x}) = \frac{\hat{p}(\mathbf{x}_0)}{\hat{v}_n(\mathbf{x})\delta S} = \text{TF}_p(\mathbf{x}_0, \mathbf{x}) \quad (6.6)$$

Analogously, the differentiation of the Green's function results in:

$$\frac{\partial G(\mathbf{x}_0, \mathbf{x})}{\partial n} = \frac{\partial \hat{p}(\mathbf{x}_0)/\partial n}{\rho_0\hat{a}_n(\mathbf{x})\delta S} = \frac{-j\rho_0\omega\hat{v}_n(\mathbf{x}_0)}{j\rho_0\omega\hat{v}_n(\mathbf{x})\delta S} = \text{TF}_v(\mathbf{x}_0, \mathbf{x}) \quad (6.7)$$

where TF_v is the transfer function for the acoustic velocity. Introducing Eq. (6.6) and (6.7) in Eq. (6.4) we obtain:

$$\hat{p}(\mathbf{x}_0) = \int_S [\hat{p}(\mathbf{x}) \text{TF}_v(\mathbf{x}_0, \mathbf{x}) + \hat{v}_n(\mathbf{x}) \text{TF}_p(\mathbf{x}_0, \mathbf{x})] dS(\mathbf{x}) \quad (6.8)$$

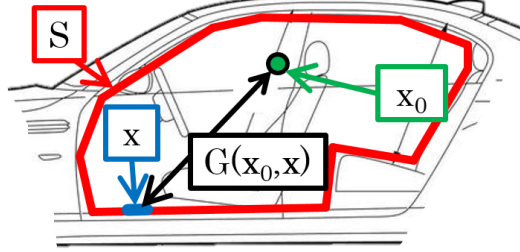


Figure 6.4: Nomenclature employed for the definition of the points and surfaces in the panel contribution analysis applied to the passenger cabin.

The direct calculation of the transfer functions is a laborious process. A known excitation needs to be applied at each point \mathbf{x} of the vibrating surface, and the pressure and velocity responses are measured at the reception point \mathbf{x}_0 . However, the transfer functions can be easily defined making use of the reciprocity principle [162]. Reciprocity in this context means that the response of a linear vibroacoustic system to a disturbance is invariant if the points of excitation and observation are exchanged. In line with this principle, a known acoustic point source with volume velocity \hat{Q} is placed at the observation point \mathbf{x}_0 , and the pressure and velocity responses at the surface position \mathbf{x} are measured. Figure 6.5 exemplarily displays the direct and reciprocal equivalent systems for the derivation of the pressure transfer function TF_p . The mathematical relations for the reciprocal calculation of the transfer functions are given in Eq. (6.9) and (6.10). The superscript R specifies that the quantity is calculated from a reciprocal configuration.

$$\text{TF}_p(\mathbf{x}_0, \mathbf{x}) = \frac{\hat{p}(\mathbf{x}_0)}{\hat{v}_n(\mathbf{x})\delta S} = \frac{\hat{p}^R(\mathbf{x})}{\hat{Q}(\mathbf{x}_0)} \quad (6.9)$$

$$\text{TF}_v(\mathbf{x}_0, \mathbf{x}) = \frac{\hat{v}_n(\mathbf{x}_0)}{\hat{v}_n(\mathbf{x})\delta S} = \frac{\hat{v}_n^R(\mathbf{x})}{\hat{Q}(\mathbf{x}_0)} \quad (6.10)$$

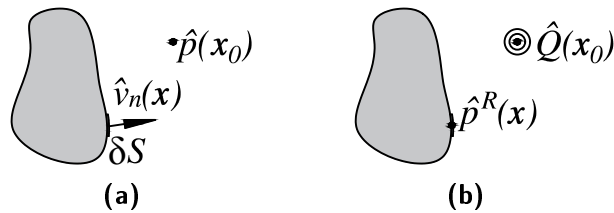


Figure 6.5: Application of the reciprocity principle to calculate the Green's function: (a) direct state, (b) equivalent reciprocal state (adapted from [162]).

For real applications, the scan process on the inner surface is not continuous, but takes place at a discrete number of points N . Because of this, the integral in Eq. 6.8 is approximated by a summation as:

$$\hat{p}(\mathbf{x}_0) \approx \sum_{i=1}^N \left[\hat{p}(\mathbf{x}_i) \frac{\hat{v}_n^R(\mathbf{x}_i)}{\hat{Q}(\mathbf{x}_0)} + \hat{v}_n(\mathbf{x}_i) \frac{\hat{p}^R(\mathbf{x}_i)}{\hat{Q}(\mathbf{x}_0)} \right] \Delta S_i \quad (6.11)$$

where the index i refers to a scanned point with an associated partial surface ΔS_i . The transfer functions reciprocally calculated serve as weighting factors of the vibroacoustic response at each point of the surface S with respect to the observation point \mathbf{x}_0 .

Recalling the experimental panel contribution analysis exposed in the previous Section 6.1, the measurement of the quantities $\hat{p}(\mathbf{x}_i)$ and $\hat{v}_n(\mathbf{x}_i)$ occurs during the operational step at the desired working state, whereas the pressure $\hat{p}^R(\mathbf{x}_i)$ and the normal velocity $\hat{v}_n^R(\mathbf{x}_i)$ are acquired in the course of the reciprocal step. In the pursued hybrid approach the operational information is provided by the numerical model, while the reciprocal data remains the result of measurements. As aforementioned, the major advantage of the utilization of experimental transfer functions is that the absorption and reflection properties of the cabin are automatically included. This way, the explicit modeling of the vehicle cabin is avoided, thus reducing the size of the problem to be solved.

6.3 Numerical verification

Before proceeding with the hybridization some preliminary analyses with the help of numerical models have been conducted. Those tests served to verify the algorithms that are later used for the hybrid integration as well as to identify the limitations and requirements of the approach.

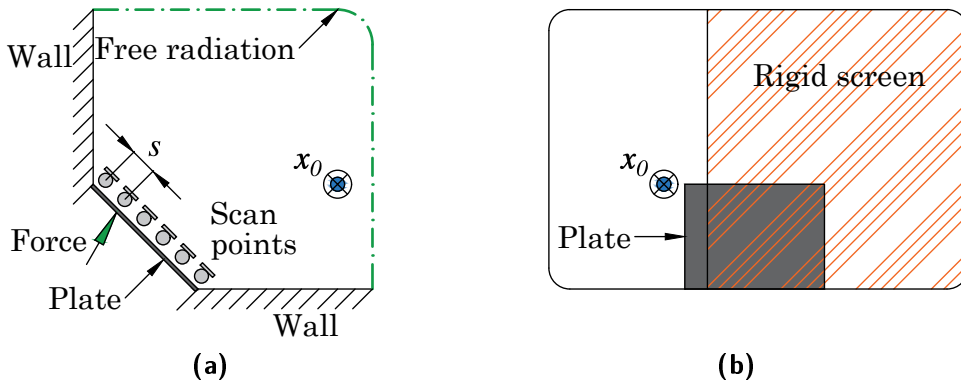


Figure 6.6: Two-dimensional representation of the model employed for the numerical verification of the adapted panel contribution analysis: (a) side view, (b) front view, the area covered by rigid screen is marked in orange.

To that end, different Finite Element models with increasing geometrical complexity were prepared. The procedure is demonstrated in this section using the example setup displayed in Figure 6.6. A 0.76 mm thick steel plate with an inclination angle of 45° is excited by a point force of magnitude $[1;0;2]$ N. The material properties are indicated in Table 4.3. The opposite face of the plate is connected to a fluid medium into which it radiates. Inside the fluid domain an observation point in the position \mathbf{x}_0 has been defined. The objective of the

test is to reconstruct the sound pressure level (SPL) at the observation point according to Eq. (6.11). For that, the simulation of the operational and the reciprocal state are required. A microphone located at the receiver point for the operational configuration provides the reference SPL. The excitation for the operational setup is the point force, whereas to model the reciprocal configuration a volume velocity source of strength $1 \text{ m}^3 \text{ s}^{-1}$ is located at the receiver position \mathbf{x}_0 . Above the radiating panel an auxiliary grid is defined to record the pressure and velocity results during both configurations in an analogous way to the PU-probes array applied in the experiments. The spacing between two scan points of the auxiliary coupling grid is designated as s .

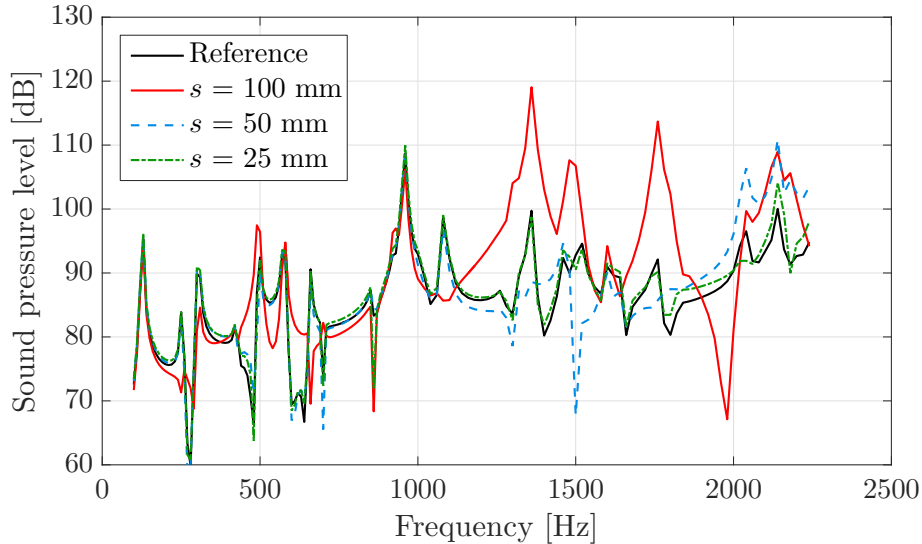


Figure 6.7: Comparison of the simulated and the reconstructed sound pressure level for free radiation with different discretizations.

First, the receiving fluid domain is unbounded, that is, the vibroacoustic waves radiate freely. This is achieved by the numerical extension of the finite fluid domain with the help of infinite elements on its outer layer (green line in Figure 6.6a). An important feature is to determine the minimum spacing s necessary to properly reconstruct the pressure level. The study by Ouisse *et al.* in [128] indicated that the auxiliary coupling area should be discretized with a minimum of a half-wavelength $\lambda/2$ size. Figure 6.7 displays the reconstructed SPL using different values for the spacing s , namely, 100 mm, 50 mm and 25 mm. In line with the aforementioned $\lambda/2$ criterion the needed discretization at the maximum frequency 2.24 kHz would be 77 mm. However, we can observe that the 100 mm discretization already diverges from the reference at approximately 1.1 kHz, which corresponds with a $\lambda/3$ criterion. Some deviations can also be noticed for the spacing with 50 mm at the high frequency range. Nonetheless, the differences with respect to the 25 mm reconstruction remain limited and the overall trends are correctly met. Later investigations with the experimental setup did not show any deviations between the two fine discretizations in the frequency range of interest. Therefore, a spacing of $s = 50 \text{ mm}$ is selected in the next chapter for the integration with the experimental results.

The next analysis should verify the impact of boundaries applied on the receiving fluid domain. Figure 6.6b illustrates the second configuration in which on nearly two thirds of the outer fluid surface a rigid screen restricts the free radiation. The reconstruction of the sound pressure level works satisfactorily and the same conclusions on the required discretization spacing as before are drawn. Another interesting aspect is the possibility

to merge the results from the operational simulation in the free radiation setup with the reciprocal transfer functions when the rigid screen is present. This combination is equivalent to the assumption that the modifications in the receiver fluid only have a marginal impact on the dynamic behavior of the structural system. In Figure 6.8 the calculated SPL of the covered state (*Screen-Screen*) is compared to the reconstruction obtained by the combination of uncovered operational and covered reciprocal states (*Free-Screen*). The agreement between the two curves and the correlation with the reference curve confirm that such merging of free radiation and restricted setup provides the desired accuracy in the prediction of the sound pressure level.

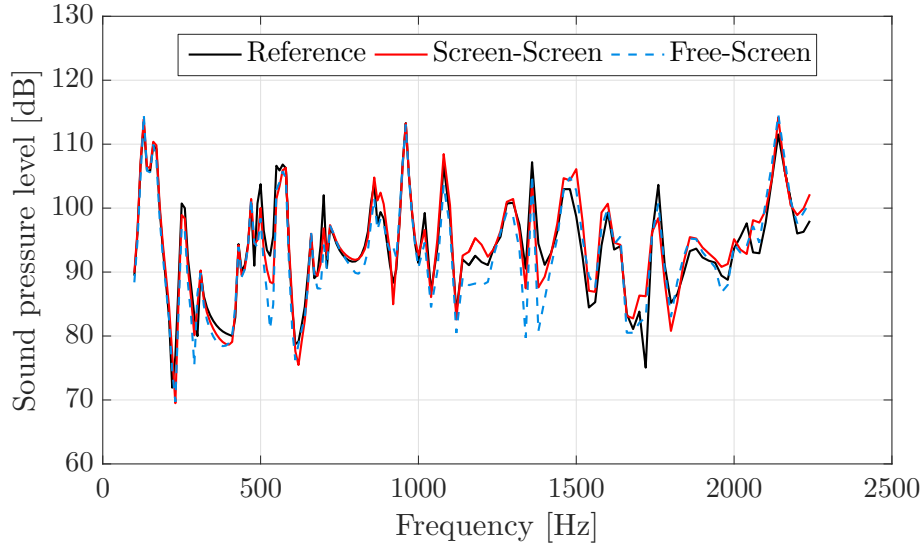


Figure 6.8: Comparison of the simulated and the reconstructed sound pressure level for the configuration with a rigid screen and a spacing of $s = 25$ mm.

This mixed combination can be implemented further on in the integration of numerical and experimental results. According to the previous results, the calculation of the operational state by means of a simulation can be conducted in a conventional free radiation setup. Later, the integration with the reciprocal transfer functions determined in the actual application environment allows for the automatic inclusion of the properties of the real boundary conditions.

6.4 Reciprocal measurement of the transfer functions

The present section focuses on the measurement procedure for the determination of the transfer functions inside the passenger cabin. First, the main steps are outlined, highlighting the particularities of the reciprocal method. After that, some especial considerations for the later integration with the numerical results are indicated.

Since the experimental approach is based on the reciprocity principle, the source is located at the receiver point for the measurement of the transfer functions between the vibrating surfaces and the point of interest. As excitation we have employed the middle and high frequency volume source from LMS Siemens. This is a monopole volume acceleration source that allows to measure acoustic transfer functions in the frequency range from 150 Hz to 10 kHz [163]. The source is equipped with an internal reference sensor that registers the volume acceleration $\dot{Q} = dQ/dt$ during the measurement. In order to

of the object. In Figure 6.10 the array positions are marked by the thick lines, whereas the fine lines delimit the area associated to each PU probe. For the top and bottom surfaces of the object six array positions were defined, as illustrated in Figure 6.11.

20	19	18	17	16	40	39	38	37	36					
15	14	13	12	11	35	34	33	32	31					
10	9	8	7	6	30	29	28	27	26					
5	4	3	2	1	25	24	23	22	21					
16	17	18	19	20	21	22	23	24	25	26	27	28	29	30
1	2	3	4	5	6	7	8	9	10	11	12	13	14	15

Figure 6.11: Numbering sequence employed for the positions of the PU-probes on the top and bottom surfaces: in blue for the measurement, in green for the numerical model.

A decisive factor to make possible the integration of the results is that these array positions must be coincident with the locations used in the operational state. Additionally, a coherent numbering sequence of the scan points needs to be defined. The numbers assigned during the experiments are derived from the measurement sequence and every array position has an internal numbering up to 20. Conversely, the grid in the simulation follows a numbering sequence in rows. In Figures 6.10 and 6.11 the two numbering approaches are indicated for a few probe positions. Therefore, previously to the integration step in the hybrid method, a careful conversion of one numbering system to the other will be needed.

In the experimental procedure each array position is measured during 10 seconds and the results are later averaged. Including the time involved for the repositioning of the PU-probes array, one minute for each partial surface is necessary. In total, approximately 20 minutes are necessary to complete the scanning operation. Lastly, one must take into consideration that the measured quantities are complex numbers. Since the measurement is not conducted at once, but sequentially one array position after the other, a channel in a static location is required in order to have a constant reference for phase shift. For the evaluation of the quotients $p^R(\mathbf{x}_i)/Q(\mathbf{x}_0)$ and $v_n^R(\mathbf{x}_i)/Q(\mathbf{x}_0)$ in Eq. (6.11) the signal from the acoustic source is employed as phase reference. This issue is not present in the simulation results since all quantities are retrieved simultaneously and already have the same phase reference.

Chapter 7

Simplified model of the vehicle front end

The prediction of the sound transmission through a system of higher complexity is the objective of the current chapter. The investigations shown below aim to apply all the work and conclusions discussed in the previous chapters to an environment closer to the real front end of a vehicle. A simplified model of the firewall with instrument panel is first introduced in Section 7.1. After that, the results calculated with the numerical model are contrasted to the data measured in a window test bench. Because of the interaction of the sound package with a closed air volume, other noise reduction properties of the poroelastic noise control treatments like absorption can be inspected. Consequently, in this chapter not only the acoustic performance of a two-layered spring-mass system has been inspected, but also one-layered absorbers and three-layered spring-mass systems with absorber have also been examined in Section 7.2. Some of the results shown here were partially published in [164]. Next, in Section 7.3 this simplified configuration is employed to put the hybrid approach into practice. The real excitation of the experiments and the transfer functions inside the reception domain are combined with the simulation model of the front section as defined in the hybrid method. Again, the reference data was obtained from measurements of the complete system in the window test bench. At the end of the chapter the main findings are summarized with special emphasis on the potential and limitations of the proposed hybrid approach.

7.1 Description of the simplified model

The object defined for the analyses is a simplified model in which all the essential components of the front section of a car are present. This mock-up has a hexahedral shape with the dimensions $0.85\text{ m} \times 0.4\text{ m} \times 0.5\text{ m}$, as Figure 7.1a illustrates. The two smaller lateral walls (brown) are structurally and acoustically rigid and represent the side walls of the car. They build the support on which a three-faced cover made of a thermoplastic Plexiglas[®] is fixed. The material for these surfaces is 1.5 mm thick and has been selected to match the properties of the real vehicle dashboard in terms of mass density per unit area. On the remaining large surface there is an opening of size $0.85\text{ m} \times 0.43\text{ m}$ in which we reproduce the firewall with a 0.75 mm thick steel plate (grey), a typical thickness in the vehicle construction. All six faces together enclose an air cavity. The system is installed in a window test bench in such a way that the steel plate is located in the partition wall between the two rooms (see Figure 7.2). The plastic cover and the air cavity are completely inside the semi-anechoic room. For verification purposes a configuration without the steel plate has also been considered and is further on referred to as open

state. Figures 7.2a and 7.2b display the system installed in the window test bench in the open and closed configurations, respectively.

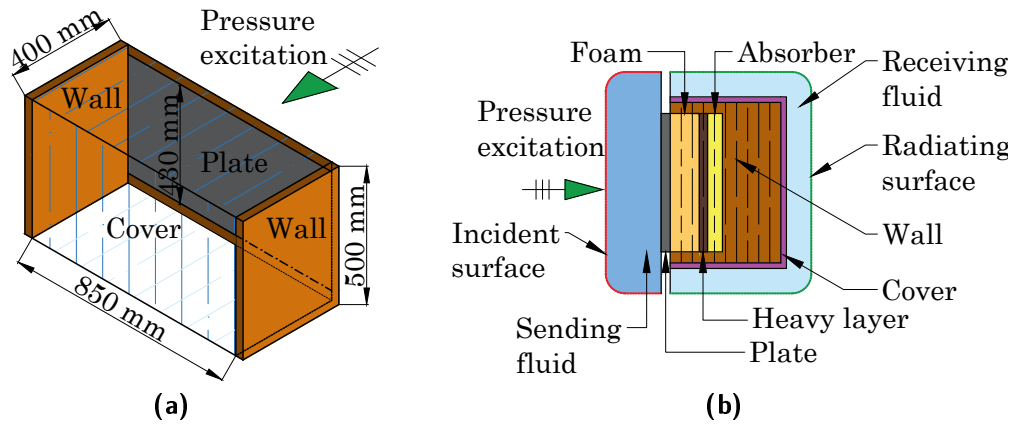


Figure 7.1: Schematic representation of the simplified front car end model: (a) isometric view with dimensions, (b) side view of the numerical model with a three-layered acoustic package and including the sending and receiving fluids. Note that the thicknesses are not scaled.

A pressure field is the excitation that acts upon the system, either applied directly on the steel plate or on the opening surface of the cavity, depending on the configuration setup. The acoustic energy propagates inside the air cavity and induces vibrations in the plastic cover, which lastly radiates into a semi-free field environment. The total radiated sound power through the cover is retrieved. During the measurements the three outer surfaces are scanned in the near field with the help of the PU-probes array according to the procedure explained in Section 5.3. The pressure and normal velocities are recorded at a total of 400 points, and the radiated power can be calculated as specified in Eq. (5.5). In the numerical models this quantity is obtained on the outer surface of the receiving fluid (marked in green in Figure 7.1b).

For the simulation model we have used two different excitation definitions depending on the application. Firstly, for the comparison of the simulated and measured states in Section 7.2 we employ an incident diffuse field homologous to the one utilized before in Chapters 3 and 5. For the representation of the open state, nevertheless, it is no longer possible to define the incident pressure field directly on the surface of the enclosed fluid, but it requires a semi-infinite fluid. For this reason the explicit modeling of the sending fluid volume is required, as Figure 7.1b shows. Analogously to the description of the receiving fluid, the sending fluid is formed by a finite domain with infinite elements on its outermost layer (marked in red). On this outer surface of the finite sending fluid the diffuse excitation can be specified. The results included in that section are evaluated in terms of the insertion loss (recall Eq. (5.1)), so it is not decisive to employ the same excitation level in the simulations as in the measurements since the system is working in the linear regime. However, the pressure field must remain constant for all the examined states. To facilitate the comparability of the open and closed configurations, the same sending fluid is used when the steel plate is present.

Secondly, in Section 7.3 we proceed with the implementation of the hybrid approach. The required output of the numerical model are the pressure and normal velocity fields on the surfaces of the plastic cover, which are later combined with the reciprocal transfer

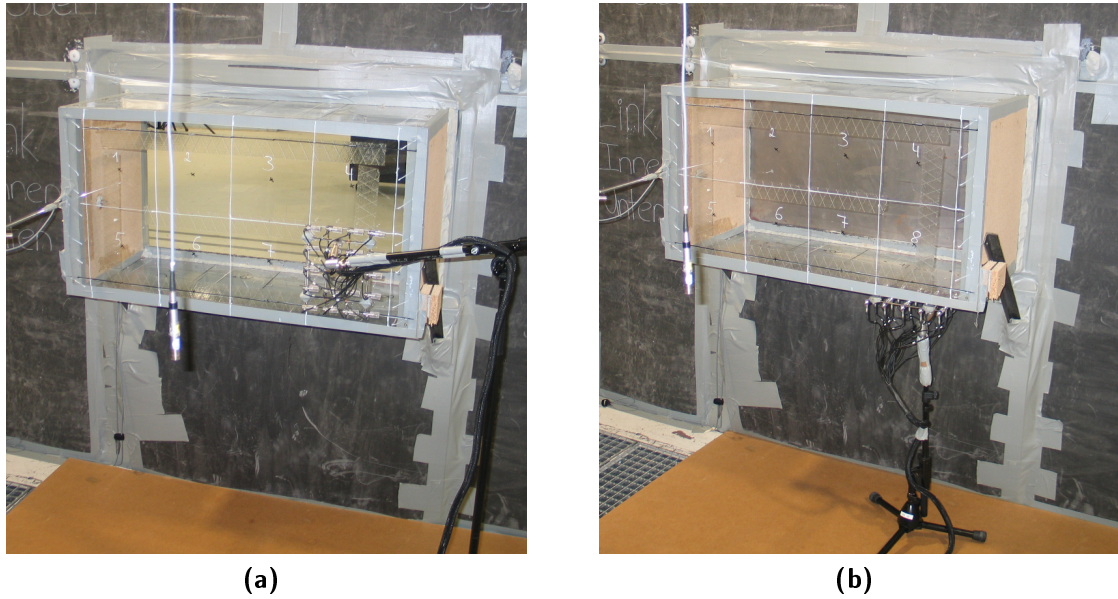


Figure 7.2: The simplified vehicle front end installed in the window test bench for the experimental investigations: (a) open state, (b) closed state.

functions. Therefore, here the fact that the distribution and the level of the excitation are exactly the same as in the measurement plays an important role. Only this way it can be ensured that the magnitude of the responses matches. To that end, the real incident pressure acting on the steel plate was first scanned on the reverberation chamber side with the PU-probes array. Then it is applied on the input surface of the plate in the numerical model as detailed later in Section 7.3.

Component	Element type	Order	Max. size	Nr. nodes
Plate	Solid shell	2 nd	6 mm	73150
Heavy layer	Solid shell	2 nd	6 mm	73150
Cover	Solid shell	2 nd	6 mm	218014
Air cavity	Hexa/Tetrahedral	1 st	17 mm	240370
Sending fluid	Hexa/Tetrahedral	1 st	17 mm	47873
Receiving fluid	Hexa/Tetrahedral	1 st	17 mm	143443

Table 7.1: Details of the numerical model for the cavity configuration.

The Finite Element model for the numerical investigations includes all the structural components introduced in the experimental setup (see Figure 7.1b). The steel plate and the plastic cover are modeled with solid shell elements. The displacements of the nodes on the outer edges of the structural parts are restricted in the direction of the thickness to represent the simply supported boundary conditions of the test bench. Inside the structure, the enclosed air cavity is discretized with hexahedral and tetrahedral elements that have a single pressure degree of freedom per node. The four large faces of the fluid cavity are directly coupled to the plate and the plastic cover to enable the energy transmission, while on the two rigid side walls a zero normal velocity is imposed to ensure

the perfect reflection of the acoustic waves. Regarding the acoustic treatments, one-layered (foam), two-layered (foam and heavy layer) and three-layered (foam, heavy layer and absorber) systems are investigated. The heavy layer is discretized with solid shell elements. The mesh information of the foam components is indicated together with the corresponding results since the requirements vary from one poroelastic material to the other. The details on the element type and order, maximum element size and number of nodes of the different components are summarized in Table 7.1.

The values of the material properties for the different components have been indicated previously in Tables 4.1, 4.2, 4.3 and 5.1. The properties of the plastic Plexiglas[®] cover are provided in the manufacturer's data sheet [165]. The modeled material has a Young's modulus $E = 3.3e9$ Pa, a Poisson's ratio $\nu = 0.37$, a mass density $\rho_s = 1190$ kg m⁻³, and a structural damping coefficient $\eta_s = 0.2$.

Before examining the vibroacoustic behavior of the poroelastic sound packages, the comparability between the measurements and the simulations is checked. To this effect, a system with only structural and acoustic components is studied. We make use of the plastic cover geometry in open and closed configurations, that is, if the steel plate is removed and when the plate is used to complete the enclosure. Among the analyzed parameters we have highlighted the boundary conditions of the structural components and the fluid damping inside the air cavity η_0 . This damping is introduced as the imaginary part of the sound speed c_0 [33]:

$$c_0 = c_r + j c_i = c_r (1 + j \eta_0) \quad (7.1)$$

The results are evaluated in terms of the insertion loss, that is, the difference of the total radiated power between the open configuration and the closed state. The resolution of the system using four parallel Intel[®] Xenon[®] processors E5-2680 v4 at 2.40 GHz in the open and closed configurations took 13 and 15 hours, respectively.

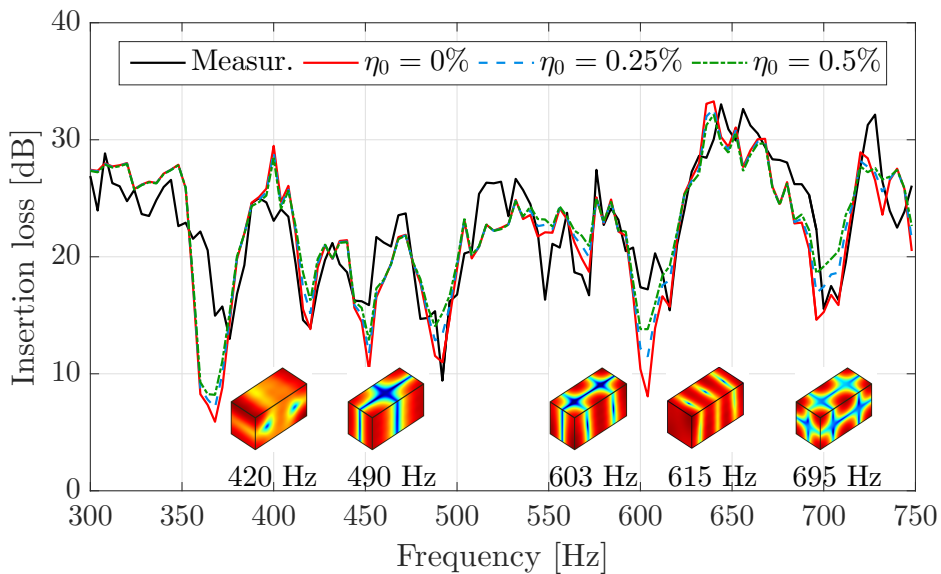


Figure 7.3: Comparison of the measured and simulated insertion loss for the cavity configuration with different damping values of the air inside the cavity η_0 .

The analyses have shown that the boundary conditions of the structural components only slightly modify the results in the frequency range below 100 Hz. On the contrary, the fluid

damping inside the air cavity is the most significant parameter for the middle and high frequency results. In Figure 7.3 we compare the narrow band response of the experiment and the simulations in the frequency range between 300 Hz and 750 Hz for different fluid damping values, namely, 0%, 0.25% and 0.5%. The overall correspondence with the measured insertion loss curve is good, with a few exceptions at the total level of some minima and maxima. The influence of the fluid damping is distinguishable at the cavity resonances, whose mode shapes have been included next to each peak in the diagram. These resonances are especially strong for the closed configuration and, consequently, more sensitive to the fluid damping. For the peaks at approximately 420 Hz and 490 Hz the undamped system $\eta_0 = 0\%$ gives the best correspondence to the measured results. But for the $[2\ 1\ 0]$ and $[3\ 0\ 0]$ cavity eigenmodes at 603 Hz and at 615 Hz the best match is obtained with a damping value of 0.5%. At the 695 Hz resonance and above that frequency a 0.25% fluid damping yields the closest approximation to the experimental data. Out of this analysis a frequency-dependent damping profile for the cavity air is defined and applied to all further models. We employ an undamped inner fluid up to 500 Hz, a damping coefficient of 0.5% between 500 Hz and 690 Hz, and a 0.25% damping value above this frequency. The differences of this damping profile with respect to a constant value are minimal at most frequencies. However, once the profile has been defined, its use does not imply any additional computational effort and slightly improves the correspondence.

7.2 Comparison of numerical and experimental results

In this section we make use of the cavity configuration to analyze the behavior of several noise control treatment concepts. The goal is to assess the suitability of the poroelastic, porous and elastic material formulations presented in Chapter 4. The conclusions from Chapter 5 concerning the modeling of spring-mass systems on a one-square meter flat plate are extended to a more complex setup. Moreover, the absorbing characteristics of sound packages are also investigated. The performance of each noise control treatment is evaluated in insertion loss terms using the cavity closed with the steel plate as reference. The following results have been averaged in third octave bands to improve the legibility.

One-layered system: Absorber

The first examined concept is a single layer of poroelastic material, commonly referred to as absorber because of its good noise absorbing properties. This 25.9 mm thick layer is made of the foam material F, whose properties are included in Tables 4.1 and 4.2. It is a relatively stiff foam with a low damping value, and its surface is open-pored, meaning that the air can penetrate and go through the layer.

The poroelastic foam is discretized with six layers in the thickness direction of 8 mm quadratic elements, resulting in a component with 162148 nodes. The absorber layer can be located at different positions inside the cavity. Firstly, the material is situated on the inner side of the cover front surface, as the small sketch accompanying Figure 7.4 illustrates. The foam is attached to the plastic cover with double-sided adhesive band. The calculation time for the complete system with the poroelastic formulation amounted to 22 hours using four parallel Intel® Xenon® processors E5-2680 v4 at 2.40 GHz. Figure 7.4 shows the insertion loss results measured in the window test bench next to the numerical calculations with the different tested material formulations. The frequency response of the poroelastic and the porous models develop in line with the trend of the

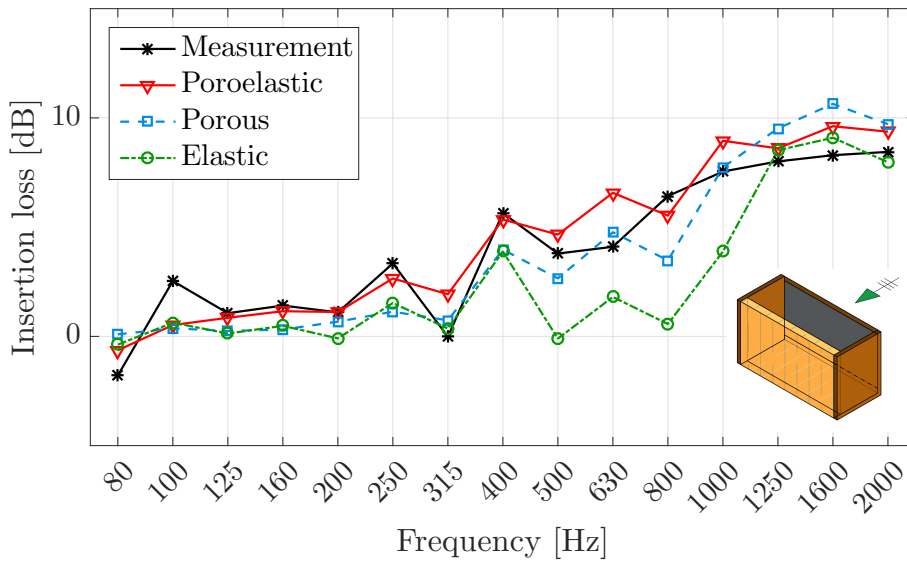


Figure 7.4: Comparison of the measured and simulated insertion loss for the absorber material F placed on the inner front face of the plastic cover with different material formulations.

experimental data. The system with the poroelastic formulation has slightly higher insertion loss values in the frequency range between 160 and 1250 Hz than with the porous simplification. The offset between the results of these two models can be explained because of the direct coupling of the noise control treatment to a vibrating panel. The increase of the structural damping that the foam layer introduces in the plastic cover is only considered in the poroelastic model, but not in the porous one. This effect can also be observed in the vibrational energy of the plastic cover. When applying the poroelastic model, the mean squared velocity of the component is reduced because of the contribution of the foam to the structural damping. However, the differences between the two formulations and the measurement are quite small. It is not feasible to determine which formulation is closer to the real behavior and, consequently, which of the two is the best suited for this application. The modeling as an elastic solid is missing the main dissipation factor, namely the energy losses by absorption. Therefore, this model underestimates the total impact of the foam layer.

For a second configuration the same absorber layer is divided into two pieces of equal size that are placed on the rigid side walls of the cavity (sketch included in Figure 7.5). The direct coupling to a rigid backing strongly reduces the displacement of the foam solid frame. For this reason the poroelastic and the porous formulations behave similarly above 200 Hz, as the insertion loss values in Figure 7.5 display. Under such circumstances, the use of the porous simplification is recommended because it results in a reduction of the number of degrees of freedom per node of the foam component from four to just one DOF. As a result, 20.4% of the computational time and 14.9% of the memory resources can be saved, which is a considerable improvement. Both the poroelastic and the porous formulation are suitable for this configuration. The elastic simplification has a different curve progression than the measurement above 315 Hz because, as aforementioned, this model does not include the absorption effects that are dominant in the middle and high frequency ranges.

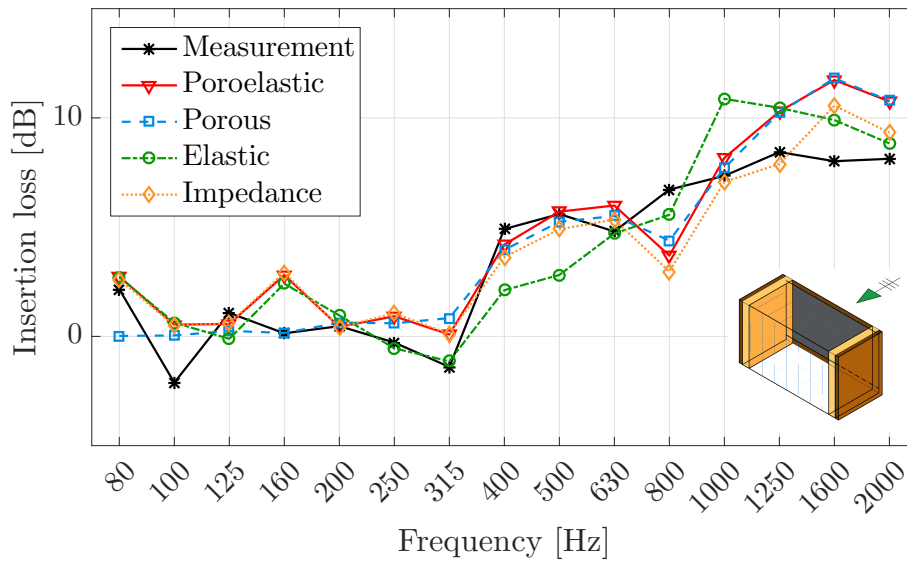


Figure 7.5: Comparison of the measured and simulated insertion loss for the absorber material F placed on the inner faces of the rigid side walls with different material formulations.

Another modeling approach has also been tested. In Section 4.2 we introduced the semi-analytical description of a poroelastic media as an impedance boundary condition. Because the absorber layer is situated on the boundaries of the fluid cavity and is not attached to any vibrating structure, this method can be employed. The simulated response is labeled in Figure 7.5 as *Impedance*. Only small deviations with respect to the poroelastic and porous results are observed. These can be attributed to the missing in-plane effects, since the impedance boundary condition exclusively reproduces a locally reacting, one-dimensional response. The computational time is reduced an additional 18.0% with respect to the porous simplification. All things considered, the impedance modeling also provides an accurate representation of the foam for this application.

We can state that the poroelastic formulation gives reliable results for the description of absorbing layers. Additionally, if the foam component is located on a rigid wall, the choice of the porous simplification or the impedance boundary condition mean a large reduction of required computational resources without affecting the accuracy of the results.

Two-layered system: Spring-mass system

Regarding the representation of two-layered systems, the same division into soft and stiff foams from Chapter 5 is applicable. We must point out that at 1600 Hz the radiated power reaches the minimum measurable level by the PU-probes over the background noise. As a consequence, the obtained information is not reliable above this frequency and has been removed from the measured results displayed here.

We begin the study with the spring-mass system C2, which contains a foam classified as soft. The FE foam component contains 207921 nodes distributed in six layers of quadratic elements with 7 mm lateral length. In Figure 7.6 the insertion loss curves obtained from the numerical models are compared with the experimental data. For this relatively soft foam we notice that the poroelastic formulation best fits the measured data over

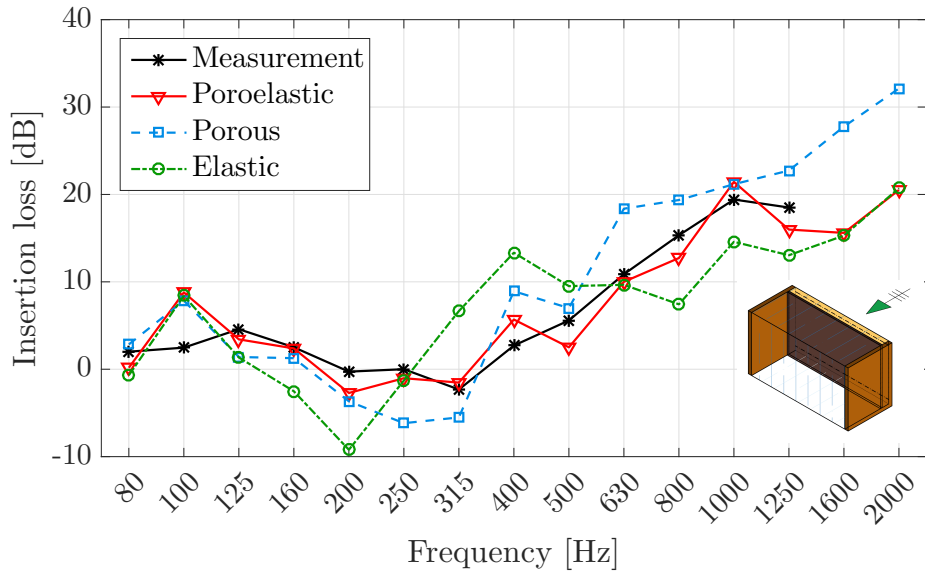


Figure 7.6: Comparison of the measured and simulated insertion loss for the spring-mass system C2 with different material formulations.

the complete frequency range, as already indicated in Section 5.4. This material model gives an accurate prediction of the two important design criteria for spring-mass systems, namely, the spring-mass resonance and the slope at high frequency. The porous model, on the one hand, underestimates the performance at the spring-mass resonance since the damping of the foam skeleton is not included. On the other hand, it overestimates the high-frequent behavior because the transmission of energy to the heavy layer is not as effective in the porous model as it is in reality. Conversely, the absence of the fluid phase in the elastic simplification notably reduces the bulk stiffness of the aggregate, which results in a shift of the complete curve towards lower frequencies.

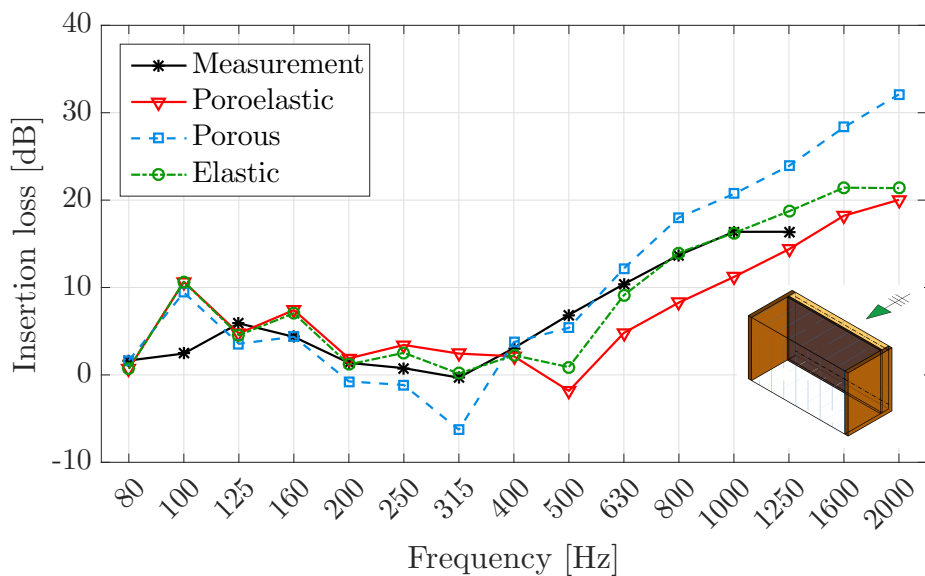


Figure 7.7: Comparison of the measured and simulated insertion loss for the spring-mass system A2 with different material formulations.

The spring-mass system A2 contains a stiff foam with a elasticity modulus per unit thickness of $E/h = 4 \text{ kPa mm}^{-1}$. The poroelastic material A is discretized with 6 mm elements in four layers in the thickness direction, which gives 198643 nodes altogether. All other components, including the heavy layer, remain the same as in the previous configuration. Figure 7.7 presents the measured insertion loss values and the numerical results for the system A2 with the different material formulations. Opposed to the previous example, the results of the elastic model come closest to the experimental data. Moreover, the overall trend is correctly captured. The curve progression obtained with the poroelastic description also exhibits a good prediction of high frequency slope. Nonetheless, the insertion loss level is too low and the frequency of the spring-mass resonance is too high. This curve shift towards higher frequencies is indicative of an overestimation of the material stiffness. The unsuitability of the porous simplification for the modeling of spring-mass systems has been explained above.

Next, the study of the vibroacoustic performance of the spring-mass system B3 follows, whose middle layer is a stiff foam too. This system was previously analyzed in detail in Section 5.4 on the one-square meter plate. The same discretization has been applied as before, namely, five layers of 8 mm quadratic elements, giving a total of 138120 elements. In Figure 7.8 the results from the numerical models calculated with the three material formulations are displayed together with the experimental information. In this particular case the measured data are only available above 200 Hz. To determine the radiated power of the system an intensity PP-probe was used that was only calibrated over that frequency. In general terms, we can identify the same trends as for the results earlier obtained in the one-meter square configuration. The poroelastic model works slightly better in the frequency range around the spring-mass resonance. However, the high frequency slope predicted by the poroelastic and the porous formulations is too steep. The elastic simplification is the model closest to the overall curve progression, but presents a shift of the spring-mass resonance towards higher frequencies. This feature again suggests that a softer material may be required in the numerical setup of an elastic model in the low and middle frequency ranges.

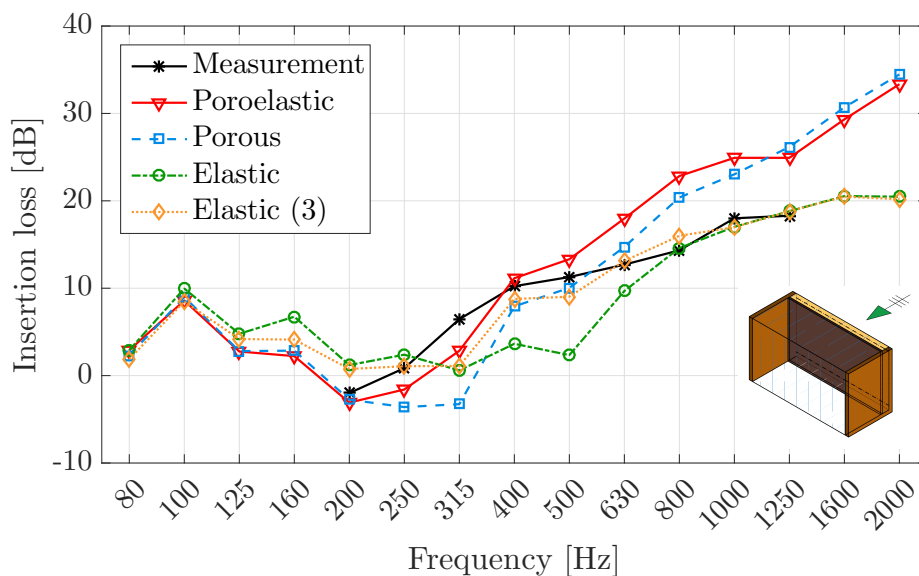


Figure 7.8: Comparison of the measured and simulated insertion loss for the spring-mass system B3 with different material formulations.

In an analogous way to the investigation for the one-square meter geometry, we now employ the values of the manually adjusted frequency-dependent Young's modulus that gave the best agreement. The calculated results are labeled as *Elastic (3)* in the graph. It is worth mentioning that the use of this frequency-dependent elasticity modulus derived from the flat configuration significantly improves the prediction in the cavity setup too. In case that the striven characterization method for the frequency-dependent elastic parameters is not attainable, this fact implies that the effort to find the adequate material parameters may be carried out for a simpler setup such as the flat square plate. Later, the derived results can be applied to model systems of higher geometrical complexity.

Three-layered system: Spring-mass system with absorber

The last sound package concept examined is built by combination of the two former systems. A three-layered system D2F is formed by placing an absorbing layer of the material F on the heavy layer of the spring-mass system D2. A sketch of the complete setup was previously displayed in Figure 7.1b. The synergy of insulation and absorption properties can be an advantageous solution in many applications. Nonetheless, its industrial use is limited because of the great space and weight requirements. Due to the high acoustic performance of this system, the radiated power is masked by the background noise already at the middle frequencies and the experimental results can only be reliably evaluated up to 800 Hz. Thus, the comments on the following paragraphs are limited to this frequency range.

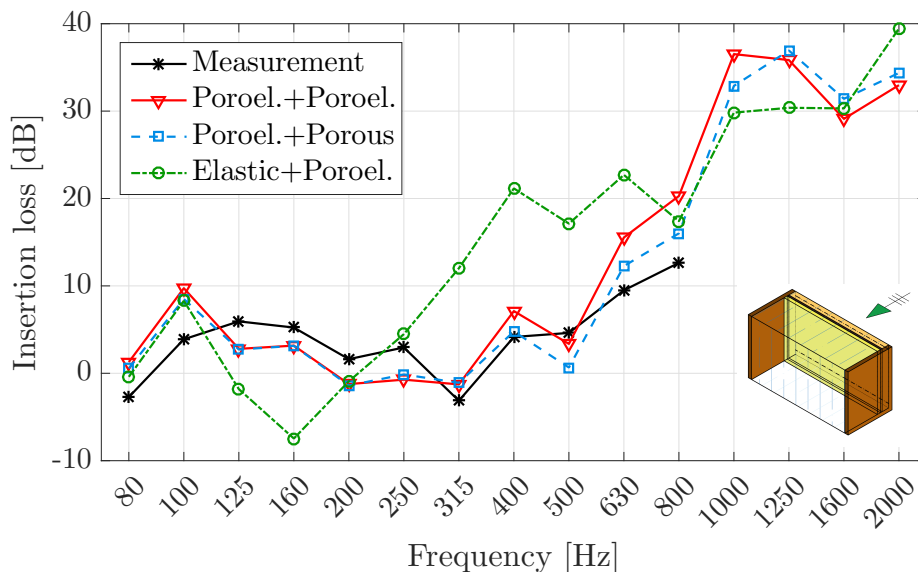


Figure 7.9: Comparison of the measured and simulated insertion loss for the spring-mass absorber system D2F with different material formulations.

Based on the findings of the one- and two-layered systems examined above, the material formulation for each of the two poroelastic layer is chosen. The middle layer of a spring-mass system can either be modeled as a poroelastic or as an elastic medium, depending on its elastic frame properties. In turn, the absorber layer may be described with a poroelastic or a porous model according to the coupling conditions. The simulations have been conducted with the corresponding numerical models for the combination of these

material formulations for the two foam layers. A selection of the results is depicted in Figure 7.9 next to the measured reference data. The designation of the curves for the numerical models indicates the material formulation chosen for the middle spring layer and for the absorber.

Firstly, the behavior of the absorber layer is examined by comparing the results under *Poroel.+Poroel.*, configuration in which the two foam layers are modeled as poroelastic media, and *Poroel.+Porous*, setup with the absorber layer as porous material. We can identify the same trends as we observed before for the absorber layer placed on the vibrating plastic cover. Above 315 Hz the poroelastic model predicts a higher insertion loss value because the solid foam frame adds structural damping, which increases the total power dissipated by the whole system. This behavior points to an interaction between the structural vibration of the heavy layer and the skeleton of the foam when using the poroelastic material model. Nevertheless, the differences between the two models in the red and blue curves and with respect to the measurements are too small to give a reliable statement on which model is more suitable to represent the real state.

Secondly, the middle layer of the spring-mass system contains a foam that is classified as a relatively soft material. Keeping the absorber layer as a poroelastic medium, we include the description of the spring foam using the elastic formulation, which is labeled as *Elastic+Poroel.* in Figure 7.9. Analogously to the conclusions for the soft foams formerly drawn, the elastic formulation incorrectly predicts the system dynamics. This model is not adequate for the representation of the performance of the middle foam since the major contribution to the total behavior, that is, the stiffness of the filling air is neglected. Therefore, the simulation results display a behavior corresponding to a softer foam than it actually is, with a curve shift towards lower frequencies.

In short, in three-layered systems the appropriate selection of the material model for the middle layer is decisive to obtain a correct overall prediction. In contrast, the influence of the chosen material model for the absorber layer is less critical. Besides that, in future measurements either a higher excitation level or another measurement technique should be employed in order to enable the experimental data acquisition at higher frequencies.

7.3 Integration of the numerical front end model with measured transfer functions

In this section, the previous numerical model is combined with experimentally determined information according to the hybrid approach introduced in Chapter 6. The main objectives aimed for are the validation of the hybridization technique as well as the identification of its limitations. Figure 7.10 shows the general workflow with the three principal subsystems of the sound transmission chain. They include the excitation side, the structural components, and the reception side. In the next paragraphs we go into detail about each one of them.

The configuration employed for the investigations is displayed in Figure 7.11. The simplified front end model employed in the former sections constitutes the main structural component. Again, the system is installed in the opening of the window test bench, meaning that the pressure excitation is originated in the reverberation chamber and impinges on the steel plate. The system transmits the vibroacoustic energy into the semi-anechoic room, in which two different boundary conditions have been analyzed. First, the system can freely radiate without constraints in the semi-anechoic room. Second, a rigid screen

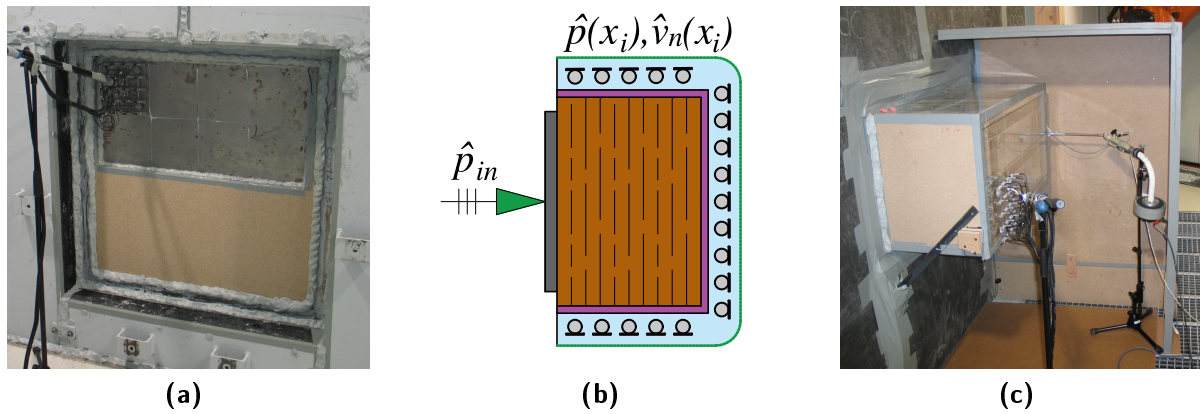


Figure 7.10: Workflow of the hybrid approach: (a) measurement of the input pressure distribution, (b) simulation of the sound transmission through the structural components, (c) reciprocal measurement of the reception transfer functions.

partially covers the cavity, thus preventing the free radiation. The dimensions of the three-sided screen are indicated in Figure 7.11a.

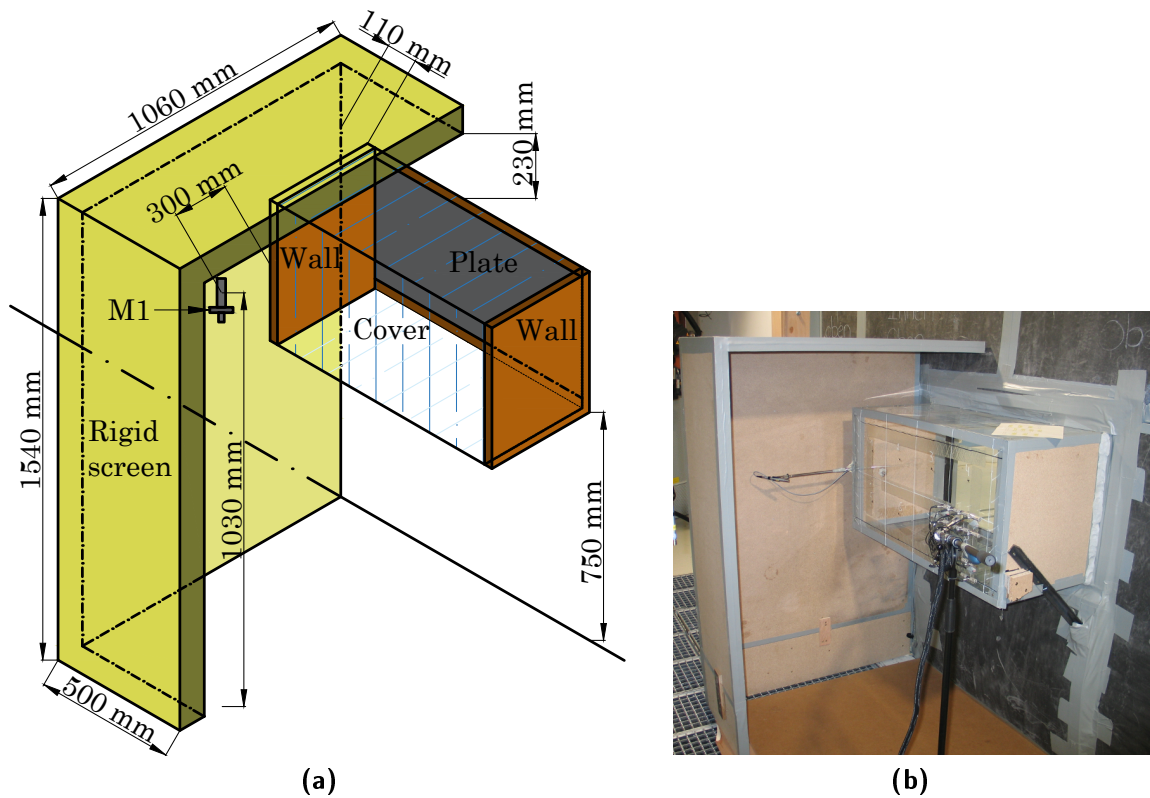


Figure 7.11: Configuration employed for the application of the hybrid approach including the rigid screen; (a) schematic representation with dimensions, (b) picture of the system installed in the window test bench.

In this setup the results are not evaluated in terms of the total radiated power or the insertion loss as before, but the prediction of the sound pressure level (SPL) at a given point is pursued. In order to obtain a reference data set, a microphone was placed at the chosen position *M1* in front of the structure as shown in Figure 7.11. Under

the operational excitation from the reverberation chamber, the resulting SPL was then measured for the configurations with and without the rigid screen.

In the framework of the hybrid methodology, the excitation applied to the numerical model should be as close as possible to the real one. Since we are aiming to predict the absolute value of the sound pressure level, it is decisive that the input information of the simulation matches spatially and in total level the actual excitation. To acquire the incident pressure distribution, the surface of the steel plate on the reverberation chamber side was scanned with the help of the PU-probes array as depicted in Figure 7.10a. Eight array positions, that is, 120 measurement points were needed to cover the complete area. The measured pressure distribution \hat{p}_{in} serves as the input excitation for the simulation. A special kind of boundary condition available in Actran[®] called *BC_Mesh* permits to define a distributed pressure field on the free faces of a structural component [166]. This avoids the explicit modeling of the sending fluid. Figure 7.12 exemplarily displays the pressure distribution applied on the numerical system at 725 Hz.

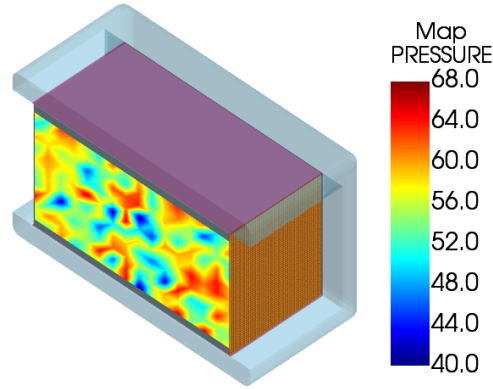


Figure 7.12: Measured input pressure distribution at 725 Hz applied on the plate of the numerical model. The pressure values are indicated in dB.

The sound transmission through the structural component is calculated by means of the numerical model. In this first study, only the steel plate, the fluid cavity and the plastic cover were considered, but no acoustic treatments were included in the model. The later evaluation of the sound pressure level at the point of interest \mathbf{x}_0 requires that the operational and reciprocal variables are known at the same positions \mathbf{x}_i of the integration surface, as Eq. (7.2) indicates. This equation recalls Eq. (6.11) in which additionally the subscripts S and M have been introduced to explicitly designate the quantities obtained in the simulations and in the measurements, respectively. In order to recover the pressure $\hat{p}^S(\mathbf{x}_i)$ and normal velocity $\hat{v}_n^S(\mathbf{x}_i)$ values in the numerical environment, a grid of saving points is defined over the three surfaces of the plastic cover, which is schematically represented in Figure 7.10b. The position of these points coincides with the location of the PU-probes in the experimental procedure.

$$\hat{p}(\mathbf{x}_0) \approx \sum_{i=1}^N \left[\hat{p}^S(\mathbf{x}_i) \left\{ \frac{\hat{v}_n^R(\mathbf{x}_i)}{\hat{Q}(\mathbf{x}_0)} \right\}^M + \hat{v}_n^S(\mathbf{x}_i) \left\{ \frac{\hat{p}^R(\mathbf{x}_i)}{\hat{Q}(\mathbf{x}_0)} \right\}^M \right] \Delta S_i \quad (7.2)$$

The next step consists in the experimental determination of the reception transfer functions following the reciprocal technique presented in Section 6.4. To this effect, an acoustic source of known strength \hat{Q} is placed at the desired point of observation \mathbf{x}_0 . The response

of the surrounding fluid is measured on the outer surface of the structural component with the PU-probes array (Figure 7.10c). The quotients $\hat{p}^R(\mathbf{x}_i)/\hat{Q}(\mathbf{x}_0)$ and $\hat{v}_n^R(\mathbf{x}_i)/\hat{Q}(\mathbf{x}_0)$ are the results of this operation. In the current application the measurement process was repeated for both boundary conditions, with and without the rigid screen.

Finally, the numerical and the experimental data are merged according to Eq. (7.2). This reconstructed sound pressure level at \mathbf{x}_0 can be compared to the reference SPL that was directly measured on the complete system. We begin with the analysis of the free radiating configuration. Figure 7.13 shows the narrow band progression of the pressure level at the observation point. In general, the overall tendency is properly predicted. The correspondence between both curves in the low and middle frequency ranges is very high, with just some discrepancies in the level of certain peaks. As the frequency increases, the trends still match, but these deviations become larger. Especially the maximum and minimum levels of the reconstructed signal are much sharper than in the measured curve. This is attributable to the fact that the simulation of the structural subsystem is calculated by a direct method for discrete frequency values, whereas the experiment averages the information in the frequency bands. This averaging process leads to less pronounced peaks. To ease the comparison of the measured and reconstructed data, the utilization of the third band averaged representation of the results can be useful.

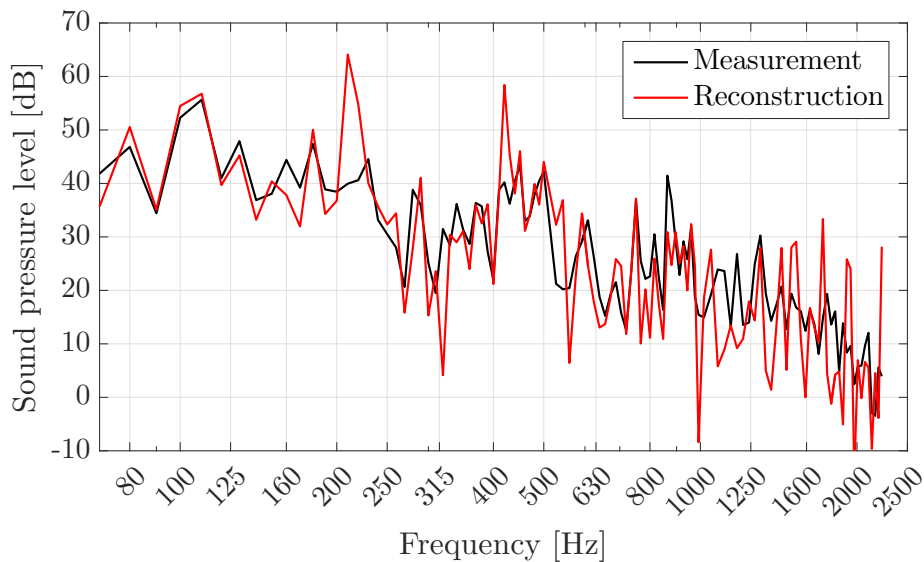


Figure 7.13: Comparison of the measured and reconstructed sound pressure level for the free radiation state.

For the second configuration, a three-sided rigid screen was placed around the structure. The primary objective was to test the influence of the environment of radiation on the total response. Under the assumption of a weak coupling between receiving fluid and the vibrating structure, the modifications in the surrounding air volume should have a small impact on the structural component. The global modes at lower frequencies, however, may not meet this hypothesis.

A preliminary verification of the weak coupling hypothesis was obtained from an auxiliary microphone located inside of the enclosed fluid cavity on one of the rigid side walls. The sound pressure level registered at this position remained unchanged when the rigid screen was built in. Hence, for the hybrid reconstruction of the pressure signal at \mathbf{x}_0 , the same simulation of the structural component as before, that is, in free radiation state was

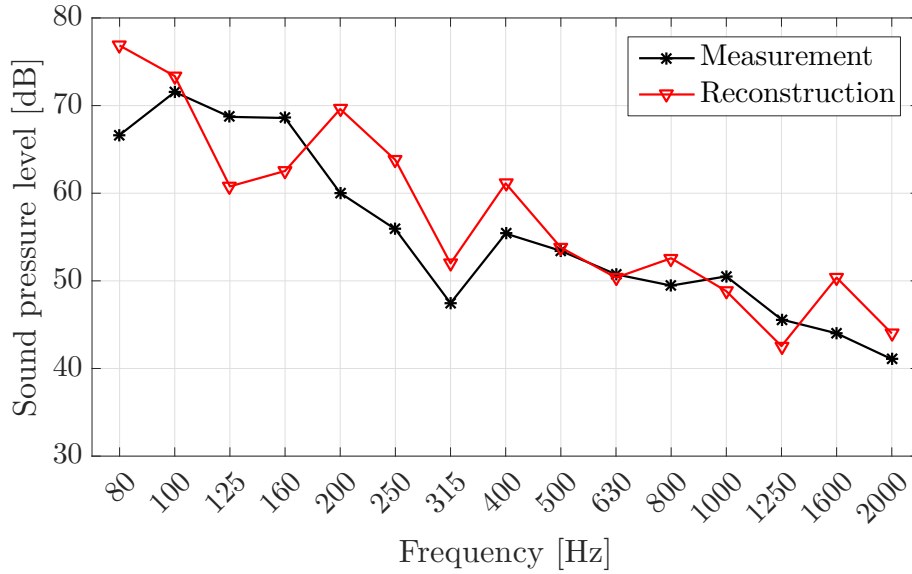


Figure 7.14: Comparison of the measured and reconstructed sound pressure level for the configuration partially covered by the rigid screen.

employed. The only modification in the workflow was the replacement of the reciprocal transfer functions by the ones measured with the rigid screen. Figure 7.14 compares the measured and the reconstructed SPL averaged in third octave bands for the screen configuration. There is a good correspondence of the main characteristics in the curve progressions. Nevertheless, at some frequency bands mainly in the low frequency range the differences reach up to 10 dB. A deviation of this order of magnitude may be inadequate as design criterion.

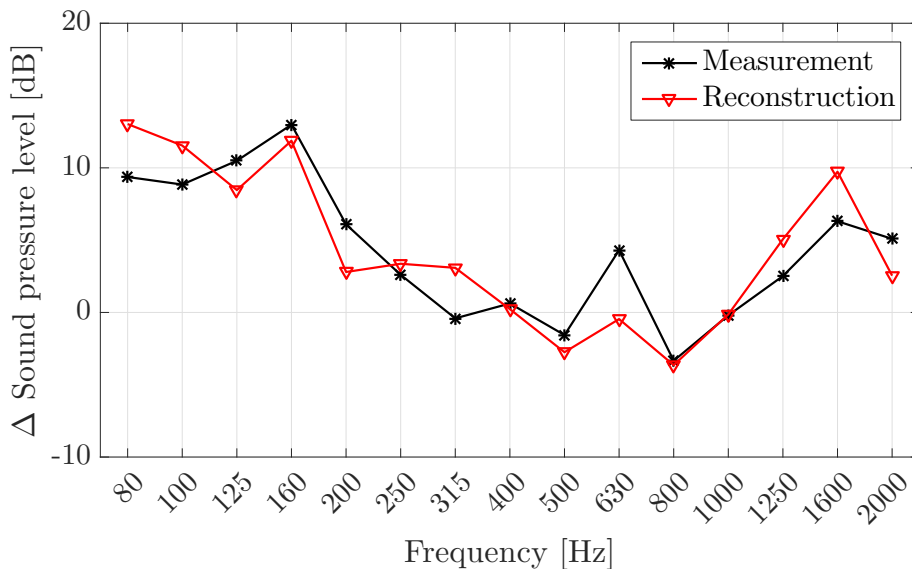


Figure 7.15: Comparison of the measured and reconstructed difference in the sound pressure level for the configurations with and without the rigid screen.

At the virtual early phases of the development process, nevertheless, it can be sufficient to deliver a statement about the relative performance of two or more concepts. An example of such comparisons is displayed in Figure 7.15. Here, the difference of the sound

pressure level for the configuration with and without the rigid screen are presented, in black for the measured and in red the reconstructed SPL values. The maximum deviation between the two frequency progressions is now limited to 5 dB. Moreover, with the exception of the 630 Hz third octave band, the sign of the two curves coincides. Hence, the proposed approach can be employed to comparatively evaluate the vibroacoustic behavior of complex systems.

The present model also manifests the importance of an accurate description of the reception domain. In this specific case, if the structural subsystem is only examined at a component level, the evaluation in terms of the total radiated power will provide the same result for both configurations. Conversely, the consideration of the propagation characteristics of the surrounding air by means of the reciprocal transfer functions weights the response at each point of the vibrating structure. To visualize how this weighting is modified by the boundary conditions, we split the surface of the radiating plastic cover into three areas. The divisions are referred to as *Front*, *Top*, and *Bottom*. As can be noted from Figure 7.16, the introduction of the rigid screen strongly affects the contribution of each surface to the total sound pressure level at the observation point. For the free radiating system most of the acoustic energy comes from the front surface. In contrast, for the system partially covered by the rigid screen the contribution of the three surfaces is more evenly distributed. For the frequency range around the 200 Hz third octave band a resonant behavior is especially identifiable in which most of the energy comes through the top area. The origin of this resonance is the fluid volume captured between the top surface of the plastic cover and the rigid screen.

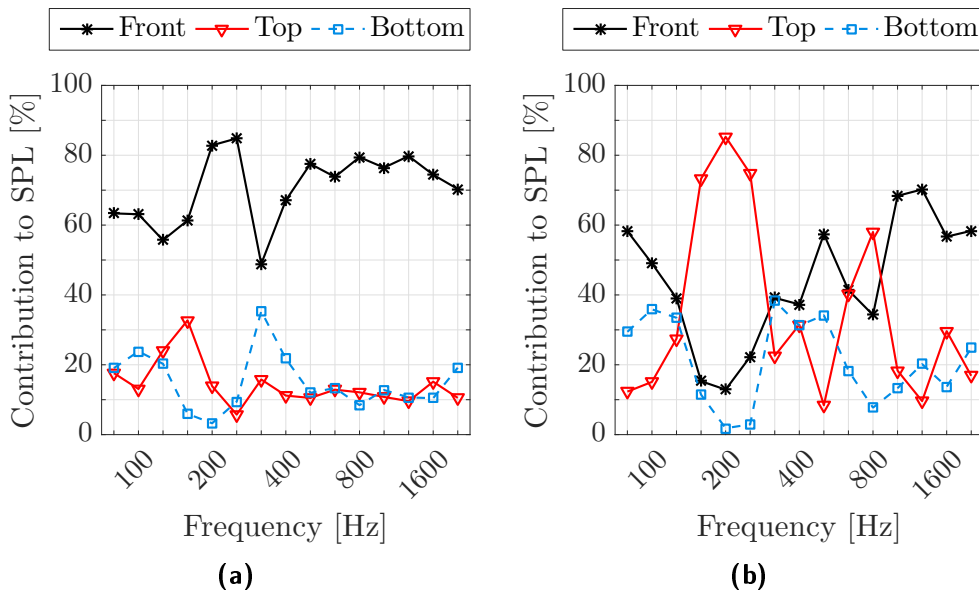


Figure 7.16: Percentage contribution of each surface of the radiating plastic cover to the total sound pressure level (SPL): (a) free radiation state, (b) system partially covered by the rigid screen.

The experimental characterization of the receiving subsystem and its later integration as transfer functions in the sound transmission chain avoids the explicit representation of the reception volume details in the numerical model. This way the size of the problem to be solved is greatly reduced, which is the principal advantage of the proposed hybrid methodology.

7.4 Summary

This chapter has covered the application of the hybrid approach to a simplified model of the front end of a vehicle. The test object was composed by a steel plate and a three-sided plastic cover that represents the firewall and the dashboard of the vehicle, respectively. Together with two acoustically rigid side walls, they enclosed an air cavity. This configuration has been investigated with the help of a numerical model as well as in an experimental mock-up. The first step consisted in the verification of the equivalence between the two environments. The fluid damping inside the enclosed air cavity was identified as a decisive variable to ensure the comparability. A frequency-dependent damping profile was derived out of the contrast of the measured and the numerical results, and it was employed for all the following simulations.

Next, the numerical representation of different sound package concepts based on poroelastic media was examined. The primary advantage of this simplified front end configuration was that, in addition to the insulating spring-mass systems, other noise control treatments with absorbing properties could be studied too. A proper description of the acoustic treatments has been identified as a key parameter in the modeling of the sound transmission. In the numerical setup three material formulations for the modeling of the poroelastic layers were examined, namely, poroelastic, porous, and elastic. The response of the complete system with each material model was compared to the radiated power measured in a window test bench.

For the one-layered treatments the backing conditions turned out to be the determining factor in the choice of a material formulation. Absorber layers attached to vibrating components were precisely represented with the poroelastic or the porous models. The behavior of the two formulations presented only small deviations because of the absence of the frame damping in the porous formulation. In turn, if a rigid wall was backing the foam, the utilization of the porous simplification or the impedance boundary condition provided almost the same results as the full poroelastic model. Additionally, their application involved a significant reduction of the required computational resources.

The investigations of the two-layered spring-mass systems confirmed the conclusions drawn for the one-square meter plate configuration tested in Chapter 5. The division into soft and stiff foams according to their elasticity modulus per unit thickness was also valid. The soft foams were found to be properly described with the poroelastic formulation, whereas the elastic simplification was the most suitable model for the stiff materials. In the example of the system B3 the impact of the frame elastic properties was tested. The use of the adjusted frequency-dependent Young's modulus derived in Section 5.4 notably improved the correlation with the experimental data set.

The combination of a spring-mass and an absorber in a three-layered compound was also inspected. The appropriate selection of the material model for the spring middle layer proved to be the most important variable. Since the analyzed foam had a soft skeleton, the poroelastic formulation delivered the best match to the measured results. The description of the uppermost absorber layer played a secondary role. Either the poroelastic or the porous material models could be chosen for the absorber without noticeably modifying the results.

Two general issues were identified during the examinations. First, the evaluation of the numerical simulations is associated to long calculation times, which may compromise the applicability of the method. Most of the effort is related to the resolution of the poroelastic components because of the four degrees of freedom per node and due to the required

fine discretizations. Therefore, it is advisable to make use of the simplified formulations whenever appropriate. Moreover, specific meshes could be employed in different frequency ranges in order to optimize the element size. Another alternatives could be the utilization of higher order elements or the combination of the Finite Element model with other techniques such as the Patch Transfer Function or the model order reduction techniques introduced in Section 5.5.

The second problem, which was also highlighted in Chapter 5, arises in the determination of the frequency-dependent elastic parameters for the skeleton of the foam. The absence of standard procedures hinders the proper modeling of the poroelastic media. Nevertheless, the application for the spring-mass system B3 showed that the parameters derived from the one-square meter geometry were also appropriate for the more complex setup. This means that the material characterization based on the results on a flat plate could be an intermediate solution if any better determination technique can be developed.

In the last part of the chapter the hybrid methodology for the prediction of the sound transmission was implemented. The numerical model of the simplified front section was integrated with experimental information. The pressure distribution acting upon the structure was first measured and later used as the excitation of the simulation setup. On the reception side, the transfer functions between the surface of the vibrating structure and the observation point were experimentally obtained by applying the reciprocity principle. The combination of the measured transfer functions with the structural response calculated by the numerical model allowed for the reconstruction of the sound pressure level at the desired position. Two different configurations were considered, namely, a free radiation state and a configuration partially covered with a rigid screen. For both setups the numerical model remained the same and only the transfer functions were correspondingly updated. The reconstructed signal for the free propagation was close to the reference data. In the case of the partially covered system, even if the overall trends were still correctly predicted, the discrepancies in the total level became larger. However, a good agreement was achieved if the results were evaluated in relative terms. In other words, the difference of the reconstructed SPL between the free and the partially covered configurations closely matched the difference of the two measured sound pressure levels. This kind of relative statements meet the needs at the early stages of the development cycle, thus enabling the comparison of different concepts in the virtual phases and, eventually, making possible the definition of optimal configurations.

Chapter 8

Concluding remarks and outlook

Acoustics contributes to the quality perception of a passenger car. In order to assist in the design process of the passive acoustic treatments, robust prediction models are required. These models need to include an accurate description of the sound packages, as well as a realistic representation of the excitation sources and all the important transmission paths. Nowadays, the verification of the acoustic specifications is mostly based on experiments. However, the first statements about the NVH performance are demanded at the early development phases, when only virtual models are at disposal. In turn, a complete numerical calculation is not practicable due to the high complexity of the considered phenomena. As a solution a combination of numerical and experimental approaches in a hybrid method has been proposed in this thesis.

The present thesis pursued the implementation and validation of a hybrid tool to predict the airborne sound transmission including poroelastic noise control treatments. The synergy of measured and calculated data allows to exploit the benefits of both approaches. On the one hand, the experimental procedures automatically provide a lifelike representation of the excitation and receiving environments. On the other hand, the simulations give the flexibility to analyze in detail different design configurations with just a moderate effort and reduced costs.

The application of the proposed method comprised two stages. First, the modeling of the poroelastic acoustic treatments was analyzed in a numerical setting. The literature survey revealed that three material formulations for homogenized poroelastic media are available. Throughout this work they have been referred to as poroelastic, porous and elastic. The investigations on several insulating spring-mass systems attached to a flat steel plate evidenced that the elastic properties of the foam determine the choice of a suitable material formulation. As reference set served different measurements conducted in a window test bench. Moreover, the coupling conditions of the foam to the plate should be known in order to correctly represent the energy distribution inside the poroelastic medium. The major difficulty arose from the foam material characterization since most properties lack standardized determination procedures. Furthermore, even if the constant measured properties predicted well the general performance trends, the use of a frequency-dependent Young's modulus allowed to capture the right dynamics over the frequency. A first attempt of a dynamic characterization method delivered too stiff elasticity values that blocked the double wall behavior.

The same poroelastic material formulations were examined in a geometrically more complex setup. The structure was composed of a steel plate, a three-sided plastic cover and two rigid walls that enclosed a hexahedral air cavity, which represented a simplified vehicle front end. Different passive concepts for noise reduction could be studied in this environment. The results of the insulating spring-mass systems confirmed the findings of the flat plate configuration. Additionally, the cavity setting enabled the investigation of

sound packages with absorption features. The backing conditions emerged as key element in the modeling of absorber layers. For the three-layered systems it was observed that the spring layer controlled the whole system dynamics and, therefore, its material formulation should be carefully selected. In short, the numerical modeling of noise control treatments based on poroelastic media was successfully completed.

In the second step, this numerical system was combined with experimentally determined components to complete the description of the sound transmission chain. On the excitation side, the pressure distribution impinging on the steel plate was measured and applied as input of the numerical model. The propagation properties of the receiving domain were included with the help of reciprocally determined transfer functions that linked the surface of the vibrating structure and the observation point. Based on the mathematical principles of the panel contribution analysis, the output of the numerical model and the experimental transfer functions were merged to reconstruct the sound pressure level at a desired position. The results have proved that the hybrid methodology can be employed to predict the sound transmission through complex systems. Although some discrepancies were noticed for the absolute pressure values, the relative quantities and tendencies were properly reproduced. During the conceptual development stages such relative statements are sufficient.

One of the main advantages of the proposed approach is that the excitation, the structure and the reception subsystems can be analyzed independently from the other two. That way, the evaluation can be carried out by the most adequate method, either numerical or experimental, depending on the data at disposal and the project stage. Another benefit of the hybridization stems from the application of the measured transfer functions, which weight the structural response according to the contribution of each partial surface to the total level. Thus, problems and weak spots can be rightly identified from the perception point of view and, in further developments, the corresponding measures can be adopted. As aforementioned, the characterization of the poroelastic components remains an open issue. For most of the material parameters no standard procedures are available. The investigations within the scope of this work pointed out that the poro-mechanical parameters have a secondary role in the material dynamics. The utilization of a standardized parameter set could help significantly to reduce the characterization effort. Conversely, the elastic parameters have a large impact on the material behavior. In order to improve the quantitative correspondence between the numerical predictions and the reference measurements a frequency-dependent Young's modulus is needed. The definition of such elasticity profile, however, poses a major challenge. An examined technique to obtain its value out of the direct characterization of the poroelastic material samples did not produce satisfactory results and should be reviewed. On another note, the investigations in the front end model demonstrated that, if no adequate direct procedure is available, the elasticity values derived from the flat plate geometry could also be employed for the more complex setup with an acceptable output.

The extensive consumption of computational resources and the very long calculation times are a limitation of the implementation of the Finite Element Method in problems including poroelastic media. The non-linear and frequency-dependent dissipative behavior of the poroelastic media impedes the utilization of reduction strategies that are state of the art in linear problems. For this reason, the use of the material simplified formulations, especially of the porous model, is strongly recommended to reduce the calculation effort provided that the application conditions are met.

In summary, the proposed hybrid approach was employed to describe the sound propagation through a simplified front end model taking into account the essential elements of the transmission chain. The inclusion of the real excitation together with the introduction of the receiving domain properties allowed to compare the performance of different systems including a detailed numerical representation of the structural components. The good correlation of the results to the measured reference data proved the validity of the presented method.

Outlook

In the investigations within the scope of this thesis the hybrid method was only verified for structural components without sound packages. The next steps should gradually increase the complexity of the configurations to achieve a more realistic model of the vehicle front section. As a first priority, the setup should include the representation of the noise control treatments having regard to the findings of the previously examined numerical systems. The extension to curved geometries and non-uniform thicknesses usually present in the actual cars require the meshing of irregular bodies, which needs to be attentively conducted. Furthermore, the input pressure distribution of the reverberation chamber could be replaced by real operating data. For example, the radiated acoustic energy measured in an engine test bench could be integrated. Eventually the detail degree of the transmission chain description should permit the NVH engineer to identify weak spots and other issues in the early development stages. Moreover, the proposed approach should set the basis for the development of a robust tool to optimize the location and dimensions of the noise control treatments taking into consideration the real application environment. In the numerical evaluation of the sound packages the poroelastic material characterization remains in a central position, since it provides the input parameters of the models. Consequently, a reliable technique for the determination of the material parameters is essential. So far, we could not find a suitable characterization procedure for the poroelastic middle layer in spring-mass systems. The aspired solution should operate at material level, that is, without the need to examine the complete spring-mass system. To the extent possible, the requirement of specific or cumbersome experimental equipment should be avoided. First, the potential of a standardized poro-mechanical parameter set has to be confirmed. Further analyses with other poroelastic material samples that are commonly employed as noise control treatments are necessary to this end. Second, regarding the elastic parameters, a detailed inspection of the tested method for the frequency-dependent characterization must be carried out. That way, one may gain a deeper understanding of the interactions taking place and be able to identify if any relevant effects are missing. If the striven characterization approach cannot be satisfactorily attained, the process for the identification of the elasticity profile out of the spring-mass system measurements should be automated. An optimization loop comparing the experimental information of the spring-mass systems in a flat geometry with numerical results could deliver a proper Young's modulus to fit curve progression. The obtained properties could then be applied to configurations of higher complexity.

A great obstacle to the operational implementation of the presented numerical and hybrid methods is the intensive use of calculation resources. In order to alleviate this issue, improvements in the numerical efficiency need to be undertaken. Besides the employment of specific meshes for different frequency ranges and the use of the simplified material formulations, the incorporation of other techniques should be inspected. One option are

hierarchical element shape functions for the Finite Element discretization of poroelastic domains. Several studies have shown that they present a better convergence rate than linear and quadratic elements. Besides, special strategies for the modal decomposition of the non-linear frequency-dependent poroelasticity equations can significantly reduce the computational time without affecting the accuracy. Another alternative could be the decomposition of the problem domain in subsystems that are independently calculated and later coupled again, like the substructuring scheme called patch transfer function. Thus, the size of the systems to be solved is notably decreased. Nevertheless, all these techniques are currently being developed and have only been tested on academic examples. They show a great potential to increase the numerical efficiency and, hence, their evolution should be followed closely to evaluate their limitations for the application to real problems.

References

- [1] K. Genuit, “Vehicle interior noise – combination of sound, vibration and interactivity,” *Sound and Vibration*, vol. 43, no. 12, p. 8, 2009.
- [2] L. Ferrali, D. Caprioli, and M. Cardillo, “The NVH package of electrified passenger vehicles: Future challenges and trends,” in *24th International Congress on Sound and Vibration, London*, 2017.
- [3] A. Fortino, L. Eckstein, J. Viehöfer, and J. Pampel, “Acoustic vehicle alerting systems (AVAS) – regulations, realization and sound design challenges,” *SAE International journal of passenger cars-mechanical systems*, vol. 9, no. 2016-01-1784, pp. 995–1003, 2016.
- [4] A. Mahapatra, “Guidelines and principles for noise and vibration performance in an autonomous vehicle,” *The Journal of the Acoustical Society of America*, vol. 142, no. 4, pp. 2488–2488, 2017.
- [5] K. Ohta, K. Amano, A. Hayashida, G. Zheng, and I. Honda, “Analysis of piston slap induced noise and vibration of internal combustion engine,” *Journal of Environment and Engineering*, vol. 6, no. 3, pp. 712–722, 2011.
- [6] M. Müller, H.-G. Eckel, M. Leibach, and W. Bors, “Reduction of noise and vibration in vehicles by an appropriate engine mount system and active absorbers,” Tech. Rep. 960185, SAE Technical Paper, 1996.
- [7] X. Wang, ed., *Vehicle noise and vibration refinement*, ch. Vehicle interior noise refinement – cabin sound package design and development. Woodhead Publishing, London, 2010.
- [8] J. Scheuren, R. Schirmacher, and J. Hobelsberger, “Active design of automotive engine sound,” in *INTER-NOISE and NOISE-CON Congress and Conference Proceedings*, pp. 1544–1549, Institute of Noise Control Engineering, 2002.
- [9] K. Genuit, *Sound-engineering im Automobilbereich*. Springer-Verlag Berlin Heidelberg, 2010.
- [10] S. Elliott, *Signal processing for active control*. Elsevier, 2000.
- [11] M. Luegmair, “Simulation der Fahrzeugakustik in der frühen Entwicklungsphase,” in *In the proceedings of the 42. Jahrestagung für Akustik - DAGA*, 2016.
- [12] L. Dejaeger, J.-F. Rondeau, P. Chanudet, and B. Auffray, “Transmission Loss trim FEM simulation of lightweight automotive dashboard insulators with consideration of the instrument panel,” in *Proceedings of the Acoustics 2012 Nantes Conference*, pp. 715–720, 2012.

- [13] J.-F. Rondeau, L. Dejaeger, A. Guellec, A. Caillet, and L. Bischoff, “Cockpit module analysis using poroelastic finite elements,” Tech. Rep. 2014-01-2078, SAE Technical Paper, 2014.
- [14] S. Korte, *Untersuchung der hochfrequenten akustischen Transmission einer Kfz-Bodengruppe mittels Statistischer Energieanalyse*. PhD thesis, Technische Universität Berlin, 2005.
- [15] A. Duval, L. Dejaeger, L. Bischoff, and C. Morgenstern, “Trim FEM simulation of a headliner cut out module with structureborne and airborne excitations,” Tech. Rep. 2012-01-1524, SAE Technical Paper, 2012.
- [16] A. Caillet, L. Alimonti, and A. Golota, “Modelling Acoustic Trims in FEM, an Overview of the Different Simulation Methods,” Tech. Rep. 2016-01-1849, SAE Technical Paper, 2016.
- [17] R. Stelzer, T. Courtois, K.-S. Chae, S. Daewon, and S.-G. Hong, “FE simulation of the transmission loss performance of vehicle acoustic components at low and medium frequencies,” *SAE International Journal of Passenger Cars-Mechanical Systems*, vol. 7, no. 2014-01-2081, pp. 1212–1220, 2014.
- [18] D. d’Udekem, F. Acher, B. Khatib-Shahidi, K.-T. Shu, H. Rabbani, and W. Liu, “Efficient analysis of a fully-trimmed car body using modal approaches,” in *INTER-NOISE and NOISE-CON Congress and Conference Proceedings*, pp. 187–195, Institute of Noise Control Engineering, 2008.
- [19] J. Monet Descombey, *Numerical modeling of poroelastic multilayered materials for automotive application (redacted in French)*. PhD thesis, Université de Technologie de Compiègne, 2009.
- [20] A. Caillet, A. Guellec, D. Blanchet, and T. Roy, “Prediction of Structureborne Noise in a Fully Trimmed Vehicle Using Poroelastic Finite Elements Method (PEM),” Tech. Rep. 2014-01-2083, SAE Technical Paper, 2014.
- [21] C. Schedlinski, F. Wagner, K. Bohnert, M. Kusel, D. Clasen, C. Stein, C. Glandier, M. Kaufmann, and E. Tijs, “Computational model updating of structural damping and acoustic absorption for coupled fluid-structure-analyses of passenger cars,” in *ISMA Conference on Noise and Vibration Engineering, Belgium*, pp. 4229–4244, 2008.
- [22] C. Schedlinski *et al.*, “Untersuchungen zur Erfassung von Absorption bei gekoppelten Fluid/Struktur-Analysen von Gesamtkraftfahrzeugmodellen,” *VDI-Berichte*, no. 2093, pp. 321–330, 2010.
- [23] F. Tinti, C. Scaffidi, and A. Perazzolo, “Improvement of interior acoustics of a top-class car in the low frequency range using a hybrid numerical-experimental technique,” *WIT Transactions on The Built Environment*, vol. 28, 1997.
- [24] M. J. Lighthill, “On sound generated aerodynamically I. General theory,” *Proc. R. Soc. Lond. A*, vol. 211, no. 1107, pp. 564–587, 1952.
- [25] M. J. Lighthill, “On sound generated aerodynamically II. Turbulence as a source of sound,” *Proc. R. Soc. Lond. A*, vol. 222, no. 1148, pp. 1–32, 1954.

- [26] P. Zeller, *Handbuch Fahrzeugakustik*, vol. 2. Vieweg+Teubner Verlag, Wiesbaden, Springer, 2012.
- [27] M. Pflüger, F. Brandl, U. Bernhard, and K. Feitzelmayer, *Fahrzeugakustik*. Springer-Verlag, 2010.
- [28] O. Gotfrýd, V. Klír, and J. Drda, “Testing of Modern Vehicles on a 2Wd Roller Test Bench,” *Journal of Middle European Construction and Design of Cars*, vol. 11, no. 1, pp. 23–27, 2013.
- [29] D. Rhazi and N. Atalla, “Acoustic and vibration response of a structure with added noise control treatment under various excitations,” *The Journal of the Acoustical Society of America*, vol. 135, no. 2, pp. 693–704, 2014.
- [30] C. Fernandez, C. Soize, and L. Gagliardini, “Sound-insulation layer modelling in car computational vibroacoustics in the medium-frequency range,” *Acta Acustica united with Acustica*, vol. 96, no. 3, pp. 437–444, 2010.
- [31] F. Duvigneau, S. Nitzschke, E. Woschke, and U. Gabbert, “A holistic approach for the vibration and acoustic analysis of combustion engines including hydrodynamic interactions,” *Archive of Applied Mechanics*, vol. 86, no. 11, pp. 1887–1900, 2016.
- [32] R. Ohayon and C. Soize, *Advanced computational vibroacoustics: Reduced-order models and uncertainty quantification*. Cambridge University Press, 2014.
- [33] E. Skudrzyk, *The Foundations of Acoustics: Basic Mathematics and basic Acoustics*. Springer Science & Business Media, 2012.
- [34] S. A. Hambric, S. H. Sung, and D. J. Nefske, *Engineering vibroacoustic analysis: Methods and applications*. John Wiley & Sons, 2016.
- [35] H. Beriot and M. Tournour, “On the locally-conformal perfectly matched layer implementation for Helmholtz equation,” in *INTER-NOISE and NOISE-CON Congress and Conference Proceedings*, pp. 503–513, Institute of Noise Control Engineering, 2009.
- [36] J.-C. Autrique and F. Magoulès, “Studies of an infinite element method for acoustical radiation,” *Applied Mathematical Modelling*, vol. 30, no. 7, pp. 641–655, 2006.
- [37] S. Marburg and B. Nolte, *Computational acoustics of noise propagation in fluids: Finite and boundary element methods*. Springer, 2008.
- [38] L. Wardle, “An introduction to the Boundary Element Method,” in *North-Holland mathematics studies*, vol. 83, pp. 525–551, Elsevier, 1984.
- [39] K. De Langhe, *High frequency vibrations: Contributions to experimental and computational SEA parameter identification techniques*. PhD thesis, Katholieke Universiteit Leuven, 1996.
- [40] C. B. Burroughs, R. W. Fischer, and F. R. Kern, “An introduction to Statistical Energy Analysis,” *The Journal of the Acoustical Society of America*, vol. 101, no. 4, pp. 1779–1789, 1997.

- [41] F. Amoroso, A. De Fenza, M. Linari, M. Di Giulio, and L. Lecce, “Energy finite element analysis (EFEA) approach for fuselage noise prediction,” in *INTER-NOISE and NOISE-CON Congress and Conference Proceedings*, pp. 670–680, Institute of Noise Control Engineering, 2012.
- [42] W. Desmet, *A wave based prediction technique for coupled vibro-acoustic analysis*. PhD thesis, Katholieke Universiteit Leuven, 1998.
- [43] B. Pluymers, *Wave based modelling methods for steady-state vibro-acoustics*. PhD thesis, Katholieke Universiteit Leuven, 2006.
- [44] F. B. Jensen, W. A. Kuperman, M. B. Porter, and H. Schmidt, *Computational ocean acoustics*. Springer Science & Business Media, 2011.
- [45] N. Atalla and F. Sgard, *Finite element and boundary methods in structural acoustics and vibration*. CRC Press, 2015.
- [46] A. Sommerfeld, *Partial differential equations in physics*, vol. 1. Academic press, 1949.
- [47] W. Desmet and D. Vandepitte, “Finite Element Method in Acoustics,” in *ISAAC13-International Seminar on Applied Acoustics, Leuven*, 2002.
- [48] K.-J. Bathe, *Finite element procedures*. Klaus-Jurgen Bathe, 2006.
- [49] E. Reissner, “The effect of transverse shear deformation on the bending of elastic plates,” *Journal of applied Mechanichs*, pp. A69–A77, 1945.
- [50] R. D. Mindlin, “Influence of rotatory inertia and shear on flexural motions of isotropic, elastic plates,” *Journal of applied Mechanichs*, vol. 18, p. 31, 1951.
- [51] J. Caseiro, R. Valente, A. Reali, J. Kiendl, F. Auricchio, and R. A. De Sousa, “On the Assumed Natural Strain method to alleviate locking in solid-shell NURBS-based finite elements,” *Computational Mechanics*, vol. 53, no. 6, pp. 1341–1353, 2014.
- [52] C. Barthel, *Verbesserte Mechanikmodelle für das virtual engineering*. VDI-Verlag, 2014.
- [53] N. H. Nguyen, V. Pham, M. Hogge, and J. Ponthot, “An assumed natural strain technique for 2D solid-shell elements,” in *Fourth International Conference on Advanced COmputational Methods in ENgineering (ACOMEN 2008)*, 2008.
- [54] R. J. Alves de Sousa, R. P. Cardoso, R. A. Fontes Valente, J.-W. Yoon, J. J. Grácio, and R. M. Natal Jorge, “A new one-point quadrature enhanced assumed strain (EAS) solid-shell element with multiple integration points along thickness - part II: nonlinear applications,” *International Journal for Numerical Methods in Engineering*, vol. 67, no. 2, pp. 160–188, 2006.
- [55] F. Ihlenburg, *Finite element analysis of acoustic scattering*, vol. 132. Springer Science & Business Media, 2006.
- [56] L. L. Thompson, “A review of finite-element methods for time-harmonic acoustics,” *The Journal of the Acoustical Society of America*, vol. 119, no. 3, pp. 1315–1330, 2006.

- [57] A. Bayliss, C. I. Goldstein, and E. Turkel, "On accuracy conditions for the numerical computation of waves," *Journal of Computational Physics*, vol. 59, no. 3, pp. 396–404, 1985.
- [58] K. Gerdes, "A review of infinite element methods for exterior Helmholtz problems," *Journal of Computational Acoustics*, vol. 8, no. 1, pp. 43–62, 2000.
- [59] J.-P. Coyette and B. Van den Nieuwenhof, "A conjugated infinite element method for half-space acoustic problems," *The Journal of the Acoustical Society of America*, vol. 108, no. 4, pp. 1464–1473, 2000.
- [60] A. Hekmati, D. Ricot, and P. Druault, "Numerical synthesis of aeroacoustic wall pressure fields over a flat plate: Generation, transmission and radiation analyses," *Journal of Sound and Vibration*, vol. 332, no. 13, pp. 3163–3176, 2013.
- [61] M. A. Biot, "Theory of propagation of elastic waves in a fluid-saturated porous solid. I. Low frequency range," *The Journal of the Acoustical Society of America*, vol. 28, no. 2, pp. 168–178, 1956.
- [62] M. A. Biot, "Theory of propagation of elastic waves in a fluid-saturated porous solid. II. Higher frequency range," *The Journal of the Acoustical Society of America*, vol. 28, no. 2, pp. 179–191, 1956.
- [63] J. Allard, *Propagation of sound in porous media: Modelling sound absorbing materials*. Elsevier, 1993.
- [64] D. L. Johnson, J. Koplik, and R. Dashen, "Theory of dynamic permeability and tortuosity in fluid-saturated porous media," *Journal of fluid mechanics*, vol. 176, pp. 379–402, 1987.
- [65] S. R. Pride and J. G. Berryman, "Connecting theory to experiment in poroelasticity," *Journal of the Mechanics and Physics of Solids*, vol. 46, no. 4, pp. 719–747, 1998.
- [66] M. Sharma, "Wave propagation in a general anisotropic poroelastic medium: Biot's theories and homogenisation theory," *Journal of Earth System Science*, vol. 116, no. 4, pp. 357–367, 2007.
- [67] J. Allard and N. Atalla, *Propagation of sound in porous media: Modelling sound absorbing materials 2e*. John Wiley & Sons, 2009.
- [68] N. Atalla, R. Panneton, and P. Debergue, "A mixed displacement-pressure formulation for poroelastic materials," *The Journal of the Acoustical Society of America*, vol. 104, no. 3, pp. 1444–1452, 1998.
- [69] S. Rigobert, F. C. Sgard, and N. Atalla, "A two-field hybrid formulation for multilayers involving poroelastic, acoustic, and elastic materials," *The Journal of the Acoustical Society of America*, vol. 115, no. 6, pp. 2786–2797, 2004.
- [70] S. R. Pride, F. D. Morgan, and A. F. Gangi, "Drag forces of porous-medium acoustics," *Physical review B*, vol. 47, no. 9, p. 4964, 1993.

- [71] D. K. Wilson, “Relaxation-matched modeling of propagation through porous media, including fractal pore structure,” *The Journal of the Acoustical Society of America*, vol. 94, no. 2, pp. 1136–1145, 1993.
- [72] R. Panneton and X. Olny, “Acoustical determination of the parameters governing viscous dissipation in porous media,” *The Journal of the Acoustical Society of America*, vol. 119, no. 4, pp. 2027–2040, 2006.
- [73] L. Jaouen, B. Brouard, N. Atalla, and C. Langlois, “A simplified numerical model for a plate backed by a thin foam layer in the low frequency range,” *Journal of Sound and Vibration*, vol. 280, no. 3-5, pp. 681–698, 2005.
- [74] Y. Champoux and J.-F. Allard, “Dynamic tortuosity and bulk modulus in air-saturated porous media,” *Journal of applied physics*, vol. 70, no. 4, pp. 1975–1979, 1991.
- [75] X. Olny and R. Panneton, “Acoustical determination of the parameters governing thermal dissipation in porous media,” *The Journal of the Acoustical Society of America*, vol. 123, no. 2, pp. 814–824, 2008.
- [76] Q. Serra, M. Ichchou, and J.-F. Deü, “Wave properties in poroelastic media using a wave finite element method,” *Journal of Sound and Vibration*, vol. 335, pp. 125–146, 2015.
- [77] H. Liu, S. Finnveden, M. Barbagallo, and I. Lopez Arteaga, “Wave propagation in sandwich panels with a poroelastic core,” *The Journal of the Acoustical Society of America*, vol. 135, no. 5, pp. 2683–2693, 2014.
- [78] O. Dazel, F. Sgard, F.-X. Becot, and N. Atalla, “Expressions of dissipated powers and stored energies in poroelastic media modeled by $\{u, U\}$ and $\{u, P\}$ formulations,” *The Journal of the Acoustical Society of America*, vol. 123, no. 4, pp. 2054–2063, 2008.
- [79] F. Dunn, W. Hartmann, D. Campbell, and N. H. Fletcher, *Springer handbook of acoustics*. Springer, 2015.
- [80] R. Panneton, “Comments on the limp frame equivalent fluid model for porous media,” *The Journal of the Acoustical Society of America*, vol. 122, no. 6, pp. EL217–EL222, 2007.
- [81] O. Doutres, N. Dauchez, J.-M. Génevaux, and O. Dazel, “Validity of the limp model for porous materials: A criterion based on the Biot theory,” *The Journal of the Acoustical Society of America*, vol. 122, no. 4, pp. 2038–2048, 2007.
- [82] Y. Salissou and R. Panneton, “Pressure/mass method to measure open porosity of porous solids,” *Journal of applied physics*, vol. 101, no. 12, p. 124913, 2007.
- [83] R. S. Lakes, *Viscoelastic solids*. CRC press, 1998.
- [84] A. Renault, *Caractérisation mécanique dynamique de matériaux poro-viscoélastiques (Dynamic mechanical characterization of poro-visco-elastic materials)*. PhD thesis, Université de Sherbrooke, 2008.

- [85] J. F. Allard, G. Jansens, G. Vermeir, and W. Lauriks, "Frame-borne surface waves in air-saturated porous media," *The Journal of the Acoustical Society of America*, vol. 111, no. 2, pp. 690–696, 2002.
- [86] L. Boeckx, P. Leclaire, P. Khurana, C. Glorieux, W. Lauriks, and J.-F. Allard, "Investigation of the phase velocities of guided acoustic waves in soft porous layers," *The Journal of the Acoustical Society of America*, vol. 117, no. 2, pp. 545–554, 2005.
- [87] J. F. Allard, M. Henry, L. Boeckx, P. Leclaire, and W. Lauriks, "Acoustical measurement of the shear modulus for thin porous layers," *The Journal of the Acoustical Society of America*, vol. 117, no. 4, pp. 1737–1743, 2005.
- [88] C. Langlois, R. Panneton, and N. Atalla, "Polynomial relations for quasi-static mechanical characterization of isotropic poroelastic materials," *The Journal of the Acoustical Society of America*, vol. 110, no. 6, pp. 3032–3040, 2001.
- [89] T. Pritz, "Frequency dependence of frame dynamic characteristics of mineral and glass wool materials," *Journal of Sound and Vibration*, vol. 106, no. 1, pp. 161–169, 1986.
- [90] T. Pritz, "Dynamic Young's modulus and loss factor of plastic foams for impact sound isolation," *Journal of Sound and Vibration*, vol. 178, no. 3, pp. 315–322, 1994.
- [91] L. Jaouen, A. Renault, and M. Deverge, "Elastic and damping characterizations of acoustical porous materials: Available experimental methods and applications to a melamine foam," *Applied acoustics*, vol. 69, no. 12, pp. 1129–1140, 2008.
- [92] D. Koblar and M. Boltežar, "Evaluation of the frequency-dependent Young's modulus and damping factor of rubber from experiment and their implementation in a finite-element analysis," *Experimental Techniques*, vol. 40, no. 1, pp. 235–244, 2016.
- [93] ISO 9053:91 (EN), *Acoustics – Materials for acoustical applications – Determination of airflow resistance*, 1991.
- [94] L. Jaouen, F.-X. Bécot, and F. Chevillote, "The acoustic characterization of porous media and its standards," in *45th International Congress and Exposition on Noise Control Engineering – InterNoise 2016, Hamburg*, 2016.
- [95] J. F. Allard, B. Castagnede, M. Henry, and W. Lauriks, "Evaluation of tortuosity in acoustic porous materials saturated by air," *Review of scientific instruments*, vol. 65, no. 3, pp. 754–755, 1994.
- [96] P. Leclaire, L. Kelders, W. Lauriks, C. Glorieux, and J. Thoen, "Determination of the viscous characteristic length in air-filled porous materials by ultrasonic attenuation measurements," *The Journal of the Acoustical Society of America*, vol. 99, no. 4, pp. 1944–1948, 1996.
- [97] P. Leclaire, L. Kelders, W. Lauriks, M. Melon, N. Brown, and B. Castagnede, "Determination of the viscous and thermal characteristic lengths of plastic foams by ultrasonic measurements in helium and air," *Journal of Applied physics*, vol. 80, no. 4, pp. 2009–2012, 1996.

- [98] Y. Atalla and R. Panneton, “Inverse acoustical characterization of open cell porous media using impedance tube measurements,” *Canadian Acoustics*, vol. 33, no. 1, pp. 11–24, 2005.
- [99] O. Doutres, Y. Salissou, N. Atalla, and R. Panneton, “Evaluation of the acoustic and non-acoustic properties of sound absorbing materials using a three-microphone impedance tube,” *Applied Acoustics*, vol. 71, no. 6, pp. 506–509, 2010.
- [100] “Material Characterization. Mecanum.” <http://www.mecanum.com/en/services/material-characterisation/>. Accessed: 2018-08-27.
- [101] K. V. Horoshenkov, A. Khan, F.-X. Bécot, *et al.*, “Reproducibility experiments on measuring acoustical properties of rigid-frame porous media (round-robin tests),” *The Journal of the Acoustical Society of America*, vol. 122, no. 1, pp. 345–353, 2007.
- [102] F. Pompoli, P. Bonfiglio, K. V. Horoshenkov, *et al.*, “How reproducible is the acoustical characterization of porous media?,” *The Journal of the Acoustical Society of America*, vol. 141, no. 2, pp. 945–955, 2017.
- [103] J. Bolton, N.-M. Shiau, and Y. Kang, “Sound transmission through multi-panel structures lined with elastic porous materials,” *Journal of sound and vibration*, vol. 191, no. 3, pp. 317–347, 1996.
- [104] T. G. Zieliński, “Microstructure-based calculations and experimental results for sound absorbing porous layers of randomly packed rigid spherical beads,” *Journal of Applied Physics*, vol. 116, no. 3, p. 034905, 2014.
- [105] C. Perrot, R. Panneton, and X. Olny, “Periodic unit cell reconstruction of porous media: Application to open-cell aluminum foams,” *Journal of Applied Physics*, vol. 101, no. 11, p. 113538, 2007.
- [106] C. Van der Kelen, P. Göransson, B. Pluymers, and W. Desmet, “On the influence of frequency-dependent elastic properties in vibro-acoustic modelling of porous materials under structural excitation,” *Journal of Sound and Vibration*, vol. 333, no. 24, pp. 6560–6571, 2014.
- [107] J. Cuenca, C. Van der Kelen, and P. Göransson, “A general methodology for inverse estimation of the elastic and anelastic properties of anisotropic open-cell porous materials – with application to a melamine foam,” *Journal of Applied Physics*, vol. 115, no. 8, p. 084904, 2014.
- [108] S. Finnveden, N.-E. Hörlin, and M. Barbagallo, “Dynamic characterization of viscoelastic porous foams used in vehicles based on an inverse finite element method,” *The Journal of the Acoustical Society of America*, vol. 135, no. 4, pp. 1834–1843, 2014.
- [109] A. Sfaoui, “On the viscoelasticity of the polyurethane foam,” *The Journal of the Acoustical Society of America*, vol. 97, no. 2, pp. 1046–1052, 1995.
- [110] J. D. Ferry and J. D. Ferry, *Viscoelastic properties of polymers*. John Wiley & Sons, 1980.

- [111] F. Duvigneau, L. Spannan, M. Gavila Lloret, E. Worschke, and U. Gabbert, “Characterization of the frequency dependent properties of damping materials,” in *PAMM - Proceedings in Applied Mathematics and Mechanics*, 2018. under review.
- [112] F. Duvigneau, L. Spannan, M. Gavila Lloret, and E. Worschke, “On the characterization of damping materials for acoustic simulations,” *Journal of Sound and Vibration*, 2018. in preparation.
- [113] Rumpler, R., *Efficient finite element approach for structural-acoustic applications including 3D modelling of sound absorbing porous materials*. PhD thesis, Conservatoire national des arts et métiers (CNAM) France, Kungliga Tekniska högskolan (KTH) Sweden, 2012.
- [114] Richter, C., *Liner impedance modeling in the time domain with flow*. PhD thesis, TU Berlin, 2010.
- [115] R. Lanoye, H.-E. de Bree, W. Lauriks, and G. Vermeir, “A practical device to determine the reflection coefficient of acoustic materials in-situ based on a Microflow and microphone sensor,” in *ISMA Conference on Noise and Vibration Engineering, Belgium*, 2004.
- [116] Y. Champoux and M. R. Stinson, “Measurement of the characteristic impedance and propagation constant of materials having high flow resistivity,” *The Journal of the Acoustical Society of America*, vol. 90, no. 4, pp. 2182–2191, 1991.
- [117] B. Brouard, D. Lafarge, and J.-F. Allard, “A general method of modelling sound propagation in layered media,” *Journal of Sound and Vibration*, vol. 183, no. 1, pp. 129–142, 1995.
- [118] L. Alimonti, N. Atalla, A. Berry, and F. Sgard, “Assessment of a hybrid finite element-transfer matrix model for flat structures with homogeneous acoustic treatments,” *The Journal of the Acoustical Society of America*, vol. 135, no. 5, pp. 2694–2705, 2014.
- [119] Villot, M., Guigou, C., and Gagliardini, L., “Predicting the acoustical radiation of finite size multi-layered structures by applying spatial windowing on infinite structures,” *Journal of Sound and Vibration*, vol. 245, no. 3, pp. 433–455, 2001.
- [120] O. Tanneau, P. Lamary, and Y. Chevalier, “A Boundary Element Method for porous media,” *The Journal of the Acoustical Society of America*, vol. 120, no. 3, pp. 1239–1251, 2006.
- [121] E. Deckers, N.-E. Hörlin, D. Vandepitte, and W. Desmet, “A Wave Based Method for the efficient solution of the 2D poroelastic Biot equations,” *Computer Methods in Applied Mechanics and Engineering*, vol. 201, pp. 245–262, 2012.
- [122] A. Craggs, “A finite element model for rigid porous absorbing materials,” *Journal of Sound and Vibration*, vol. 61, no. 1, pp. 101–111, 1978.
- [123] O. Dazel and N. Dauchez, *Materials and acoustics handbook*, ch. The Finite Element Method for Porous Materials, pp. 327–338. Wiley Online Library, 2009.

- [124] N. Atalla, M. A. Hamdi, and R. Panneton, “Enhanced weak integral formulation for the mixed (u, p) poroelastic equations,” *The Journal of the Acoustical Society of America*, vol. 109, no. 6, pp. 3065–3068, 2001.
- [125] R. Panneton and N. Atalla, “An efficient finite element scheme for solving the three-dimensional poroelasticity problem in acoustics,” *The Journal of the Acoustical Society of America*, vol. 101, no. 6, pp. 3287–3298, 1997.
- [126] S. Feng and D. L. Johnson, “High-frequency acoustic properties of a fluid/porous solid interface. I. New surface mode,” *The Journal of the Acoustical Society of America*, vol. 74, no. 3, pp. 906–914, 1983.
- [127] L. Alimonti and N. Atalla, “Efficient modeling of flat and homogeneous acoustic treatments for vibroacoustic finite element analysis. Direct field formulations,” *Journal of Sound and Vibration*, vol. 367, pp. 84–100, 2016.
- [128] M. Ouisse, L. Maxit, C. Cacciolati, and J.-L. Guyader, “Patch transfer functions as a tool to couple linear acoustic problems,” *Journal of vibration and acoustics*, vol. 127, no. 5, pp. 458–466, 2005.
- [129] M. Polanz, E. Nijman, and M. Schanz, “The Patch-Transfer-Function (PTF) method applied to numerical models of trim materials including poro-elastic layers,” Tech. Rep. 2018-01-1569, SAE Technical Paper, 2018.
- [130] O. Dazel, B. Brouard, J.-P. Groby, and P. Göransson, “A normal modes technique to reduce the order of poroelastic models: Application to 2D and coupled 3D models,” *International Journal for Numerical Methods in Engineering*, vol. 96, no. 2, pp. 110–128, 2013.
- [131] E. Lappano, M. Polanz, W. Desmet, and D. Mundo, “A parametric model order reduction technique for poroelastic finite element models,” *The Journal of the Acoustical Society of America*, vol. 142, no. 4, pp. 2376–2385, 2017.
- [132] R. Panneton, *Modélisation numérique tridimensionnelle par éléments finis des milieux poroélastiques (Finite Element three-dimensional numerical modeling of poroelastic media)*. PhD thesis, Université de Sherbrooke, 1996.
- [133] N. Dauchez, S. Sahraoui, and N. Atalla, “Convergence of poroelastic finite elements based on Biot displacement formulation,” *The Journal of the Acoustical Society of America*, vol. 109, no. 1, pp. 33–40, 2001.
- [134] S. Rigobert, N. Atalla, and F. Sgard, “Investigation of the convergence of the mixed displacement-pressure formulation for three-dimensional poroelastic materials using hierarchical elements,” *The Journal of the Acoustical Society of America*, vol. 114, no. 5, pp. 2607–2617, 2003.
- [135] N.-E. Hörlin, “3D hierarchical hp-FEM applied to elasto-acoustic modelling of layered porous media,” *Journal of Sound and Vibration*, vol. 285, no. 1-2, pp. 341–363, 2005.
- [136] H. Henn, G. R. Sinambari, and M. Fallen, *Ingenieurakustik: Grundlagen, Anwendungen, Verfahren*. Springer-Verlag, 2013.

- [137] M. Möser, *Technische Akustik*, vol. 8. Springer, 2009.
- [138] F. Sgard, N. Atalla, and J. Nicolas, “A numerical model for the low frequency diffuse field sound transmission loss of double-wall sound barriers with elastic porous linings,” *The Journal of the Acoustical Society of America*, vol. 108, no. 6, pp. 2865–2872, 2000.
- [139] Free Field Technologies S.A., *Actran 17 User’s Guide - Volume 1*. MSC Software Belgium SA, 2016.
- [140] M. Scheinhardt, *Sound-engineering im Automobilbereich*, ch. Prüstände zur Entwicklung von Luftschallmaßnahmen. Springer-Verlag Berlin Heidelberg, 2010.
- [141] de Bree, H.E., “The Microflown E-Book,” tech. rep., Microflown Technologies, 2007.
- [142] E. Tijs, A. Nejade, and H. de Bree, “Verification of PU intensity calculation,” in *INTER-NOISE and NOISE-CON Congress and Conference Proceedings*, 8, pp. 423–434, Institute of Noise Control Engineering, 2009.
- [143] F. Jacobsen, *Springer Handbook of Acoustics*, ch. Sound intensity. Springer, 2014.
- [144] “Sound and Vibration Measuring and Analysis System. PAK. Müller-BBM VAS.” <https://www.pakbybbm.com/>. Accessed: 2018-06-27.
- [145] H. M. Atassi, “Introduction to Acoustics.” Lecture notes. University of Notre Dame, Indiana (USA).
- [146] R. Randall and B. Tech, *Frequency analysis*. Bruël and Kjær, 1987.
- [147] R. Panneton and N. Atalla, “Numerical prediction of sound transmission through finite multilayer systems with poroelastic materials,” *The Journal of the Acoustical Society of America*, vol. 100, no. 1, pp. 346–354, 1996.
- [148] K. R. Symon, *Mechanics: 3rd Ed*. Addison-Wesley Publishing Company, 1971.
- [149] P. Schrader, F. Duvigneau, M. Gavila-Lloret, H. Rottengruber, and U. Gabbert, “Finite element analysis of the acoustic behavior of poroelastic materials based on experimentally determined frequency dependent material properties,” in *ISMA Conference on Noise and Vibration Engineering, Belgium*, 2018.
- [150] J. F. Allard, Y. Champoux, and C. Depollier, “Modelization of layered sound absorbing materials with transfer matrices,” *The Journal of the Acoustical Society of America*, vol. 82, no. 5, pp. 1792–1796, 1987.
- [151] M. V. van der Seijs, D. de Klerk, and D. J. Rixen, “General framework for transfer path analysis: History, theory and classification of techniques,” *Mechanical Systems and Signal Processing*, vol. 68, pp. 217–244, 2016.
- [152] H. Van der Auweraer, P. Mas, S. Dom, A. Vecchio, K. Janssens, and P. Van de Ponsele, “Transfer path analysis in the critical path of vehicle refinement: The role of fast, hybrid and operational path analysis,” Tech. Rep. 2007-01-2352, SAE Technical Paper, 2007.

- [153] S. F. Wu and L. Kumar Natarajan, “Panel acoustic contribution analysis,” *The Journal of the Acoustical Society of America*, vol. 133, no. 2, pp. 799–809, 2013.
- [154] O. Wolff and R. Sottek, “Binaural panel noise contribution analysis. An alternative to the conventional window method,” in *CFA/DAGA Strasbourg*, 2004.
- [155] J. Hald and J. Mørkholt, “Panel contribution analysis in a vehicle cabin using a dual layer handheld array with integrated position measurement,” *SAE International Journal of Passenger Cars-Mechanical Systems*, vol. 2, no. 2009-01-2171, pp. 1458–1469, 2009.
- [156] H. Jakob, A. Bocquillet, S. Marburg, and H.-J. Hardtke, “Validation of a measurement based Area Contribution Analysis,” in *NAG/DAGA Rotterdam*, 2009.
- [157] O. Wolff, E. Tijs, and H.-E. de Bree, “A PU probe array based panel noise contribution analysis whilst driving,” Tech. Rep. 09NVC-0094, SAE Technical Paper, 2009.
- [158] O. Wolff, “Fast panel noise contribution analysis using large PU sensor arrays,” in *INTER-NOISE and NOISE-CON Congress and Conference Proceedings*, vol. 2007, pp. 1112–1121, 2007.
- [159] M. Grialou, N. Totaro, A. Bocquillet, and G. J.-L., *Motor- und Aggregate-Akustik: Tagungsband des 9. Magdeburger Symposiums*, ch. Identification of the inherent impedances of subsystems, based on the acoustical response of a fully coupled system, pp. 63–83. OvGU, 2016.
- [160] W. Kaplan, *Advanced calculus*. Addison-Wesley, 1952.
- [161] D. T. Francis, “A gradient formulation of the Helmholtz integral equation for acoustic radiation and scattering,” *The Journal of the Acoustical Society of America*, vol. 93, no. 4, pp. 1700–1709, 1993.
- [162] F. Fahy, “Some applications of the reciprocity principle in experimental vibroacoustics,” *Acoustical Physics*, vol. 49, no. 2, pp. 217–229, 2003.
- [163] “LMS Qsources Siemens PLM Software: Mid/High-Frequency Volume Source.” <https://www.plm.automation.siemens.com/fr/products/lms/testing/qsources/mid-high-frequency-source.shtml>. Accessed: 2018-07-17.
- [164] M. Gavila Lloret, G. Müller, F. Duvigneau, and U. Gabbert, *Motor- und Aggregate-Akustik: Tagungsband des 10. Magdeburger Symposiums*, ch. Prediction of the sound transmission through a simplified front end model of a car, pp. 257–274. OvGU, 2018.
- [165] Evonik Industries AG, *Technical Information Plexiglas® – Ref. No. 211-1*, 2013.
- [166] Free Field Technologies S.A., *Actran 17 User’s Guide - Volume 2*. MSC Software Belgium SA, 2016.